2021-05-01

Development And Testing Of Nanostructured Materials For Extreme Environment Applications

Nanthakishore Makeswaran
University of Texas at El Paso

DEVELOPMENT AND TESTING OF NANOSTRUCTURED MATERIALS FOR EXTREME ENVIRONMENT APPLICATIONS

Nanthakishore Makeswaran
Doctoral Program In Mechanical Engineering

APPROVED:

_____
Ramana V. Chintalapalle, Ph.D., Chair

_____
Arturo Bronson, Ph.D.

_____
Skye Fortier, Ph.D.

_____
Eric MacDonald, Ph.D.

_____
Stephen L. Crites, Jr., Ph.D.
Dean of the Graduate School

DEVELOPMENT AND TESTING OF NANOSTRUCTURED MATERIALS FOR EXTREME ENVIRONMENT APPLICATIONS

By

NANTHAKISHORE MAKESWARAN

DISSERTATION

Presented to the Faculty of the Graduate School of
The University of Texas at El Paso
in Partial Fulfillment
of the Requirements
for the Degree of

DOCTOR OF PHILOSOPHY

Department of Mechanical Engineering
THE UNIVERSITY OF TEXAS AT EL PASO
May 2021

Acknowledgements

Firstly, I would like to express my gratitude to my advisor and mentor Dr. Ramana Chintalapalle, for the guidance, support, and patience he has shown me throughout my academic career in the pursuit of my doctoral research. I have grown tremendously as a scholar, researcher and person thanks to his encouragement and education and I am immensely grateful for the lessons I have learned from him.

I would like to thank Dr. Arturo Bronson, Dr. Eric Macdonald, and Dr. Skye Fotier who have agreed to be part of my doctoral committee and were willing to spend their valuable time to evaluate my dissertation research.

Additionally, I would like to thank the past and present team members at UTEP including Dr. Debarata Das, Dr. Malasham Bandi, Dr. Anil K. Battu, Dr. Swapdita Roy, Mr. Vishal Zade, Mr. Cristain Orozo, Ms. Rebecca Romero, and to the many others who have helped me in this endeavor and made my research experience both possible and fulfilling.

I would like to dedicate this work to my parents Mr. Makeswaran Seenivasagam, and Mrs. Saranga Makeswaran, who constantly pushed me to achieve the utmost with my life while offering their continual support and patience.

Finally, I wish to express my sincere thanks to the institutions and organizations that made my research possible including the Department of Energy, National Science foundation, Lawrence Livermore National Laboratory, Air Force Research Laboratory, and the German aerospace center. While portions of the research presented in this dissertation was supported by the DoE and DoD, the views and opinions expressed by the author(s) herein do not necessarily state or reflect those of the United States government or funding agency thereof.

Abstract

Nanostructured materials have many potential applications in the fields of power generation and transportation technologies, particularly in the areas of gas sensing technology, industrial gas turbines and protective coatings. In the former case β-Ga_2O_3 represents a promising candidate due to its high degree of stability and functionality for oxygen sensing at higher temperatures (>700^{o}C). In the latter case, the application of Y-Si-Fe compounds acting as environmental barrier coatings for gas turbine and aerospace engine applications to protect from corrosion effects has been demonstrated in recent years. In both cases, however, there is room for improvement whether it is in the form of innate material properties for the reduction of response time and increase sensitivity for sensors to resistance to harmful airborne particulates for protective coatings. In this work, a multi-stage approach was adopted for testing the chemical and physical properties of these classes of materials after a variety of fabrication methods to ensure nanoscale structures was completed. For sensor work making use of gallium oxide, RF-magnetron sputtering, pulsed laser deposition, and electrospinning was employed to manufacture thin films, epitaxial nanocolumnar structures, and nanofibers, respectively. All of these were subjected to high temperature fabrication and post fabrication processes (>500^{o}C) to simulate effects of these conditions on crystal structure, optical, electrical, and mechanical properties. This was done in order to determine suitability for extreme environmental applications and the extent that properties of gallium oxide could be fine-tuned via nanostructure as opposed to dopant inclusion. For structural components the Y-Si-Fe coatings where subjected to simulated, destructive, airborne particulates to determine their ability to maintain structural integrity in real world situations. Throughout the work a wide variety of analytical techniques were employed to derive conclusions on the structure, morphology, chemical states, and thermos-mechanical properties of the materials.

The results are presented and discussed in this thesis on determining the feasibility of utilizing nanoscale structures for extreme environmental conditions as well as implications and potential future work regarding integrated sensing and structural components to maximize combustion efficiency and durability.

Table of Contents

List of Tables

Page

List of Figures

Page

1. Introduction

With the rapid development of technology in a variety of fields ranging from automation and aerospace to energy production and manufacturing there has been an increasing need for functional and structural materials that can operate in extreme environments. These conditions can include exposure to high temperatures, radiation, thermal gradient extremes, high pressures, and toxic or corrosive chemical environments. Not only do such applications require high durability and reliability on the part of the materials, but also on the architecture utilized for those materials.

One such area of interest lies in the modern combustion process utilized in energy generation systems and aircraft propulsion. These processes are highly dependent, not only on sensing, monitoring, and oxygen control for maximum system efficiency, but also on high durability of their components to ensure maximum energy creation and lifespan. Additionally, the application of these sensors to efficiently control oxygen levels during combustion processes can serve to reduce hazardous emissions such as NO_x, CO_2, and SO_2 (1). Within the realm of energy generation, various gases have become important raw materials for energy generation, which necessitates continuous monitoring of gas concentrations in as selective manner as possible. This leads to the need for materials that can potentially operate beyond just oxygen sensors and be used for a large array of sensing applications for improved energy system performance.

Efforts in this field have focused on increased chemical gas sensitivity, improved selectivity, reduction of electric power, and an overall decrease of response and recovery times to better suit high speed combustions processes (1-6). This has largely been done via the miniaturization of gas sensors via thin films, metal-oxide-semiconductor (MOS), semiconductor, and membrane technologies. However issues regarding measurement inaccuracies, and the

inherent physical characteristics of the materials and structures utilized have made developing sensors with high degree of accuracy and reliability difficult.

Beyond the development of nanostructured materials and devices in energy applications, the usage of such advancements to improve the structural integrity of advanced transportation needs such as the turbines engines utilized in airplanes is also of great interest. One key example lies covered in this work involves the effects of CMAS (calcium-magnesium-alumno-silicates) which constitute much of the various airborne particulates such as sand, industrial pollutants, and in particular volcanic ash that can cause significant damage to airplane engine components when ingested during flight (2). These materials, once ingested during flight, will melt at the operational temperatures of the engines which can exceed 1200 °C and will damage both the components of the engines themselves as well as any protective coatings applied to them to prevent damage via other physical or chemical processes.

One such protective coating subtype that can be negatively affected by molten CMAS exposure are known as thermal barrier coatings (TBC) and environmental barrier coatings (EBC). These materials consist of ceramics which low thermal conductivity deposited onto a substrate material via a bond coat to prevent structural damage due to high temperatures. A commonly used variety is 7 wt.% yttria stabilized zirconia. Another class of coating, and a primary focus of this work, are known as environmental barrier coatings (EBC). These are a group of ceramic coatings that are generally applied to ceramic matrix composites to protect underlying components from water vapor recession during atmospheric combustion. Yttrium mono-silicates and yttrium di-silicates have shown promise from a water recession preventative standpoint. In both cases, exposure to CMAS particles can infiltrate theses protective coatings. In the case of TBC's, they will tend to cause chemical degradation leading to the loss of the coatings strain tolerant

microstructure, and eventual spallation. For EBC's the most common failure mechanism involves rapid reaction with and consumption into the applied molten CMAS. With such consideration in mind, developing nano structured materials that can meet the ever-increasing demands of the energy and transportation fields lies at the core of this work.

The typical CMAS attack in gas turbines is due to the deposition of molten CMAS glassy particles on the hot gas path components, which subsequently infiltrate the porous TBC network. As the molten glass penetrates the porous TBC, it changes its mechanical properties, which leads to premature coating spallation. A pre-requisite for any TBC/EBC material to be CMAS resistant is its ability to react quickly upon interaction with the molten CMAS glass-forming stable reaction phases. Then, the reaction phases must nucleate in a beneficial shape, which promotes the seal of the open porosities in the TBC, maintaining a shallow infiltration. Furthermore, since the range of chemical composition of CMAS bearing compounds is vast, the compositionally tailored TBC/EBC with enhanced efficiency can be realized only by means of extensive studies on the design and development of materials.

The present work is focused towards a set of two different compositions, where the design and development of nanostructured materials is the key, for utilization in two different aspects in turbine based combustion processes. The first is the materials for sensors. Currently, there is an increased interest in the integration and control of combustion processes using advanced sensors and controls. Reliable high-temperature sensors are needed near the combustion zone. In addition to being reliable, fast, highly sensitive, and selective, the sensors that are desired for detecting and monitoring of gases in the energy processes must be survived. The second is the EBC development, where the coatings can integrate the sensors in addition to offering excellent CMAS resistance.

2. Motivation

The future development of efficient and durable power generation systems, and optical sensors for both airborne and terrestrial applications is highly dependent on a comprehensive system of components that work together for maximum performance. Metal oxide semiconductors offer a promising medium for sensors due to low cost, low power consumption, and ease of integration due to small dimensions. However, there is a need for improved response and recovery times and long-term stability for which multiple options of nano-structured materials exist. Additionally, the resistance to environmental degradation, whether by thermal, mechanical, or chemical sources, of both the sensors and the components in which they may be integrated, is key to long term viability.

Across the entire process, whether for sensing or structural applications there will be a need to follow cyclic developmental procedure that maximizes the efficiency of material creation and performance. This will involve selecting fabrication methods that can produce high quality materials and structures while retaining the ability to be easily scaled for potential commercial applications. Optimization of depositions conditions based on structural, electrical, electronic, and morphological characterizations and associated structure-property correlations is key for deriving the most efficient process for creating usable materials. The final stage would then involve evaluation of sensors and coatings under simulated operating conditions to determine if they meet necessary criteria.

Keeping the aforementioned technological and scientific issues in mind, this project sought to study the nanostructured materials' design and development for energy related applications. The first part was toward Ga_2O_3 in the form of thin films derived from RF magnetron sputtering and

pulsed laser deposition, as well as nanofibers created through electrospinning processes. The aim was developing materials that serve as promising candidates for oxygen or other chemical sensors with rapid response times, selectivity, and long-term stability when exposed extreme environmental conditions. Simultaneously, giving importance into structural components, which can even integrate these sensor elements, an investigation of Fe-Y oxide based environmental barrier coatings (EBCs) also performed. Efforts made to address one potential issue from structural side of this matter in regards to turbine degradation via molten CMAS exposure. The underlying goal of this work is to develop a fundamental understanding of the intrinsic properties of these nanoscale gallium oxide structures and environmental barrier coatings to determine their feasibility when eventually applied to the roles as sensors and structural coatings in physically demanding conditions as well as lay a ground work for future research into the topic.

The first objective of this work involved the fabrication of high-quality β-Ga_2O_3 thin films via RF magnetron sputtering and pulsed laser depositions. The use of the two separate systems was to determine which would develop thin films with the ideal properties for either oxygen or gas sensors. These techniques also have the benefit of being readily repeatable, as well as offering the ability to be easily integrated into mass production systems. The second objective in regards to the sensor portion of the project involved deposition of gallium oxide nanofibers via electrospinning. This method was chosen as nanofibers possess a higher surface area to volume ratio as compared to thin films which has the potential to increase gas diffusion rates when applied as an oxygen sensor. Nanofibers have also demonstrated unique photoluminescent properties that may lend themselves to optical sensors when applied properly.

For all three cases the deposition conditions will be fine-tuned to determine what parameters lead to the best structural, electrical, and morphological conditions in the samples. A

variety of parameters ranging from substrate temperatures and reactive gas partial pressures for PLD and magnetron depositions to calcining temperatures and salt precursor concentrations for the electrospinning samples will be tested. The end goal is to produce samples with high structural quality.

The third portion of this project shifts to the structural aspect of a potential integrated system and deals with the deposition of an environmental barrier coating via magnetron sputtering. As before this will serve to provide a uniform coating method that can be readily scaled up to commercial applications. Unlike the previous primary objects, the focus is less on the deposition and testing of the coatings individually, and more on determining their interactions with varying CMAS compositions, temperatures, and exposure times to determine their potential long-term viability.

Finally, the research objectives of this thesis work can be summarized into the following main key points:

Research Objective 1:	Fabrication and Synthesis of High-Quality Sensor and EBC materials Physical and Chemical Deposition Methods
Research Objective 2:	Understand the Effect of Processing Conditions on the Phase, Structure, Microstructure and Properties
Research Objective 3:	Optimize Conditions to Produce Nanostructured Materials with Desired Structure & Properties to Derive Enhanced Performance Devices

3. Literature Review

Current gas sensor technology suffers from issues of response and recovery times and stability. Semiconductor/metal oxide materials display many properties that lend themselves for gas sensor applications. Metal-oxide based *n*-type semiconductors are commonly used sensing materials as they can detect a change in the gas atmosphere due to changes in the electrical resistance. As a result, a polycrystalline metal oxide thin film will show superior performance compared to large grain films, or single crystal-based sensors. This is due to the effects of potential energy barriers between grain boundaries on electrical conductivity. A chemical sensor will make use of two basic functions. One is the receptor function that serves to recognize a chemical substance at the surface of the semiconducting layer. The second is the transducer function that transduces the chemical signal through the material into an electrical output. The corresponding change in electrical resistance across the sensing element is what is then recorded as a signal. As absorption and desorption are highly temperature dependent processes, the temperature becomes a key parameter for any sensor, and as a result requires materials that have stable performance at the potentially high temperatures at which combustion processes generally occur (3-6).

Wide band gap oxides have been the focus of extensive work due to the material's compatibility in a variety of applications including electronics, photonics, photo catalysts, and chemical sensing (3-15). Among these oxides, β-Ga_2O_3 displays many properties that make it an attractive choice for gas sensing applications. It possesses the second largest band gap of this particular group of materials with ~4.9 eV (12,16). Additionally, it possesses diverse structures, useful material properties, as well as chemical and thermodynamic stability (6,8,9,12). β-Ga_2O_3 in various thin film and other nanostructures have found multiple applications, in high temperature sensors, electronics, luminescent phosphors, batteries, antireflective coatings, and solar cells (10-

15,18,19). Gallium oxide exhibits polymorphism with the α, β, γ, δ, and ε phases being widely studied (12,20,21). While certain polymorphs are still not well understood such as the γ, and ε phase, others have well documented physical properties that lend themselves to a variety of potential applications. For example, α phase Ga_2O_3 exhibits the highest band gap among the polymorphs, as well as a higher refractive index and reflectance, while possessing a lower mass of electrons when compared to β-Ga_2O_3 (9-14). This high band gap marks this polymorph as a promising candidate for heterojunction of two crystals for photocatalytic applications. Monoclinic β-Ga_2O_3, one of the materials that serves as a primary focus of this work, is thermally stable with a high breakdown field strength of 8 MV/cm (12,19). β-Ga_2O_3 is in fact the only polymorph of gallium oxide that is stable until its melting point of approximately 1900 °C whereas all other polymorphs are metastable and will convert into β-Ga_2O_3 at temperatures between 750-900 °C (9-14). A representation of a β-Ga_2O_3 can be seen in Figure 1.

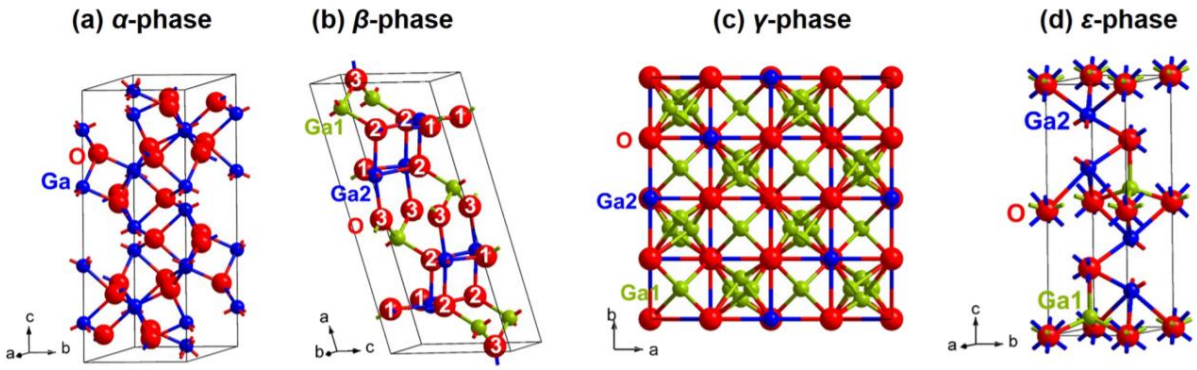

Figure 1: a) α-Ga_2O_3 unit cell, b)β-Ga_2O_3 unit cell, c)γ-Ga_2O_3 unit cell, d)ε-Ga_2O_3 unit cell (7)

One of the aspects of this material that makes it particularly useful for the development of high temperature chemical sensors is its high thermal stability. (11,12). This, coupled with Ga_2O_3

based materials deep ultraviolet transparency makes them potential candidates for chemical sensors in extreme environments as well as transparent electrodes in UV photonics, thin-film transistors, and optoelectronics. (11,12, 21, 22). However, it should be noted that regardless of the applications, a fundamental understanding of the crystallography, surface interface structure, and chemical properties is needed as well as proper tuning of the microstructure to ultimately enhance device performance.

One such method for tuning the properties of gallium oxide films is via thermal annealing. Annealing at the post fabrication stage is a common practice in the manufacturing of electronics for device applications. Annealing strongly influence the microstructure and properties of oxide-based materials (22-31). A large number of efforts have be directed to understanding the effects of atmosphere and temperature on the mechanical, chemical, electronic, and physical properties of gallium oxide films (25-30). One study deposited β-Ga_2O_3 thin films using laser-assisted molecular beam epitaxy at 600°C, and where subsequently annealed at different temperatures and durations in air and oxygen (29). While annealing at 800-900°C for 30 or 60 minutes led to the samples remaining close to β-Ga_2O_3, increasing the annealing temperature and/or annealing time fully destroyed the crystal quality. Furthermore, the optical characteristics indicate a red-shift of absorption edge with in the annealed layers as opposed to the as deposited ones. The band gap differences were attributed to the relaxing of the in-plane compressive strain during annealing. The authors further noted a reduction in nonstoichiometric GaO_x phases after high temperature annealing in air and oxygen atmosphere with the material being fully converted to Ga_2O_3. This was associated with a decrease in oxygen deficiency and oxygen vacancy concentration (29). High temperature annealing in an oxygen atmosphere is beneficial for recrystallization of β-Ga_2O_3 which is considered the cause of the larger photo-current obtained in the oxygen annealed device.

Another study involving annealing of the β-Ga_2O_3 films grown by anodic oxidation of n-GaAs wafers indicate a phase evolution sequence. A high degree of difference was observed in reaction tendencies when the layers where annealed in argon at temperatures of 600 and 900°C for 30 minutes (26). Non-annealed films reacted readily with acids which served to confirm the presence of the α-phase, and while those films annealed at 600°C dissolved in a hydrochloric acid solution, the films annealed at 900°C did not (26). Additionally, post-deposition annealing tests of electrical conductivity of the films showed an increase for both temperatures and a current growth decrease from 80-90 V to 4-6 V. Those without annealing also showed reduced increase in forward current with voltage compared to those films annealed in oxygen (26).

Further studies on the annealing of β-Ga_2O_3 films deposited by pulsed laser deposition (PLD) technique on (0001) oriented sapphire substrates showed the films had a [401] orientation with low intensity peaks (31). The films retained identical compositions regardless of the varied annealing temperatures, though they did have variances in their surface structure. The 800°C film has a smoother surface and relatively larger feature size, while the 1000°C film had an enhancement in the surface lateral feature size. Additionally, the films did exhibit AL diffusion from the substrate as a result of the high temperature annealing (31).

Extensive transformative behavior brought on by the annealing process was noted in a study where a semiconductor to insulating electronic transformation was seen in a Si-doped β-Ga_2O_3 films when annealing was performed at 800-850°C in O_2 atmosphere (28). Multiple studies have also shown that oxygen vacancy and carrier concentration decrease after annealing of β-Ga_2O_3 single crystals (25). The physical structure of gallium oxide films is also seen as was the case when films deposited by Metal Organic Chemical Vapor Deposition showed and amorphous to crystalline structural transformation with improved crystalline quality and mother surface

following annealing at 900°C (27,29). This improved crystalline quality also led to minimum optical band gap coupled with a very high transparency (27,29).

Physical processes for tuning a material need not be limited to post deposition procedures. A variety of relatively low-cost processes such as Pulsed Laser Deposition (PLD) or Chemical Vapor Deposition (CVD), can be employed to design various nano-architectures within a deposited thin film. These include, but are not limited to, columnar nanostructures, vertical nanopillars, nano helixes, and zigzag nanopillars (32-38). One particular relevant study involved the deposition of β-phase (100) $(Al_xGa_{1-x})_2O_3$ thin films via metalorganic chemical vapor deposition. In this study a step flow growth process of the film on a β-Ga_2O_3 substrate involved the absorption, diffusion, and adherence of Al adatoms on the growth surface along with Ga adatoms incorporation at the nearest Al site. These Al areas acted as preferential nucleation sites for incoming Ga adatoms (33). This initial nucleation process and growth process is a potential creation mechanism for nano-columnar structures that will be a focus of this work. In general, while these structures have proven promising for applications in electronics, optoelectronics, and photocatalysts, precise size control and phase stability during deposition remain challenging.

When speaking of such applications the luminescence in n β-Ga_2O_3 has been widely investigated, with the agglomeration of the findings in respect the materials photoluminescence, including studies on potential dopants and concentrations was used to derive the mission with a specific color in the visible region (37-39). In one particular study it was reported the ultraviolet (UV) and red emission PL bands at ∼3.40 and ∼1.78 eV, respectively, in β-Ga_2O_3 nanostructures (39). These nanostructures were arranged in a core−shell structure, where the crystalline core is associated with an amorphous shell. In fact, both blue- and green emission characteristics were observed in β-Ga_2O_3 previously. Recombination of the charge carriers trapped by the O and Ga

vacancies, leading to deep donor and acceptor states, respectively, has been proposed as the origin of the blue PL band. A multitude of explanations exist for red and UV emissions for β-Ga_2O_3, green emissions are typically only observed via doped samples. Deriving green emission characteristics in β-Ga_2O_3 without the need for dopants via control of the size, phase, and interface of the highly dense, close-compact nanocolumnar nanostructures can serve to expand potential applications of the material in optical sensors while reducing costs and complexity from a manufacturing standpoint.

Beyond tuning of materials via a physical process like annealing, novel structural approaches to improving durability and long-term stability of sensors also stands as a viable approach. One such nanoscale structure that shows promise in the sensing and energy fields is the nano fiber. This form of engineered nano-architecture, designed to take advantage of improved chemical and structural properties, shows enhanced surface flexibility, stiffness and tensile strength compared to other classes of materials, including thin films. This 1D nano architecture serves as an optimal material system to determine the effects of size reduction and dimensionality on characteristics such as electrical, optical, mechanical, and thermo-chemical properties (40-45). In terms of their usage in gas sensors, nanofibers provide a high surface to volume ratio allowing for the possibility of improved gas diffusion which in turn can lead to improved response and recovery times (46,47). Various inorganic nanowires and fibers have been shown promising results when used in nanoscale electronics, opto-electronics, and sensor devices (48-51).

An effective and commonly used means of producing nanofibers is the electrospinning process. This involves inducing a static electrical charge in a solution, and once a critical voltage is achieved, a subsequent self-repulsion of the charges causes the solution to stretch into a fiber. A structure known as a taylor cone forms during this process and thin strands, typically from a

positively charged syringe, will be drawn to a negatively charged collector (53,54). A major advantage of the electrospinning process is the tunability of the resultant nanofibers via manipulation of the spinning solution. This solution will usually contain a salt precursor, polymer, and reasonably volatile solvent such as water or ethanol. One study demonstrated that the diameter of the precursor fibers can adjusted by controlling the concentrations of zinc acetate in the solution when creating ZnO fibers (54,55). Post spinning calcination and annealing parameters can readily adjust the morphology of the fibers as well. Additional literature of electrospinning fabrication of various oxides indicates that processing conditions and precursor chemistry strongly influence crystal structure, chemical composition, electronic, and optical properties. This ability to easily customize the properties of the resultant nanofibers lends a great deal of potential versatility when designing and implementing them in a sensing application.

Of course, application of nanoscale extreme environment materials is not limited to sensing only. Thermal barrier coatings (TBCs) and one of the primary focuses of this study, environmental barrier coatings (EBCs) play a critical role in the physical integrity and long term viability of aircraft engines and gas turbines in extreme environments. EBC refers to a class of materials comprising of ceramic layers coated onto components such as SiC fiber reinforced SiC ceramic matrix composites. Their high temperature resistance and lighter weight as opposed to more traditional nickel based super alloys has led to an increasing demand in the aviation industry, particularly in the high heat sections of engines (56,57). The major vulnerability of these materials lies in oxidation and water recession as a result of water vapor in the engine; this is where EBCs come into play to afford a level of protection against such degrading processes. EBCs can vary in thickness from 25 to several hundreds of micrometers, and are usually multilayer systems consisting of a bond coat, and dense rare earth (RE) silicate layers. These layers will need a

relatively low CTE (coefficient of thermal expansion) and will need to endure temperatures up to 1650 °C and potentially beyond (2,56,58-60). A basic schematic of a coating system incorporating an EBC is shown in figure 2.

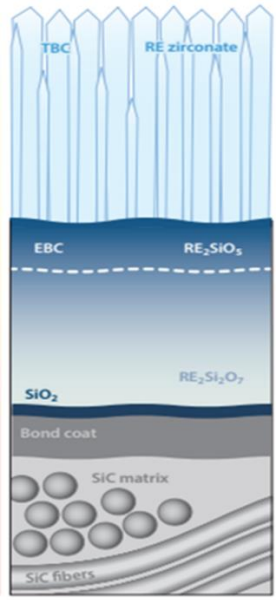

Figure 2: Schematic of typical Environmental Barrier Coating (60)

At higher temperatures, SiC will form a protective SiO_2 layer (59). The bond coat between the chosen substrate and the rare earth silicates can be made of a Si or Re-Si alloy. Hf or Zr can be added as dopants to reduce oxidation (56,58,60). As Si melts at 1414 °C, alternative Si based bond coats are preferred when dealing with higher expected temperatures, and during exposure to such temperatures a SiO_2 TGO (thermally grown oxide) layer will form at the top of the bond coat (61). If high temperature water vapor is present during this point, the TGO will react with the water and subsequently vaporize. This causes the formation of gaseous $Si(OH)_4$ and as a result the recession of the protective SiO_2 layer. This will in turn lead to a decrease in the overall strength of the material (2,56).

$$SiO_2 \text{ (solid)} + H_2O \text{ (gas)} \rightarrow Si(OH)_4 \text{ (gas)} \quad (1)$$

The above reaction is the reason EBCs must act as a water vapor barrier while remaining chemically stable enough to minimize reaction with the TGO and bond coat (56,20,62). These requirements necessitate that EBCs be dense enough to ensure low permeability, and have a low CTE mismatch between both the layers of the coating system and the substrate to reduce thermal stresses on the coating layers and minimize any cracking or delamination. Multiple potential EBC material candidates have been examined including RE monosilicates (RE_2SiO_5), RE disilicates ($RE_2Si_2O_7$), and barium strontium/magnesium aluminum silicates (BSAS/BMAS). When used in combination, the first two demonstrate low CTE values close to SiC and reduced volatility when compared to BSAS/BMAS compositions (56-48).

The EBCs tend to dissolve into molten CMAS on the coating surface as opposed to TBCs where CMAS infiltration stands as the primary failure mechanism (2). This dissolution process, which is the result of continuous chemical reactions between the CMAS and coating, leads to new crystalline phase formation, and causes continual degradation of the coating. A promising counter to this, and the focus of the respective portion of the study, is to maximize the reactivity of the EBC material with the molten CMAS to encourage crystallization of desired reaction products and create equilibrium between the unreacted EBC and the remaining CMAS.

Yttrium disilicates (YDS) and Yttrium monosilicates (YMS) demonstrate properties such as low elastic modulus, low CTE, low oxygen permeability, low water vapor recession, low volatility, and high melting points (1950 °C and 1980 °C respectively). This has made them attractive candidate in a variety of EBC studies (61). SiO_2 reacts with RE (in this case Y) oxides to form silicates based on stoichiometry a sample of which shown below.

$$Y_2O_3 + SiO_2 \rightarrow Y_2SiO_5 \quad (2)$$

$$Y_2SiO_5 + SiO_2 \rightarrow Y_2Si_2O_7 \quad (3)$$

$$Y_2O_3 + SiO_2 \rightarrow Y_2Si_2O_7 \quad (4)$$

Studies carried out at the German Aerospace Center (DLR) demonstrated that the addition of iron oxide and yttria via magnetron sputtered YSiFe coatings led to improvements to CMAS resistance and reactivity characteristics. This led to reduced CMAS damage to the coatings (62). This came with the caveat that there was a need for post deposition annealing to stabilize a crystalline YMS phase and an yttria rich FeO containing phase. This was the result of YMS having 2 temperature dependent polymorphs. Heat treating of the coatings lead to crystallization of single phase of YMS to improve thermal stability as well as prevent phase transformations as a result of cyclic temperature cycles during potential engine or gas turbine usage (60-63). The transition from the X1 phase (low temperature) to the desired X2 phase (high temperature) happens between 850 °C - 1200 °C with the X2 phase being predominant above 1190 °C (59-63). The needed Y_2O_3:SiO_2 ratio to achieve a stable YMS as well as the various YDS polymorphs are shown in figure 3. Furthermore, the heat treatment served to create a homogenous layer, with a certain amount of innate porosity to offset thermal stresses that can arise from CTE mismatch. In this regard FeO pays an important role as pure yttria/YMS coatings tend to suffer from extensive phase segregation allow for areas more prone to CMAS infiltration. When FeO is incorporated into the coatings, they become substantially more homogeneous post heat treatment with stabilization of the desired X2-YMS phase (56-60). The FeO also had the benefit of triggering the creation of stable yttrium iron garnet which contained all available cations from the CMAS melt and coating material. This resulted in more efficient CMAS consumption (62,64).

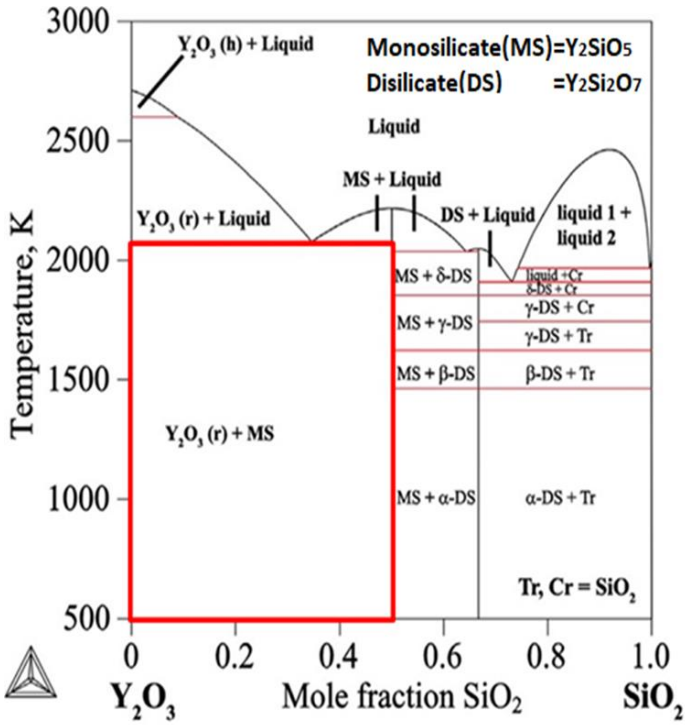

Figure 3: Binary Y_2O_3-SiO_2 phase diagram (60)

4. Experimental Details

4.1. Fabrication of Thin Films and Coatings

The entire set of samples investigated in this thesis work were made via well-known physical vapor deposition (PVD) methods, widely used techniques for the fabrication of thin films and coatings. The specific reasons for using the PVD methods, namely sputter-deposition and pulsed-laser deposition, are: (1) the PVD methods are simple, economically viable, and scalable; (2) these methods have been used in industrial sector to produce films and coatings with desired properties and performance; (3) can combined with different methods to produce coatings with superior properties. The PVD methods became the heart of today's modern electronics, optics, electro-optics, mechanics, electro-mechanics, and energy related technologies, especially with the recent developments in nanoscience and the ability of PVD methods to produce unique materials with desired structure, properties, and performance. Figure 4 illustrates the general path of nanoscale structure creation and characterization utilized in this study. As is the case with most functional materials, particularly those that are expected to be utilized in extreme environmental conditions, a rigorous, multi-stage process of fabrication and characterization is needed to determine optimal materials and configurations. Initial synthesis of the materials in question can be accomplished via multiple means depending on the quality of nanostructured materials produced and potential scalability for industrial applications. Subsequent characterization of the materials produced is then done to determine structure, morphology and chemical nature. Based on these results the effects of synthesis methods/parameters, and post synthesis processing on the materials can be extrapolated and in turn be used to fine tune the fabrication process to achieve desirable traits in the materials in question. The final step in the procedure involves the application of the various nanostructured materials in environments simulating their potential real world uses

and monitoring their performance. The chemical and physical properties of the material can then be directly correlated to their performance characteristics and this knowledge can then be used for manufacturing materials with optimal all-round characteristics.

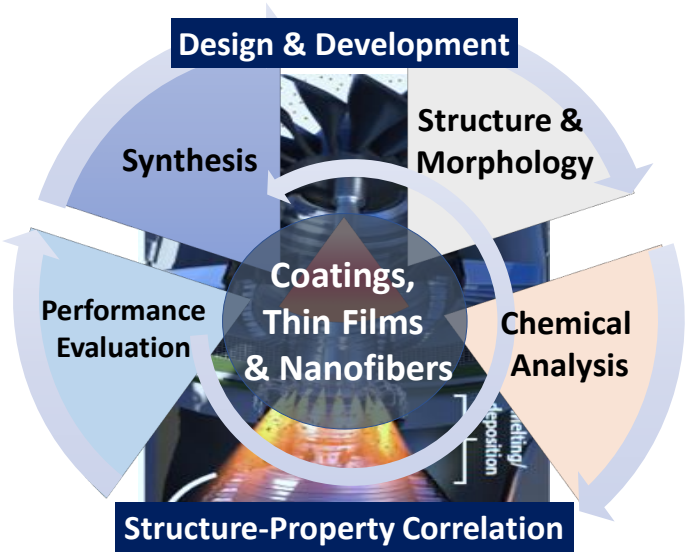

Figure 4: Development and testing path for nanoscale structures

The PVD process refers to a variety of vacuum deposition methods. Most importantly, the physical processes such as sputtering and evaporation are commonly employed in PVD methods to produce a vapor, in the form of atoms, molecules, or ions, of the coating material supplied from a target. The film/coating formation takes place by means of the subsequent transportation of the vapor flux thus generated and deposited on to the substrate surface. Thus, the processes involved in PVD methods for the fabrication of thin films and coatings involve the following steps. (a) The vapor production (of the material to be deposited) by physical means (in a high-temperature vacuum or gaseous plasma system), (b) the vapor transportation to a region of low pressure from its source to the substrate, and (3) finally, the vapor condensation on the substrate resulting in the formation of thin film or coating. Additionally, a brief overview of the PVD methods employed,

specifically sputter deposition and PLD, as well as the general principles/mechanisms involved are presented below.

The most commonly used PVD techniques are: thermal evaporation, electron-beam evaporation, ion plating, sputter-deposition, and pulsed laser deposition (PLD). However, compared with evaporation methods, sputtering and PLD methods are more suitable for handling the complex target materials, such as multi-component ceramics and refractory metals/alloys, which are difficult to deposit by evaporation. Additionally, thin films and coatings produced by sputtering and PLD typically exhibit excellent bonding strength and adhesion to the substrate while resulting in variable microstructures by controlling the process parameters.

The initial set of samples were deposited by radio-frequency (RF) magnetron sputtering process. The process of RF magnetron sputtering makes use of an energetic wave running through an inert gas in a vacuum chamber. This ionizes the inert gas and in turn causes the target material, i.e. the cathode, which will be bombarded by these high energy ions to sputter off surface layer atoms as a fine spray that will cover the desired substrate which is located on the anode. This method makes use of magnets located behind the negative cathode to trap electrons so they are not free to bombard the substrate allowing for faster deposition rates (64).

The system utilized makes use of a pair of cathodes set on the target side and an anode set with the substrate, though for the purpose of this work only one cathode with a Ga_2O_3 target is utilized. As the positively charged gas (Ar) ions accelerate toward the surface of the negatively biased target atoms of the target material will subsequently break off in vapor form. Secondary electrons will also be ejected from the target surface from the ion bombardment though they will not have a significant contribution to sustaining the ejected atoms onto the substrate. These excess electrons are likely to facilitate unwanted heating, but the application of a magnetic field parallel

to the target surface can cause the secondary electrons to circle the magnetic field lines, stay in close proximity to the target, and lead to increased ionization efficiency (65,66).

Pulsed laser deposition is a technique that makes use of high-power laser pulses, typically in the UV wavelengths with nanosecond pulses, to melt, evaporate and ionize from a targets surface. This ablation process creates a short lived, high temperatures plume of plasma that expanse away from the target surface at high speed (with velocities in excess of 106 cm/s in vacuum), after which the ablated material is collected on a substrate located perpendicular to the plume. Multiple variables affect the properties of the resulting thin film one of these is laser fluence (energy of a laser pulse divided by illuminated area measured in J/m^2). With increasing laser fluence, and ablation threshold is reached where laser energy absorption is greater that what is needed for evaporation. This ablation threshold is dependent on the absorption coefficient of material. As fluences values are increased still further, absorption by the ablated species occurs that results in plasma formation at the surface. High energy densities are absorbed by small material volumes, assuming appropriate choices of ablation wavelength and target material, leading to vaporization that is not dependent on the vapor pressures of the constituent cations (67). Another potential variable is background gas pressure (if any). Background gases can serve two main purposes: firstly, they aid the formation of multi-cation thin films that require reactive species, and secondly to reduce kinetic energies in the ablated species (67). These variables, along with the aforementioned laser wavelengths and target materials, and in conjunction with substrate related processes such as temperature can be taken advantage of to fine tune the end results of deposition and film properties. Issues involving PLD include the singular direction and relatively small deposition area of the produced plasma plume (~$1cm^2$ as is the case in the system utilized in

this study), or the potential of the ablated material to contain globules of molten material that can be detrimental to film properties.

The details of the substrate and target materials, fabrication processes, and deposition conditions used in the present work are described in the sections below.

4.1.2 Substrate Materials and Preparation

The gallium oxide samples made by both sputtering and PLD used the Si (100) substrate (University Wafer Inc.) for film deposition. The Si(100) wafers supplied from University Wafer Inc. were subjected thorough cleaning before being placed in their respective deposition chambers. This consisted of cutting the larger wafers into smaller samples with surface areas between ~1-2 cm^2. The samples were then sonicated in 99.9% ethanol for 10 minutes before being removed and allowed to dry. Any residual moisture was dried with nitrogen from an in-lab supply.

4.1.3 Magnetron Sputtered Gallium Oxide

Target material for the RF sputter deposition was obtained from Plasmaterials and consisted of a 2-inch diameter, 0.125-inch-thick, 99.999% purity Ga_2O_3 ceramic target (Figure 5). Nanocrystalline Ga_2O_3 thin films where then deposited on silicon (Si) 100 wafers acting as substrates. The sputtering machine used is the Excel Instruments Model DCSS-12. The deposition chamber figure 6 was evacuated to a base pressure of ~10^{-6} Torr in preparation for deposition. The ceramic target was mounted on a 2-inch sputter gun located a distance of 7 cm from the substrate. For the case of a Ga_2O_3 target a 0.125-inch-thick copper (Cu) backing plate is required to protect the target. To regulate temperature during depositions the sputtering gun was chilled via water with the help of a Polyscience Recirculation Filter chiller. An initial power of 40 W was applied to the target while high purity Argon (Ar) gas was introduced to the chamber. Upon formation of

a steady plasma stream, target power was gradually increased to their respective sputtering power for the final deposition. MKS mass flow meters where used to control Argon and Oxygen (O_2) flow rates within the chamber. To ensure any impurities where removed from the target surface prior to deposition, pre-sputtering was done for 15-20 minutes with a closed shutter between the target and substrate. Once pre-sputtering was completed all samples underwent a total deposition time of 3 hours with a sputtering power of 100 W supplied to the Ga_2O_3 target. The substrates where kept at a temperature of 500 ^oC, registered using a K-type thermocouple located within the sample holder/heater, which is the optimal temperature to produced formation of nanocrystalline β-phase Ga_2O_3 films based on previous trials. To ensure uniformity in surface coverage the substrates where kept constantly rotating during deposition. To study the effect of thermodynamic parameters on the samples' structure, mechanics and properties, the final set of samples were obtained by annealing the films at higher temperatures under post-deposition conditions. Specifically, each sample was subjected to thermal annealing for 1 hour between 600 to 900 °C in the air.

Figure 5: 2-inch diameter Ga_2O_3 Ceramic Target

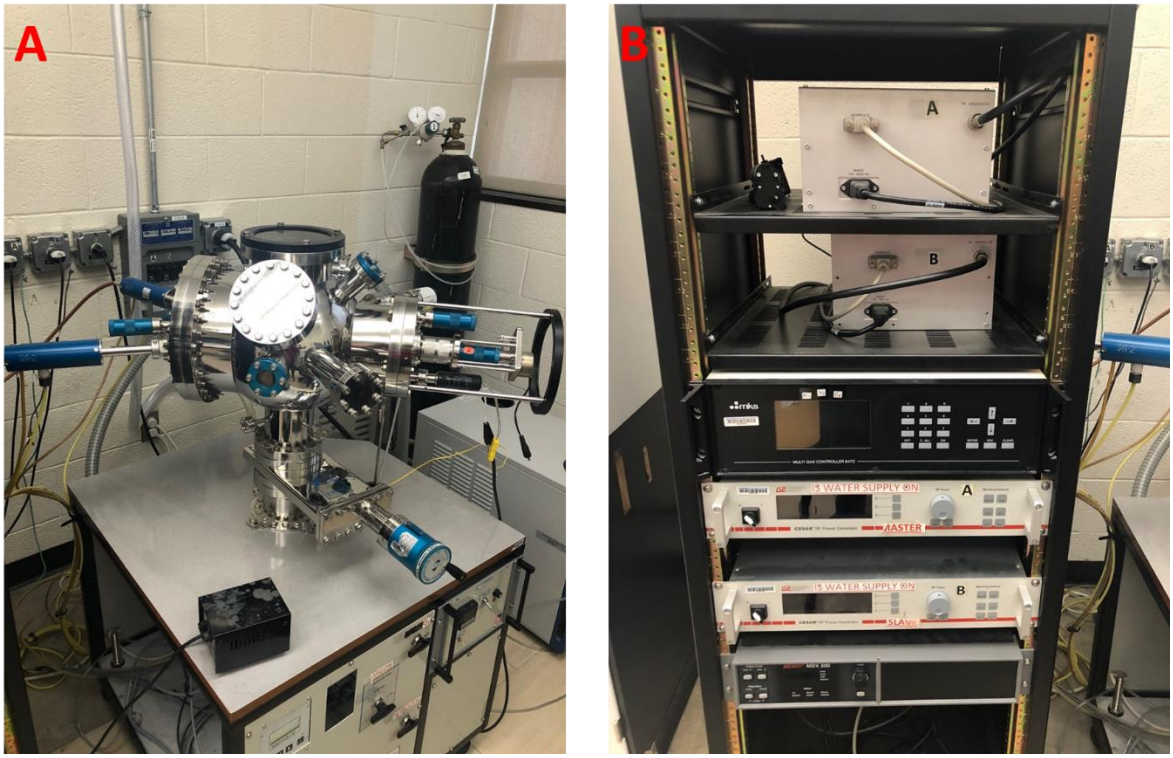

Figure 6: A) RF Magnetron Sputtering Chamber, B) Flow meter and power sources

4.1.4 Pulsed Laser Deposition (PLD) of Gallium Oxide Films

4.1.4.1 Target Preparation

Pure gallium oxide (Ga_2O_3) powder (5N purity) was used as a source material to synthesize the sintered target for laser ablation in a vacuum chamber for pulsed laser deposition (PLD) of Ga_2O_3 thin films. The target was processed to achieve the highest density, typically, as close as possible to match with that of the Ga_2O_3 material. The Ga_2O_3 powder base was mixed with Polyvinyl Alcohol polymer (Sigma Aldrich) by means of thorough mixing. The resulting powder was pressed into pellets of approximately 0.125-inch-thick, 1-inch diameter using the pellet press machine. The pellet thus obtained was subsequently sintered at 1200^{o}C in air for 6 hours. Finally, the target was attached to the PLD target holder for further processing and thin film deposition onto the desired substrate materials.

4.1.4.2. Film Deposition

For the Pulsed Laser deposition (PLD) of Ga-oxide thin films, Ga_2O_3 target (prepared as per the detailed mentioned in previous section) was placed on individual mounts before being placed within the deposition chamber figure 7. The background chamber pressure was reduced to ~10^{-6} Torr before oxygen was introduced into the chamber. The laser unit figure 8, which is a KrF excimer laser with a wavelength of 248nm and 220 mJ of cumulative energy (COMPex-Pro, Coherent) was then utilized to ablate the Ga_2O_3 target. The target was located 45 mm from the substrate. A 5 Hz pulse frequency was used for ablation while the Ga_2O_3 target was kept constantly rotating to maximize potential of even distribution of ablated material from across the target. This both served to extend usable target life, and keep the distance between point of ablation and the substrate as constant as possible to ensure a consistent deposition profile. To ensure no impurities

where present in the deposition, pre-ablation of the target was done for ~200 pulses with a shutter closed between the target and substrate. The total number of pulses for deposition was kept constant at 2000, which led to film thicknesses between 150-250 nm depending on the temperature which varied between room temperature (~25^{o}C) up to 700 ^{o}C. The use of the sintered Ga_2O_3 target and high-energy laser processing under equipment specific optimized thermodynamic conditions was key to the production of the needed high energy plasma plume from the target. The energized particles where directed toward the substrate as shown in figure 9 where, under optimum conditions, the expected nanostructured films are shown schematically. It should be noted that while in-situ chamber pressures where kept high, the reduction in film thicknesses with higher temperatures implies adatom out diffusion during the nano-columnar growth process.

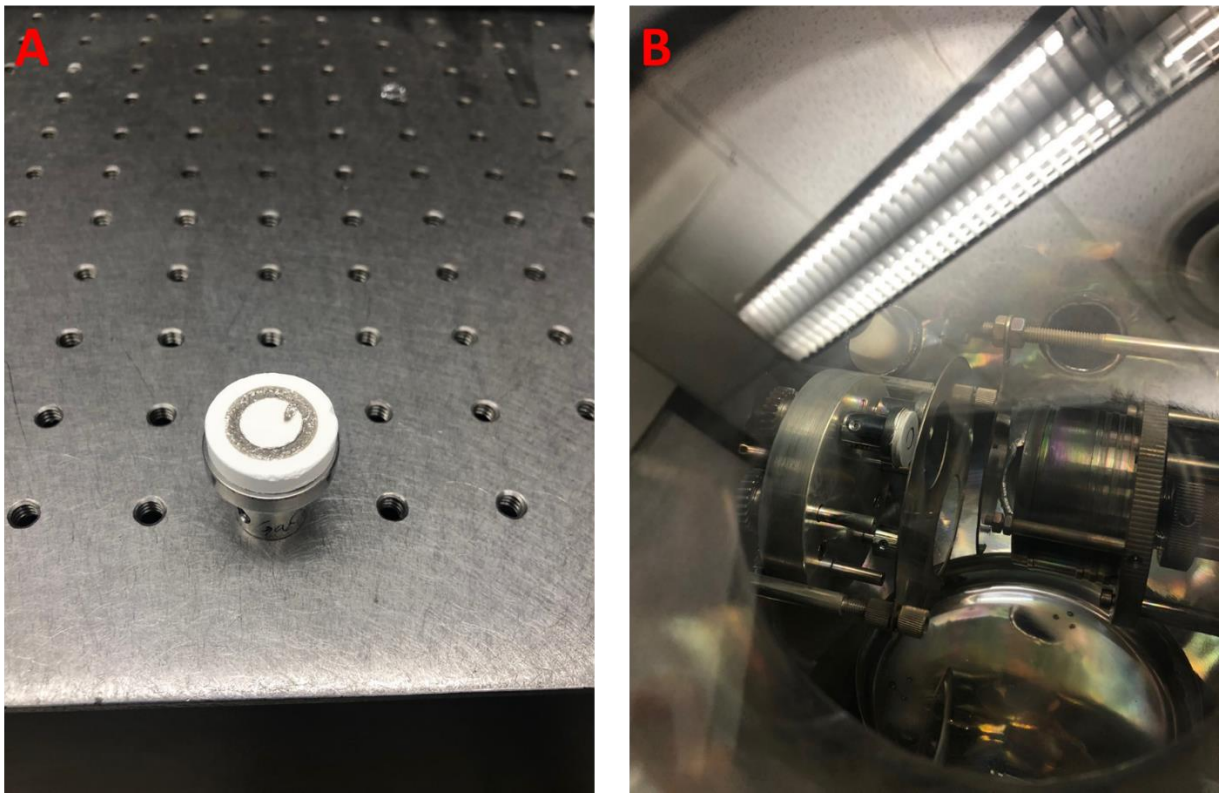

Figure 7: A) PLD target, B) Deposition chamber

Figure 8: KrF laser unit

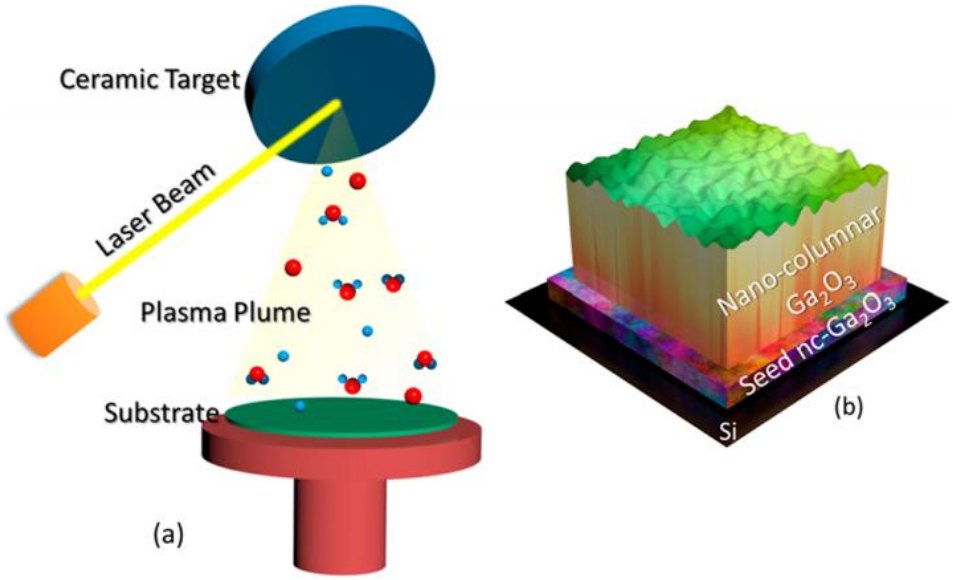

Figure 9: A) Schematic diagram showing PLD of β-Ga_2O_3. B) Schematic of a nanostructured Ga_2O_3 thin film on Si.

4.1.5 Gallium Oxide Nanofibers

A precursor solution was initially formulated before spinning of fibers commenced, with variations on exact polymer-precursor-solvent ratios being tested to ensure maximum efficacy in deposition. A variety of Gallium precursors were also reviewed with final selection being based primarily on safety of handling and ease of acquisition. With these conditions the following served as the basis for the synthesis of Ga_2O_3 nanofibers. Gallium nitrate was used as the gallium precursor for nanofiber production. The electrospinning solution was prepared with a 1:1 weight ratio of ethanol and deionized water to which varying weight percentages, 3.25%-15%, of gallium nitrate were added. Finally, 10 wt% of polyvinyl pyrrolidone was added to ensure sufficient viscosity for the electrospinning. Actual electrospinning was done on a Bioinicia Fluidnatek Le-10 benchtop electrospinning system (figure 10). The metal syringe was set constant motion along a sliding track to ensure even deposition, while fibers were collected on rotating drum covered in

plastic sheeting to ease removal of fibers. Flow rates for the solution varied with environmental conditions such as temperature and humidity as well as gallium precursor content and often had to be adjusted during each deposition. The machine was run until 1 ml of solution was spun, at which point the plastic sheeting was removed, and the fibers peeled off for heat treatment. The fibers were finally subjected to post-processing annealing at 700-900°C in air for 2 h to form gallium oxide.

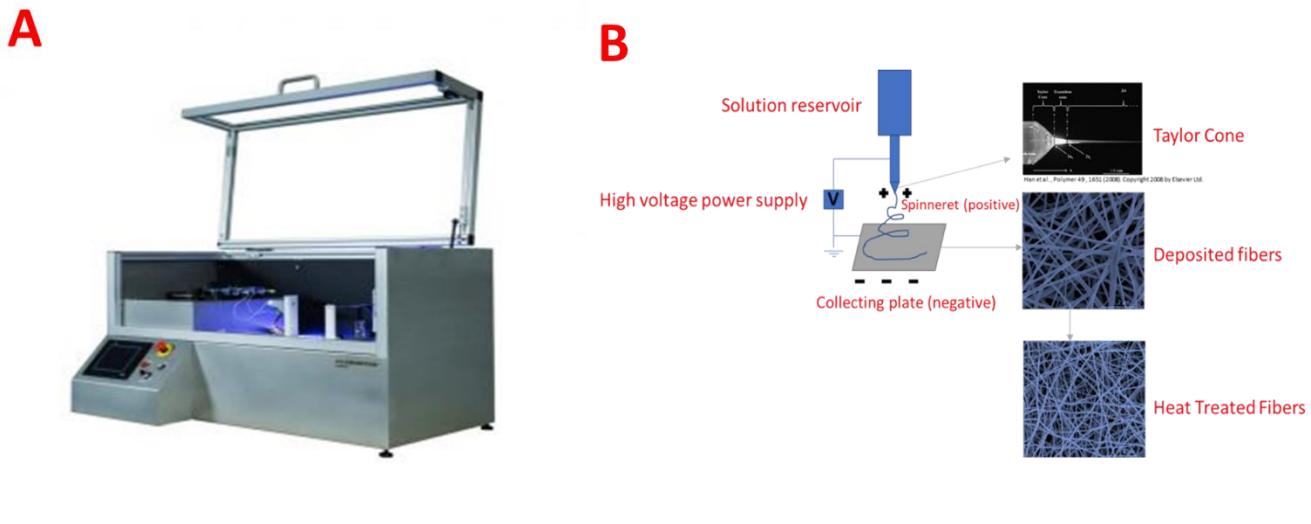

Figure 10: A) Bioinicia Fluidnatek Le-10 benchtop electrospinning system (Bioinicia.com), B) diagram of electrospinning process

4.1.6 Environmental Barrier Coating (EBC)

To determine the effects of substrates on adherence and interaction at the coating surface the YSiFe coating was applied to both alumina substrates and a simulated full EBC system deposited on a SiC button. The 1 mm thick plane alumina substrates (Ceramtec) provide high melting points as well as a high degree of inertness. This allows for longer infiltration tests at higher temperatures. For the full system testing a 5mm SiC button was coated with a Si bond coat

followed by a YDS layer. For comparison testing of pure YDS when exposed to the new CMAS compositions separate samples with the YDS coating were placed on the same type of alumina substrates as the YSiFe coatings without a bond layer.

Reactive magnetron sputtering was used to achieve YSiFe coatings with constant stoichiometry, of approximately 25 µm thickness. A batch time magnetron sputtering facility (Z 400, Systec SVS vacuum coatings) was used employing a yttrium-iron target power of 800 W along with a silicon target at a power of 300 W. The yttrium-iron target was custom manufactured on-site by drilling into a existing yttrium target and inserting pure iron pellets into the resultant holes. Total pressure in the deposition chamber was 4.4 × 10-3 mbar in Ar (23 sccm) and O_2 (6 sccm). Before actual deposition samples were etched in Ar (10 sccm) for 20 min (pulse rate 200 kHz, 3 µs, 250V). The sample grew at a sputter rate of 3.8 µm/h while being rotated at 10-12 rpm. Substrate temperature varied from 150 – 300 °C during deposition.

For the YDS coating directly applied to alumina substrates, yttrium and silicon targets were employed instead. The yttrium target power was set to 800 W, while the silicon target was set to 300 W at chamber pressure of 4.1 × 10-3 mbar in Ar (21 sccm) and O2 (6sccm). Samples were coated at a sputter rate of approximately 4.3 µm/h for a total thickness between 15-20 µm. Samples were rotated at 20 rpm, and as with the YSiFe coatings, the substrates were etched in Ar (10 sccm) for 20 min (pulse rate 200 kHz, 3 µs, 250V) before deposition.

As the focus of this section of the study was to determine the effects of variances in CMAS composition on EBS integrity a variety of compositions were selected for testing. One natural volcanic ash from the Popocatepetl volcano along with 3 synthesized variations were utilized for infiltration tests. The USCB CMAS, CMAS 1 and 2 where synthesized at DLR with the largest

difference based on calcium oxide levels within the compositions. A summary of the CMAS samples used, their compositions, and melting temperatures are compiled in table 1.

Table 1: Composition and melting points of tested CMAS variants

CMAS ID	CaO(Mol. %)	MgO(Mol. %)	$AlO_{1.5}$(Mol. %)	SiO_2(Mol. %)	FeO(Mol. %)	TiO_2(Mol. %)	Other Na/k/Mn/P oxide(Mol. %)	Onset of Melting (°C)	Melting Max (°C)
CMAS1	22.1	11.2	19.9	37.5	1.4	-	-	1225	1259
CMAS2	28.1	10.3	18.4	34.7	1.3	-	-	1215	1247
UCSB CMAS	33.3	9.1	12.3	45.4	-	-	-	1233	1249
Popocatepetl	0.01	0.3	6.3	66.9	1.4	15.8	15.8	1100	1175

Based on previous work done at DLR a quench type heat treatment for the amorphous YSiFe coating was performed to facilitate and stabilize the desired phases (22). The heat treatments took place in a thermal cyclic furnace or tube furnace as availability dictated. The furnace was pre-heated to 1250 °C at which point the samples were introduced to be rapidly heated. The samples underwent isothermal heating in air for 1 hour at 1250 °C then quickly removed from the furnace and air quenched to room temperature through the use of fans.

A series of short-term infiltration test was carried out on the prepared YSiFe and YDS coatings. CMAS was applied to the heat-treated coatings in the amount of 10 mg/cm^2 on top of an approximate 1 cm x 1 cm area on the sample or as close to this as the sample size would allow. To ensure homogeneity in the applied layer, the CMAS was mixed with a few drops of ethanol and the suspension was applied to the sample. The sample was then allowed to dry before being placed in a pre-heated tube chamber furnace at 1300 °C. Total exposure times were 10 minutes for an initial test run, and then either 30 minutes or 1hr. Once heating was done, the samples where quickly removed from the furnace and air cooled to room temperature using fans.

In preparation for final characterization the samples went through a standard metallographic sample preparation procedure. Cross-sectional analysis of the sample was facilitated by the use of precision cut-ff machines set to a cutting rate of 0.005 mm/s utilizing a diamond cutting disk. Before cutting the samples were stabilized using a two-component epoxy adhesive (Gatan). The purpose of the adhesive is to fill any open gaps to provide more stability when cutting, grinding, and polishing the sample. The sample, cut through the primary part of the CMAS melt/coating interface, was kept upright via metal clips and hot-embedded in electrically conductive synthetic embedding material (Struers, Polyfast). Embedding was performed at 180°C for 6 minutes while pressure was increased from 50N to 75N after 3 minutes. Following an additional 6 minutes. the sample was water cooled before removal. The sample was then polished using a series of diamond discs ranging from 220 grit to 8 µm, followed with an alcoholic diamond suspension, then a Al_2O_3 oxide suspension (Masterprep), before completing a final cleaning with detergent and water for 20 minutes. All polishing was done with an applied pressure of 10 N. A thin platinum layer was applied via sputtering for 30 seconds before beginning SEM analysis to prevent charging effects.

4.2 Characterization

4.2.1 X-ray Diffraction (GIXRD and Powder)

Grazing incidence X-ray diffraction is a method employed with thin films or other instances where there is insufficient material for high quality signals in more conventional XRD measurements. This method makes use of the same basic principles of traditional XRD involving the use of a monochromatic X-ray is emitted and directed toward a material whose atoms cause the x-rays to diffract. Based on the crystal structure of the material, the scattered x-rays will

undergo constructive or destructive interferences. The diffracted x-rays are then collected by a detector at varying angles to satisfy Bragg's law in order to identify phases/unit cells.

$$n\lambda = 2dSin\theta \quad (5)$$

In this equation n is the integer, θ is Bragg's angle, d is the interplanar distance, and λ is the x-ray wavelength.

In the case of the RF-magnetron sputtered Ga_2O_3 thin films this process was undertaken on Bruker D8 advance setup using Cu Kα radiation (λ= 1.54 Angstrom). All measurements were taken at room temperature with the grazing incident angle set to 1^o for income x-rays to maximize exposure to the surface and layers of the films. The detector scanned from 10-67^o at a rate of 0.5 s/step. Similar parameters where used on the thin films prepared via pulsed laser deposition but where performed on a Rigaku Smartlab Diffractometer in 1D mode with a HyPix 3000 high energy resolution 2D hybrid pixel array detector.

As the gallium oxide nanofibers proved too brittle for traditional or GIXRD measurements, the calcined fibers where lightly ground to powder form before being placed on a glass slide with structural analysis performed on a Rigaku Benchtop Powder X-Ray Diffractometer. Scanning parameters where set to 10^o – 80^o (2θ range), step size – 0.02^o and scan rate – 0.6 ^{o}/min.

4.2.2 Scanning Electron Microscopy

Scanning Electron Microscopy (SEM) makes use of a very focused beam of electrons to observe surface features of samples. High energy electrons are emitted from an electron gun that are directed at a specimen to scan the surface and create an image via a rastering process where the beam serves to illuminate a single point at a time.

For the gallium oxide nanofibers, the surface morphology and microstructural features of Ga_2O_3 fibers are important and reveal information about the samples processed under variable synthetic conditions as well as post-processing effects. Therefore, Scanning Electron microscopy (Hitachi – 4800) was used to analyze Ga_2O_3 nanofibers. Small sheets of the samples were placed on circular stages of approximately 0.5-inch diameter with double sized carbon tape. Electron incident current and voltage was varied to obtain the best resolution images possible for each sample prior to imaging, the samples were sputter coated with silver to avoid the charging effect, a common problem in imaging insulating samples. Once sample images where saved, Image J software, was used to determine fiber diameters and lengths (67).

In the case of the mounted environmental barrier coating samples microstructural analysis of the samples was undertaken using SEM (DSM Ultra 55, Carl Zeiss NTS) which had been also equipped with an energy dispersive X-ray spectroscopy (EDS) system (Inca, Oxford Instruments). Pictures of samples were taken with the detector set to an accelerating voltage of 5kV using the secondary electron setting (SE2), with the aperture set to 30 μm. The angle selective backscatter (AsB) electron detector set to an accelerating voltage of 10-15 kV was then utilized to show more contrast and provide topographical clarity.

4.2.2.1 Scanning Electron Microscopy (SEM) and Energy Dispersive X-ray Spectroscopy

Energy Dispersive X-ray Spectroscopy (EDS) is an analytical technique that is used for chemical and elemental analysis of a sample which is reliant on a source of x-ray excitation (a beam of electrons in this case) within a material. The number and energy of the x-rays emitted from a material once excited can be measured via spectrometer and used to determine sample composition. As was the case with the SEM measurements, the EDS measurements of the EBC samples utilized the angle selective backscatter electron detector with an associated voltage

between 10-15 kV. Working distance was set as approximately 8mm. EDS elemental mapping, in conjunction with area and spot analysis of the captured images was done to determine the chemical composition of the remaining coating, reaction layer/products, and any changes to the CMAS melts themselves.

4.2.3 Transmission Electron Microscopy

Transmission electron microscopy (TEM) is an analysis technique making use of a high energy, focused beam of electrons emitted from a tungsten filament. A high vacuum is needed for the optical system of the microscope to reside in ensure collisions of electrons with air molecules and the resulting scattering of electrons ins avoided. A series of magnetic coils placed at specific intervals along the column act as an electromagnetic condensing lens to focus the electron beam on the sample. A focused ion beam (FIB) is used to remove a small sliver from the larger sample, which is subsequently placed in the path of the electron beam. As the beam of electrons is partially transmitted through the thin sample, they will allow for insights into the sample structure. A series of fluorescent screens/photographic plates/ or light sensitive sensors will record images of spatial variations in the electron beam information after it has been magnified by the magnetic lenses.

For the PLD grown gallium oxide samples TEM characterization was carried out on a Thermo Scientific Titan Themis 200 G2 probe aberration-corrected system which had been equipped with a SuperX energy-dispersive X-ray Spectrometer and ran at 200 kV. Specimens where prepared using a FEI Scios FIB and SEM dual beam system following standard protocol for TEM preparation. This included using an electron beam at 5 kV and 1.6 nA, to deposit a thin C protection layer of 15 μm × 2 μm on the Ga_2O_3 film grown on a Si substrate, and then a 15 μm × 2 μm × 2 μm Pt protection film was deposited on top of the C protection layer at 30 kV and 300 pA, followed by rough cutting, cleaning cut, J-cut, and lamellae transfer out of the substrate to a

TEM grid. Further FIB cleaning at 5 kV and 48 pA as well as at 2 kV and 27 pA was performed on the final thinned specimen to removed excess contaminated layers. All TEM data processing was carried out using relevant offline data processing software from Thermo Scientific in addition to Image J software to run radial profile analysis of selective area electron diffraction (SAED)

The high-resolution transmission electron microscopy (JEOL JEM-2100F TEM equipped with Oxford AZtec energy dispersive x-ray spectrometer and Gatan Tridiem GIF electron energy loss spectrometer) measurements were made to analyze the surface morphology and crystal symmetry of Ga_2O_3 nanofibers. Bright field images and selected area electron diffraction (SAED) patterns were recorded. All the measurements and imaging analysis was made on the Ga_2O_3 nanofibers samples prepared under variable synthetic conditions. In order to prepare TEM sample, a small amount of Ga_2O_3 nanofiber sample was diluted with ethanol, suspension is sonicated, a single drop of the resulting suspension is placed onto a carbon-coated copper grid and allowed to dry in air.

4.2.4 X-ray Photoelectron Spectroscopy

X-ray Photo electron spectroscopy (XPS) was utilized to determine surface chemistry and film stoichiometry. This technique makes use of x-ray inelastic scattering phenomena to quantify chemical data. The surface atoms of a sample when exposed to high energy x-rays will undergo electron emission, known as the photoelectric effect. The kinetic energy of the emitted electron will be measured by:

$$KE = hv - BE - \Phi \quad (6)$$

In which KE represents kinetic energy of the electrons, h is the Planck constant, v is frequency, BE is binding energy and Φ is the spectrometer work function (68). Photon energy must exceed

that of the work function or no electrons will be emitted. Each emitted electron carries kinetic energy equal to the difference between the photon and binding energy. Kinetic energy can thus be used to find the concentration of surface elements since each element possesses unique sets of core levels. Additionally, elemental binding energy variations or chemical shifts can be used to determine the chemical state of the material (70).

For the PLD grown gallium oxide films, XPS scans where performed using a Kratos Axis Ultra DLD spectrometer equipped with an AL Kα monochromatic x-ray source rated at 1486.6 eV. The system made use of a high-resolution hemispherical analyzer. The survey scans on the samples were carried out at pass energies of 80 or 160 eV. High resolution scans where performed at 20 eV. A 5 keV Ar^+ ion beam was rastered over a 2x2 mm^2 area of the sample for depth profiling. Additionally, the high resolution xps spectra were also recorded at 20 eV with a step size of .1 eV. For the total analysis area, the 20 eV pass energy is referred to the full with half maximum of .59 eV for Ag $3d_{5/2}$. Depth profiling of the data was performed using CasaXPS software via Gaussian/Lorentzian (Gl(30)) line shape along with a Shirley background correction. There was an approximate error for element concentrations of +/- 0.01 at. % for Ga and +/- 0.1 at. % for oxygen.

4.2.5 Atomic Force Microscopy

To determine the surface morphology of the RF magnetron deposited Gallium oxide films Atomic Force Microscopy (AFM) was employed. Parameters of particular interest were e average surface roughness (R_a), root-mean-square roughness (R_q), ten-point average roughness (R_Z), and the third highest peak to third lowest valley height (R_{3Zi}). Measurements were performed on an Ntegra Mt-MDT system in contact mode once double sized tape had been utilized to affix the samples to onto sapphire substrates. The probe utilized had a 0.01-0.50 N/m force constant (Nt-

MDT CSG/10). Multiple surface measurements were undertaken to ensure tip quality, which was qualitatively assessed via examination of resulting AFM imagers for clarity and noticeable artifacts. Calibration was done in accordance with manufacturer supplied standards. Average surface roughness was determined using:

In the equation Z(x) represents the function describing the surface profile analyzed in terms of height and position in terms of evaluation length L. R_a represents the arithmetic average of the absolute values for surface height deviations as determined from the mean plane. 65,536 sampling points were taken from each 500nm x 500nm image. R_q stands for the standard deviation of the variance from the mean plane in reference to the image sampling points. These 2 values play a primary role in classifying surfaces of the same type that also have similar manufactured origins. Finally, symmetry of distribution is characterized by surface Skewness, which along with kurtosis parameters play a significant role in understanding surface features.

4.2.6 UV-Vis Spectroscopy

Diffuse reflectance spectroscopy was utilized to determine the optical absorption behavior of the PLD grown gallium oxide samples. A Jasco V-770 UV-visible Spectrophotometer with an optical resolution of 0.3nm, was used measurements. PL measurements were undertaken on the as grown thin films via an 80 MHz 100 fs Ti: sapphire laser, which was equipped with an additional third-harmonic generator. The cumulative power was 10 W/cm^2 and the excitation energy was set at 180 nm, both of which were kept constant during measurement. Emitted photons were subjected to a 0.02 nm resolution monochromator with a subsequent photomultiplier tube detector.

4.2.7 Spectroscopic Ellipsometry

Spectroscopic Ellipsometry (SE) was utilized to find surface interface characteristics and optical properties of the RF-magnetron sputtered Gallium oxide samples. This methodology utilized a light source emitting through a polarizer that will fall onto a sample, and after reflection it will pass through a second polarizer and be picked up by a detector. Ellipsometry measures the reflectance ratio ρ of a system and then derives the physical properties of the reflected light specifically ψ (amplitude component) and Δ (phase difference) via:

$$\rho = \frac{r_p}{r_s} = tan\psi(e^{i\Delta}) \tag{7}$$

Where r_p and r_s represent the components of the polarized light incident upon the sample oscillating parallel and perpendicular to the plane of incidence respectively.

For the thin films ψ and Δ were determined over a wavelength range from 200-1600 nm at 300 k in air. A J. A. Woollam vertical, variable-angle spectroscopic ellipsometer along with a computer controlled Berek wave plate compensator was used for measurements. 60°, 65°, and 70° were the angles of incidence used during measurements, followed by post analysis of the data using commercially available WVASE32 software. The Levanberg-Marquardt regression algorithm was employed to minimize mean-squared error (MSE):

$$\text{MSE} = \frac{1}{2N-M}\sum_{i=1}^{n}\left[\left\{\frac{(\Psi_{exp}-\Psi_{calc})}{\sigma_{\Psi_i}^{exp}}\right\}^2 + \left\{\frac{(\Delta_{exp}-\Delta_{calc})}{\sigma_{\Delta_i}^{exp}}\right\}^2\right] \tag{8}$$

Here Ψ_{exp}, Ψ_{calc}, and Δ_{exp}, Δ_{calc} are the measured and calculated ellipsometry functions. M represents the number of fitted parameters in the optical model, while N is the number of measured Ψ, Δ pairs. σ represents the standard deviations of the data points. Multiple measurements and analyses were completed to account for optical inhomogeneity.

The extinction coefficients (k) and refractive index (n) where derived from the data after fitting the as-recorded measurements to a Cauchy dispersion model (determined as a function of wavelength λ):

$$n(\lambda) = A + {}^{B}/_{\lambda^2} + {}^{C}/_{\lambda^4} \quad (9)$$

$$k(\lambda) = d + {}^{e}/_{\lambda^2} + {}^{f}/_{\lambda^4} \quad (10)$$

Within the function for the refractive index, A, B and, C represent constants that dominate n(λ) for long, middling, and shorter wavelengths respectively. For the function in reference k, the values represented by d, e, and f are constants specific to the material (71).

4.2.8 Electrical Characterization

Electrical resistivity of the RF magnetron sputtering samples was measured utilizing the four-point Van-Der Pauw method which consisted of 4 electrical contacts on the samples constructed with a 2-part epoxy and silver wires. In the first set of measurements, current was applied to an arbitrary pair of electrodes with the subsequent voltage across the remaining pair of electrodes being measured. This was repeated for a total of 8 combinations of contact configurations. A Keithley 220 programmable current source was utilized which applied a current of 2 mA. Voltage was measured by a Keithley 196 sensitive digital voltmeter, in conjunction with a 196 DMM system to measure the intervening currents. Switching between currents was accomplished via a Keithley 2001 switch. Automatic data recording from the various meters was done using a LABVIEW data acquisition system with a IEEE-488 GPIB. The Van Der Pauw principle was used to determine final resistivity after taking into account sample thickness, shape factor, and other limitations.

$$R_{(=)} = R_{(AB,CD)} = \frac{V_C - V_D}{I_{AB}} \tag{11}$$

$$e^{-R_{(=)} \cdot \frac{\pi d}{\rho}} + e^{-R_{(\|)} \cdot \frac{\pi d}{\rho}} = 1 \tag{12}$$

V_C represents voltage of the contact measured against ground and I_{AB} is the current applied between the contacts A and B, starting at A and ending at B. Through cyclical changing of the contacts, the vertical Van-Der Pauw resistance can be determined.

4.2.9 Nano Mechanical Characterization

The RF Magnetron sputtered samples underwent nanomechanical characterization to determine their hardness (H) and reduced elastic modulus (E_r). This was accomplished via nano indentation testing performed on a Hysitron T1750 Tribo Nanoindentor. A triangular pyramid Berkovich diamond indenter was used which possessed a normal angle of 65.3^o between the tip axis and the triangular pyramid faces. The apex possesses an effective size of approximately 100nm. The samples where automatically indented by the system with a total of 7 indents in a "H" pattern with one central indent and three vertical indents to a side. This pattern was recommended for indenter tip calibrations performed on fused quartz with a spacing of ~15µm apart for the indents. The recorded load vs displacement curves were then compared to the original probe calibration sheets. The loading and unloading curves where then used to calculate the mechanical characteristics of the films using the Oliver and Pharr method (72).

$$E_r = \frac{\sqrt{\pi}}{2} \frac{S}{\sqrt{A}}; \; H = \frac{P_{max}}{A} \tag{13}$$

Where S represents stiffness of the film derived from the slope of the unloading curve, P_{max} is the maximum load, and A is defined as the aera of contact at the peak load.

Additionally, adhesion properties of the films were determined using scratch testing. This was an important property to determine as adhesion to a given substrate is critical in determining coating quality and endurance for nanoscale films. The same Hysitron T1750 Tribo nano indenter was utilized to perform the test. Samples were kept at room temperature under a continuously increasing load from 0 to 8000 µN via the same triangular pyramid tip used in the indentation tests. Total scratch length was 16 µm with a scratch speed of 0.18 µm/s

5. Results and Discussion

5.1. RF Magnetron Sputtered Gallium Oxide

5.1.1 Surface Morphology

The AFM patterns of as-deposited and annealed β-Ga_2O_3 films are shown in Figures 11-13. Figure 11 depicts topographic images of the thin films' morphology while the corresponding grain area analysis is illustrated in Figure 12. The surface roughness and grain histograms are shown in Figure 13, respectively. The morphology of the nanoparticulate film surfaces for as-deposited Ga_2O_3 films demonstrate conically shaped grains distributed uniformly over the film surface of the intrinsic Ga_2O_3 films while the root-mean-square surface roughness value was ~1 nm. These reported AFM values for intrinsic Ga_2O_3 films are in excellent agreement with those reported in the literature (40,71). It is clear from results presented here that increasing the annealing temperature produces substantial changes in the surface morphology of the Ga_2O_3 films. The increasing grain size and surface roughness values of the Ga_2O_3 films exhibit a clear dependence on the annealing temperature (Figure 13). Also, as noted in Figure 13a, the average roughness (Ra) is well correlated with the root mean square (Rq). The surface roughness increases with increasing temperature until a temperature of 800 °C, and at this point, there is a large decrease in surface roughness. One can see from the grain area histogram (Figure 13b) that, between 700 and 800 °C, there are competitive bimodal phases contributed to grains of different areas in contrast to grain analysis on as-deposited films and those annealed at the highest annealing temperature (900 °C), where a much more consistent distribution of grains appears. The single numerical parameters, Ra and Rq, are useful to classify the same type of surfaces which have been produced using the same method. The annealing temperature has a dramatic effect on surface roughness, especially when

the annealing temperature exceeds 700 °C. While these results agree, in general, with results reported in literature for Ga_2O_3 films fabricated by physical methods, differences arise due to the differences in synthesis conditions adopted for deposition, substrate materials, and physical parameters (thickness, density, etc.). For instance, while the noted trend is very similar to annealing behavior of polycrystalline Ga_2O_3 films made by anodic oxidation of nGaAs wafers, there are significant difference in the observed values of roughness values and grain size and shapes (72). The Ga_2O_3 anodic films exhibit linear grain sizes, where grains were in the form of squares with a side length of 600−700 nm (72). After annealing, Ga_2O_3 anodic film roughness increased to 100−120 nm, which exceedingly higher compared to sputter deposited films. While the trend is similar, the differences are primarily attributed to the preparation methods, that is, anodic oxidation under oxygen plasma versus sputter deposition under reactive conditions. The later results in more finer grains while Ga_2O_3 anodic films tend to result in larger or micro size grains rather than nanoscale dimensions. On the other hand, our results closely agree with those reported for Ga_2O_3 films made by pulsed laser deposition. Similar to sputter-deposited Ga_2O_3 films, PLD Ga_2O_3 films were also of the same composition, no matter the different temperatures of annealing (30). The PLD Ga_2O_3 films annealed at 800 °C exhibit a smoother surface and relatively larger feature size (30). Similar to PLD Ga_2O_3 films, the sputter-deposited films also attain the maximum grain size and lower surface roughness for annealing at 800−900 °C.

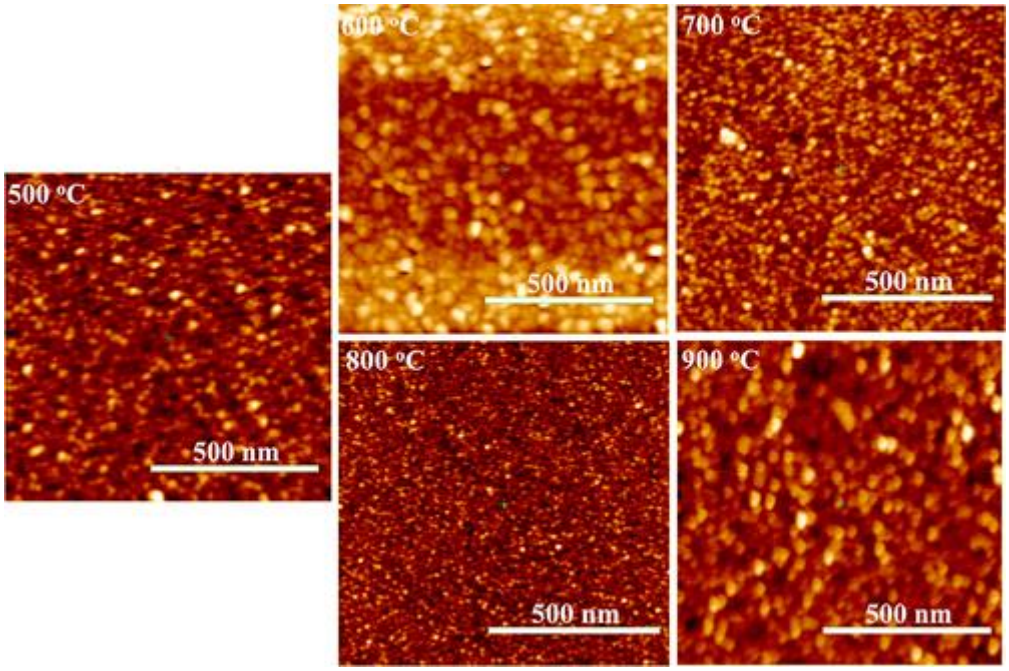

Figure 11: AFM morphology micrographs of Ga_2O_3 films as a function of annealing temperature.

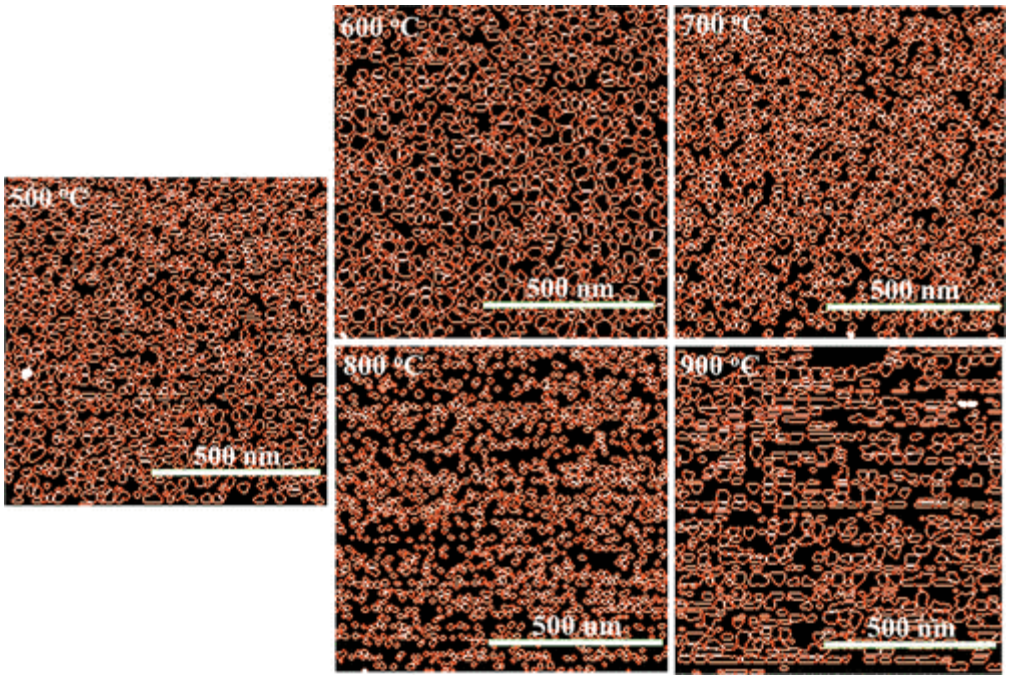

Figure 12: AFM grain analysis micrographs of Ga_2O_3 films as a function of annealing temperature.

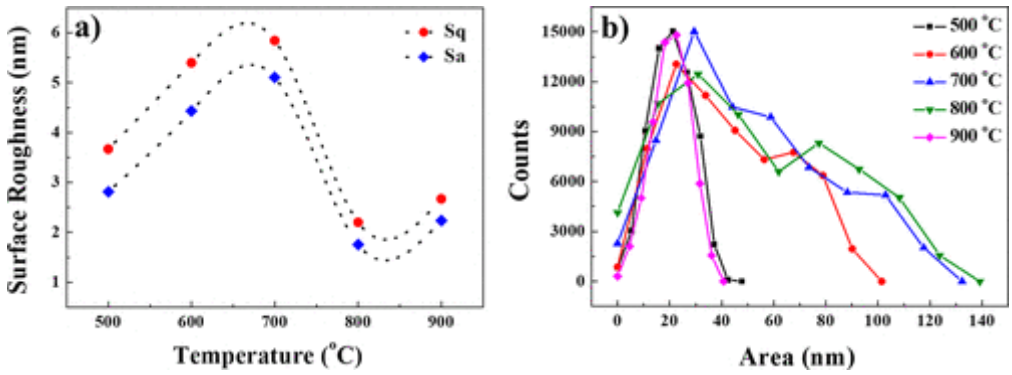

Figure 13: AFM surface roughness analysis and correlation between roughness and temperature (a) and grain analysis histograms (b).

5.1.2 Crystal Chemistry, Crystal Growth, and Mechanism

Figure 14a shows the GIXRD patterns for the both the as deposited and annealed Ga_2O_3 films. The results indicate annealing temperatures play a substantial role in determining crystal structure. The as-deposited nanocrystalline Ga_2O_3 sample corresponds to the monoclinic β-phase (space group C2/m). The XRD peaks, due to diffraction from crystal planes of (−201), (400), (002), and (−204), which correlate to 2θ values of 18.95, 30.05, 31.74, and 64.17, in accordance with JCPDS (00-043-1012). Significant changes are not visible in the XRD patterns until temperatures of 700 °C. The peaks become shaper with an intensity increase in addition to the appearance of (104), (113), and (−211) peaks. This observation indicates the thermally induced crystallization leading to further structural evolution in the sputter-deposited Ga_2O_3 films. Further increase in the annealing temperature to 900 °C induces texturing of the Ga_2O_3 films, as can be seen in XRD data (Figure 4a). The peak intensity for (400) and (−201) reflections increases with thermal annealing indicating the preferential growth or texturing of the Ga_2O_3 films. Specifically, the (400) peak intensity increases considerably while the peak becomes narrower with a noticeable reduction in full width at half-maximum (FWHM) indicating a higher crystallinity. The results are in general

agreement with those reported for MOCVD Ga-oxide films (27,28,31). Those samples exhibited an amorphous-to-crystalline structural transformation with improved crystalline quality and a smoother surface structure with an annealing temperature of 900 °C (27,28). Similarly, under thermal annealing, PLD β-Ga_2O_3 films on sapphire substrates also exhibited the typical behavior of polycrystalline nature and texturing upon annealing at temperatures of 800−1000 °C, although annealing at the high end of this temperature range resulted in Al diffusion from the substrate (31). Thus, from the results presented in this work, in conjunction with previous results available in the literature, it can be conclusively stated that the thermal annealing at higher temperatures 800−900 °C induces crystallization and introduces changes in the crystallite size and morphology. To understand the effect of thermal annealing on crystallinity and crystal growth, the average crystallite size of the sputter-deposited nanocrystalline Ga_2O_3 films is calculated using the Scherrer's equation

$$d = \frac{0.9\lambda}{\beta \cos \theta} \tag{14}$$

where d represents the average crystallite size, the angle of the peak is θ, λ is the wavelength of x-rays, and β is the width of the peak at its half intensity. The intense (400) peak data was used for calculations. Similarly, determining the microstrain in the Ga_2O_3 films is made by further analysis of the XRD data. The origin of the microstrain is related to the lattice misfit, which, in turn, depends upon the fabrication parameters. The microstrain is calculated using the relation (73):

$$\varepsilon = \frac{\beta \cos \theta}{4} \tag{15}$$

In this equation β once again is the full width at half-maximum while θ is instead the Bragg angle. The variation of the average crystallite size and microstrain with annealing temperature is shown in Figure 4b. The average crystallite size increases from 10 to 16 (±1) nm with the increase of

temperature from 500 to 900 °C. The nature of annealing, crystallization (explained in XRD) and grain growth mechanism plays a critical role for the change in the average crystallite size. The decrease in the strain values implies that the films becoming strain free and thermal annealing improves the crystalline nature of the Ga_2O_3 films. Finally, to understand the fundamental mechanism of crystallization and growth behavior in nanocrystalline Ga_2O_3 films under the effect of increasing thermal annealing temperature, the data obtained from XRD and AFM were analyzed in terms of simple models available in the literature. Temperature, a key thermodynamic parameter, plays an major role in deciding the microstructure and properties of thin films produced by the physical or chemical deposition methods (21,68,74). Usually, when the effect of temperature is not sufficient to produce, amorphous films are the result, while increasing annealing temperature or time of annealing can induce sufficient atom mobility and, hence, crystallization in the films (68,69,74-76). From XRD and AFM data analyses, it can be observed that the increasing annealing temperature improves crystallization and induces texturing. As the average crystallite size and morphology changes, the enlarged grain-size, in addition to their distribution characteristics, a direct result of further increase in annealing temperature, can only be due to restructuring of the Ga_2O_3 films on the Si(100) substrate. The crystallite size data were analyzed and fit to the Arrhenius relation, similar to diffusion coefficient in solid-state materials and phenomena, where the crystallite-size (d) typically depend on temperature as (77):

$$d = d_{\circ} \exp(-\Delta E/k_B T) \qquad (16)$$

where ΔE is the activation energy, kB is the Boltzmann constant, T is the absolute temperature, and d0 is a preexponential factor that depends on the physical properties of the substrate-oxide film configuration. If it is assumed that the crystallite-size relates directly to surface diffusion and atom rearrangement, it can be expected to witness the increase in d with annealing temperature in

accordance with the Arrhenius relation. As such, the d-values, determined from XRD, were fitted in Figure 14c, where it is evident that the experimental data fits to the first order exponential growth function. All the data fits to an exponential function (Figure 14c). This feature indicates the thermally activated mechanism as operative in the crystallization, which account for the changes in the Ga_2O_3 film's surface morphology and average crystallite size as a function of annealing temperature, as seen in the data from AFM and XRD measurements. Figure 14c displays the Arrhenius plots for the XRD data. The data are well fitted by a linear function. An activation energy of 0.12 (±0.01) eV for the nanocrystalline, monoclinic β-Ga_2O_3 was determined from the slope of the linear plot. Directly comparing this value with other reports is not currently possible as there is no available data for nanocrystalline Ga_2O_3 films, whether deposited by sputtering or other physical/chemical vapor deposition methods. This value (0.12 eV), while small, is to be expected for nanocrystalline films with the given size parameters, particularly when compared to the data of some other micro- and nanocrystalline metal-oxide thin films, such as monoclinic HfO_2 films and nanocrystalline, tetragonal WO_3 films (75,78).

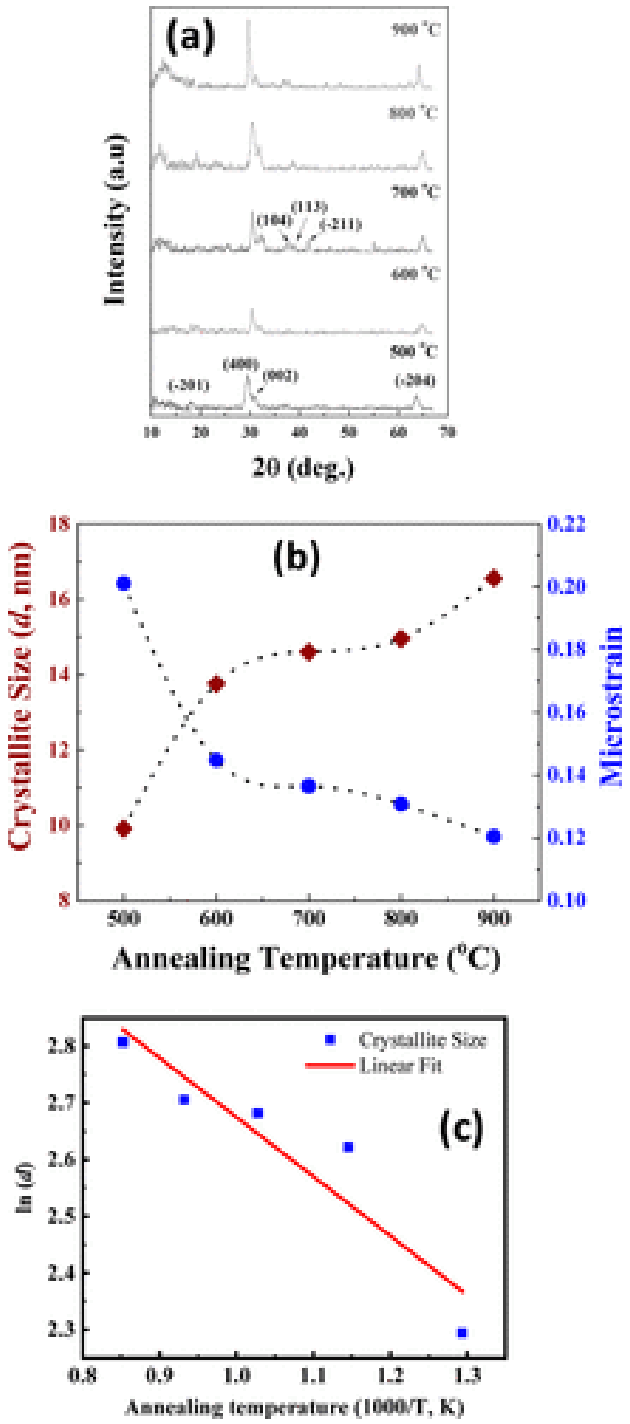

Figure 14: A) XRD patterns of as-deposited and annealed Ga_2O_3 films. B) Variation of crystallite size and microstrain in the Ga_2O_3 films. C) Arrhenius plot of crystallite size versus temperature.

5.1.3 Mechanical Properties

One of the key components of structure optimization for thin films lies with tailoring their mechanical properties (22,79). These properties, in turn, can be governed by various parameters, such as the coating-substrate hardness relation, film thickness, or roughness of the film, while the reactions are based largely on the rate of application and magnitude of stress (77,78). Large stresses may present in thin films that can lead to their deformations and cracking, and understanding and minimizing these stresses, how they occur, and in what ways they influence film integrity is vital in thin film production (80,81). A key component of determining overall wear resistance of thin films lies with elastic modulus and its relation to elastic strain to failure, which in turn is related to the hardness/elastic modulus (H/E) (81,82). These parameters were determined using the indentation load versus depth characteristics of as-deposited and annealed Ga_2O_3 films presented in Figure 15. Note that the mechanical properties of the films are strongly influenced by the underlying substrate material's properties (79). Therefore, penetration depth characteristics as a function of applied indentation load become critical to find the optimum load and proceed further with other measurements. As shown in Figure 15, the applied indentation load is varied from 100 to 2000 μN, while recording the corresponding penetration depth at each and every applied load. At the initial applied load of 100 μN, the penetration depth is 9 nm for the as-deposited Ga_2O_3 film. The penetration depth increases with increasing applied indentation load. For as-deposited Ga_2O_3 film, at the applied load of 350 μN, the total penetration depth is as high as reaches to 19 ± 1 nm, which nearly reaches 10% of total film thickness. Thus, this load has been considered to be optimum for testing all of the as-deposited and annealed Ga_2O_3 films for better comparison of nanomechanical properties. In general, to obtain reliable and true information on the films, the penetration depth must not exceed 10% of total film thickness (22,78). Thus, all samples readily

satisfy this requirement. However, while the indentation depth for the annealed Ga_2O_3 films at different temperatures is almost same, minimal differences (±5 nm) in penetration depth is due to variation in the structural quality of the respective films with steadily increasing annealing temperatures.

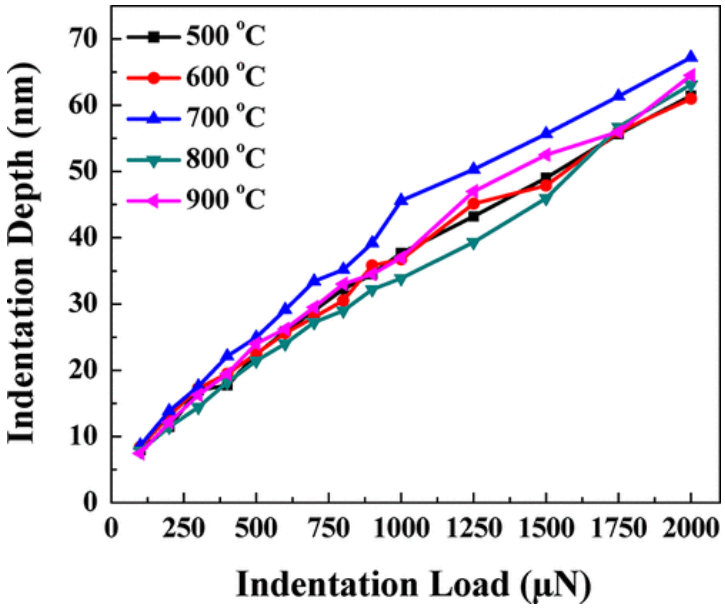

Figure 15: Applied indentation load versus indentation depth characteristics of Ga_2O_3 thin films. The data shown are for samples annealed under variable temperatures.

The loading and unloading curves for Ga_2O_3 thin films are shown in Figure 16a. The data is obtained with an indentation load of 350 μN. It can be noted that the load versus displacement curves are slightly different for Ga_2O_3 films annealed at different temperatures. Close inspection of the data indicates a slight shift with increasing annealing temperature, especially for Ga_2O_3 thin films annealed at 700−900 °C. These data enable us to determine the hardness (H) and elastic modulus (Er) of the Ga_2O_3 thin films. The variation of H and Er values with annealing temperature of Ga_2O_3 films are presented in Figure 16b and 16c, respectively. There was a noticeable difference in the H and Er values for the Ga_2O_3 films annealed at different temperatures. The observed

differences can be attributed mainly to the variation of crystallinity and morphology of Ga_2O_3 films as a function of annealing temperature. It can be noted (Figure 16c) that the H value of 27 GPa decreases initially for the Ga_2O_3 films annealed at 700 °C. This may be due to the residual stress relaxation by thermal annealing. However, it can be noted that further increase in annealing temperature to 800 °C increases the H values to ∼30 GPa, and the level remains more or less constant with further increase in the annealing temperature to 900 °C. The crystal structure improvement of Ga_2O_3 films with increasing annealing temperature accounts for the increased H values at >700 °C. Thus, the results indicated that the hardness of the annealed Ga_2O_3 films is predominantly due to the crystallization upon thermal annealing, as revealed by both XRD and AFM analyses.

In Figure 16c, the variation in Er of Ga_2O_3 thin films is shown as a function of annealing temperature. The trend is very similar to the H results shown in Figure 16b. The elastic modulus represents the resistance to small changes in separation of adjacent atoms in relation to interatomic bonding forces. The magnitude of the elastic modulus depends on the slope of the load−displacement curve. The Er values for the film deposited at 500 °C is ∼295 GPa, and with the annealing effect, Er values decreased to ∼265 GPa for the film annealed at 700 °C. On further temperature increasing, the Er values increased to ∼295 GPa for the films annealed at 800 and 900 °C. Overall, there was not a noticeable change in elastic modulus values.

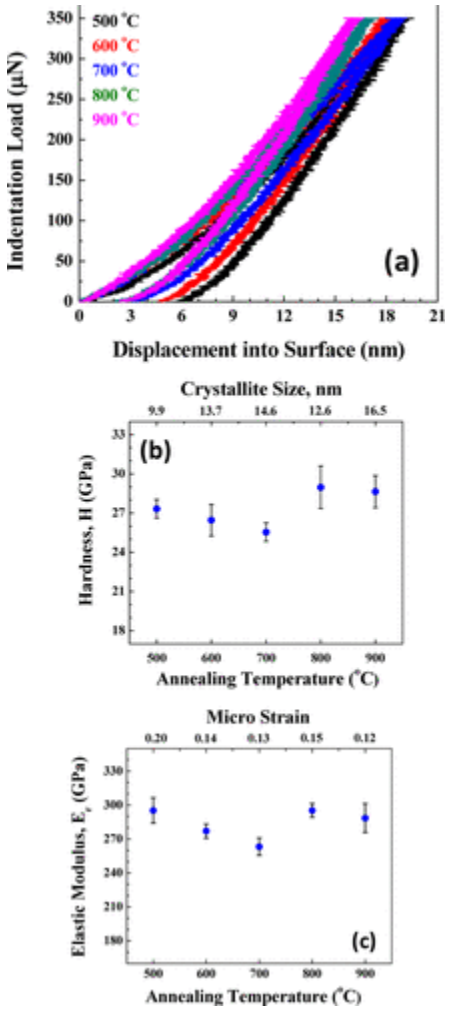

Figure 16: A) Load versus displacement curves obtained for Ga_2O_3 films. B) Hardness values of Ga_2O_3 films. C) Elastic modulus of Ga_2O_3 films.

The nanoscratch results of as-deposited and annealed Ga_2O_3 films are shown in Figure 17. In Figure 17a, the images of 20 μm × 20 μm are shown, as obtained before and after the scratch text of the Ga_2O_3 films, while the corresponding depth profiles are shown in Figure 17b. The Ga_2O_3 films exhibit no indication of delamination from the substrate. The nanoscratch testing was conducted in such a way that the only area immediately surrounding the scratch deforms, whereas the remaining part of the film is undamaged. The scratch test was conducted in ramping mode, in which normal force is increased with direction of tip travel. The depth profile characteristic for the

as-deposited Ga_2O_3 film is ~67 nm after the nanoscratch. On the other hand, for the film annealed at 900 °C, the depth is only about 53 nm. The data clearly indicate that there is no significant change in the early stages of annealing, while significant changes occur as discussed in XRD and nanomechanical sections. The main observation is that, while scratch tests revealed material pile-up, there was no evidence of delamination of the as-deposited and annealed Ga_2O_3 films.

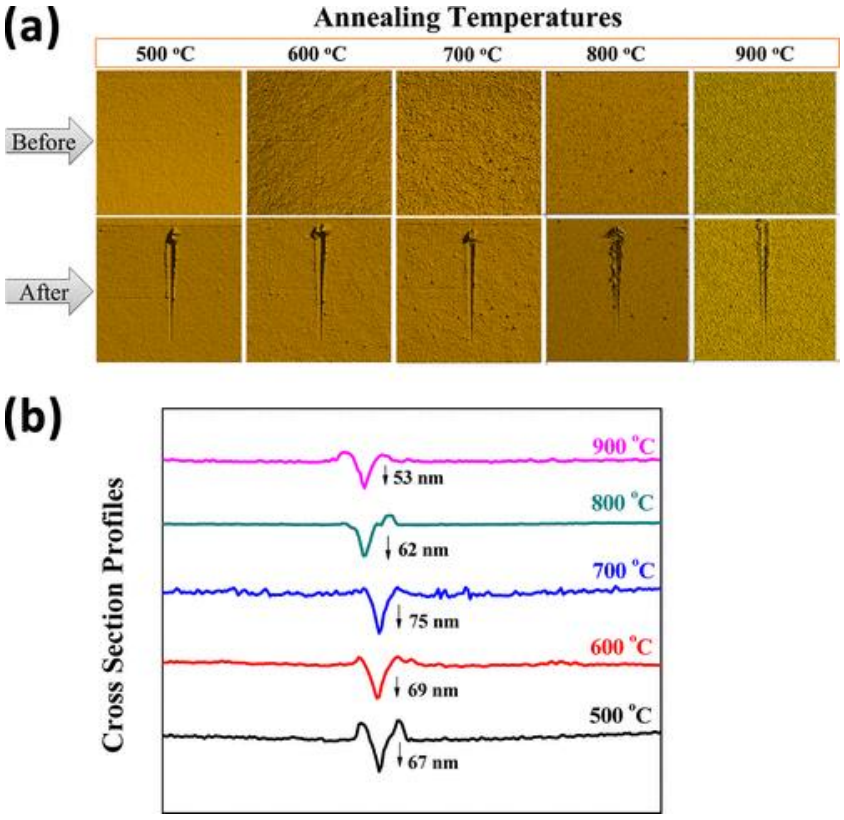

Figure 17: A) Scratch testing data of Ga_2O_3 thin films. The images represent before and after the scratch test performed on the samples. B) Scratch testing profiled of Ga_2O_3 thin films. The depth decreases with increasing annealing

5.1.4 Optical Constants and Electrical Resistivity

The spectroscopic ellipsometry measurements and analyses were employed to determine the optical constants of the Ga_2O_3 films. The refractive index (n) and extinction coefficient (k) were fitted with Cauchy dispersion model which is quite successful in evaluating the optical properties of Ga_2O_3 films made by several deposition methods (83-85). This model was chosen partly due to transparency in respective wavelength regions for Ga_2O_3 films and partly due to it providing a successful fit to the data and serving to explain the optical properties of the films (21,40). The Cauchy equation for refractive index n as a function of wavelength λ is

$$n(\lambda) = A + B/\lambda^2 + C/\lambda^4 \quad (17)$$

where A, B, and C are the Cauchy coefficients that are unique to a given material. The three constants play dominant roles n(λ) along different wavelengths with A for long wavelengths, B for wavelengths in the middle of the visible spectrum, and C for shorter wavelengths. However, extracting meaningful physical information from ellipsometry requires forming an optical model of the sample, accounting for several distinct layers with varying optical dispersions (84,85). The layer interfaces act as optical boundaries where light is refracted and reflected per the Fresnel relations. Figure 18 shows the stack model used to determine the optical constants of the Ga_2O_3 films. From the top down the model contains: Ga_2O_3 film, Ga_2O_3/SiO2/Si interface and Si substrate. To accurately fit the data both surface and interface roughness were also considered.

Figure 19 shows the spectral dependencies of ellipsometric parameters Ψ (azimuth) and Δ (phase change); these parameters are fitted using appropriate models to determine film thickness and the optical constants, refractive index (n) and extinction coefficient (k). These determinations are derived from the best fit between experimental and simulated spectra. The curves obtained for

annealed Ga_2O_3 films indicate, as shown in Figure 19, agreement between the experimental and simulated data for the entire annealing temperature range.

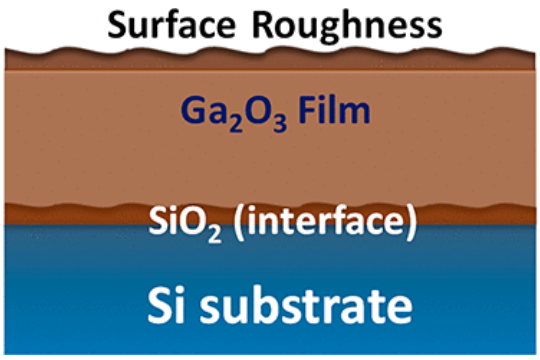

Figure 18: Stack model of the Gallium oxide sample constructed for ellipsometry data analysis

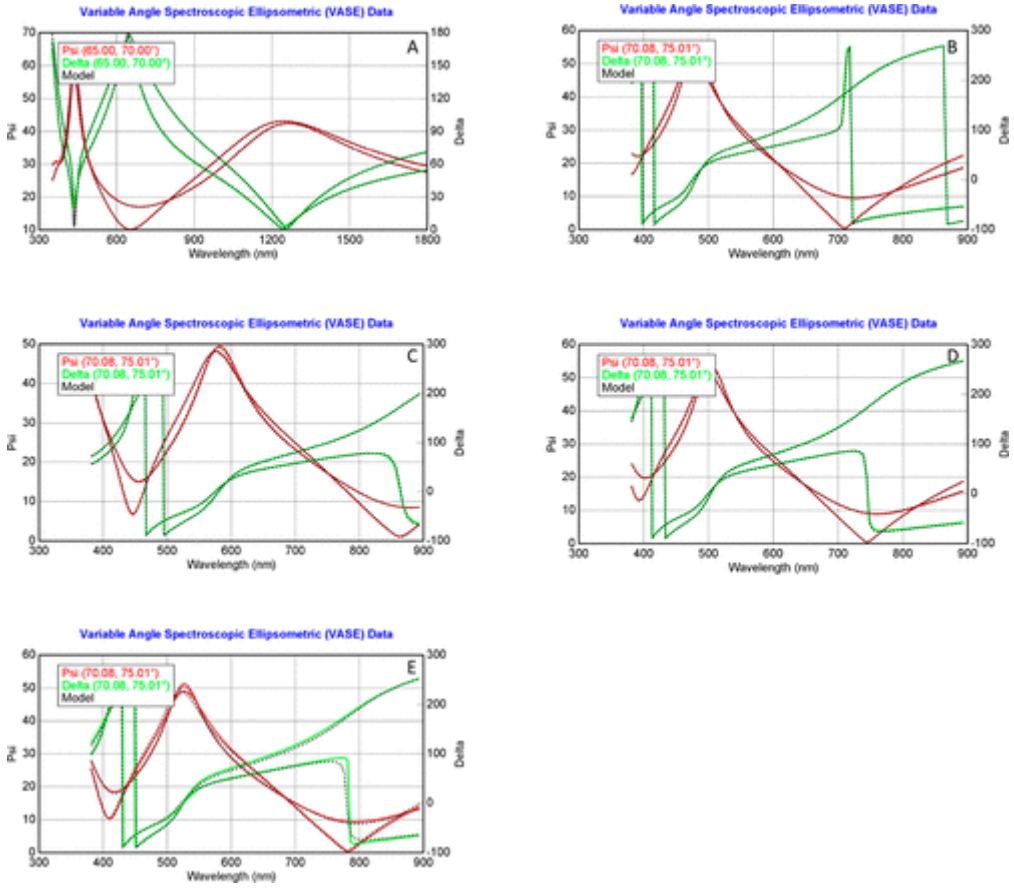

Figure 19: Experimental and modeled curves of Ψ and Δ for gallium oxide films: A) 500, B) 600, C) 700, D) 800, and E) 900 °C.

The dispersion refractive index profiles determined from SE data for Ga_2O_3 films are shown in Figure 20. There is a sharp increase of fundamental absorption of energy across the band gap correlating to shorter wavelengths. The thermal-annealing induced changes in structure and the dependence on annealing temperature are clear in the dispersion curves (Figure 20). The data reveals that there is a progressive increase in n values with increasing annealing temperature. Throughout the spectrum the extinction coefficient values are low and very close to zero. An understanding of the structural quality of Ga_2O_3 films can also be derived from the dispersion profiles of n(λ). Specifically, the curves (Figure 20) indicate the increasing tendency of n value of the Ga_2O_3 films which is due to improved crystallinity of the samples. However, we believe that the changes in optical properties and electrical properties are primarily due to changes in the physical characteristics and crystallization but not at all due to any chemical changes (86). For instance, the spectroscopic analyses on these Ga_2O_3 films as function annealing temperature indicate that the chemical stoichiometry is well maintained in the entire range of Ta. As reported elsewhere, (Ga3+), the highest chemical oxidation state for gallium, exists in both the as-deposited and annealed Ga_2O_3 films (86). The electronic structure was not observed to have changed significantly, particularly when considering the chemical valence of Ga ions and Ga−O bonds as a function of the thermal annealing (86). Therefore, the observed trend in optical and electrical properties of in this work attributed to the crystallization and improved packing density of the Ga_2O_3 films upon thermal annealing.

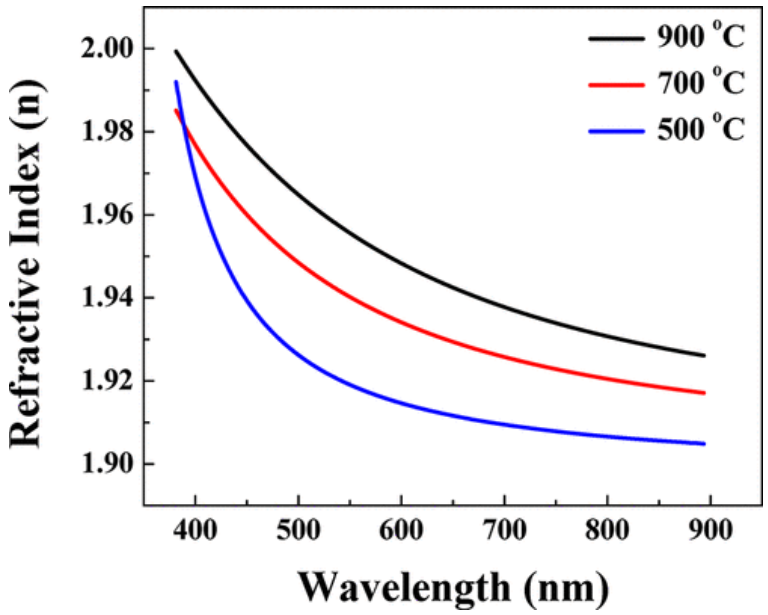

Figure 20: Refractive index profiles of Ga_2O_3 films.

The electrical properties of Ga_2O_3 films as a function of annealing temperature corroborated with the changes in structure and morphology. The Ga_2O_3 thin films deposited at 500 °C had electrical resistivity of 104 × 103 Ω cm, and it slightly increased to 127 × 103 Ω cm for the Ga_2O_3 films annealed at 600 °C. Then it starts decreasing to 85 × 103 Ω cm and significantly down to 1.04 × 102 Ω cm for the Ga_2O_3 films annealed at 800 and 900 °C, respectively. The effect of annealing on the microstructure evident in the electrical resistivity of the Ga_2O_3 films. The electrical resistivity usually becomes higher with grain size reduction usually leads to an increase in electrical resistivity due to the increasing grain boundary volume and associated charge carrier flow impedance (40,68). Grain boundary scattering becomes a dominant effect leading to higher electrical resistivity as a result of crystallite size becoming smaller than the electron mean free path. Lattice imperfections such as vacancies and dislocations, often present in nanocrystalline materials, also strongly influence electrical resistivity (40,68). Additionally, lattice strain and associated distortions can negatively affect the charge mobility leading to a decrease in

conductivity. The room temperature electrical resistivity variations with annealing temperature observed for Ga_2O_3 films can be explained taking these factors into consideration. The resistivity decrease by increasing annealing temperature can be attributed to increased crystallinity of the films, as well as a combined effect of the average crystallite size increase and surface morphology variation. This trend in resistivity can then be directly attributed to better crystallinity, larger grains, and fewer grain boundaries in the samples annealed at higher temperatures.

5.2. PLD Gallium Oxide Films

5.2.1 Crystal Structure

The crystal structure, phase stabilization and strain (if any), and morphology data of the PLD Ga_2O_3 films are presented in Figure 21. The XRD data of PLD Ga_2O_3 films (Figure 21a) indicate the information on the crystal structure and phase. The sequence of structural transformations induced as a function of the deposition temperature (Ts) can also be noted. It is evident that XRD peaks with appreciable intensity can be seen only in the Ga_2O_3 samples deposited at Ts ≥ 600 °C. On the other hand, Ga_2O_3 films deposited at Ts < 600 °C are all amorphous, as is evident from the diffuse nature of the XRD patterns. An amorphous-to-crystalline structural transformation can be noted in Ga_2O_3 films when Ts is 600 °C. The Ga_2O_3 films deposited at Ts = 600−700 °C correspond to a monoclinic crystal structure, which has been identified to be β-Ga_2O_3 existing in the C2/m space group. However, both of them show the presence of slightly varying lattice parameters and strain profiles. The average crystallite size calculated using the Scherrer equation is ~9 nm, which is more or less the same for Ga_2O_3 films deposited at Ts = 600−700 °C.

The XRD results also indicate that the PLD nanocrystalline β-Ga_2O_3 samples exhibit the preferred orientation. The films deposited on Si(100) substrates clearly show textured growth,

which is seen in the detailed quantitative analysis (Figure 21b). While the three diffraction planes with the appreciable intensity identified are $(2\bar{0}1)$, $(\bar{4}01)$, and $(\bar{7}12)$ (Figure 2c), the PLD Ga_2O_3 films exhibit $(\bar{4}01)$ texturing. The degree of texturing can be understood from the texture coefficient (Figure 21b), which is relatively higher for β-Ga_2O_3 films deposited at 600−700 °C. The kinetics and thermodynamic processes involved in finding the most stable texture development are related to the contributing effects of the atomic influx and the minimum energy for that particular synthesis condition. Increasing Ts provides the additional kinetic energy, leading to the growth of more random crystals. A similar temperature-dependent trend was observed earlier, where after a certain critical substrate temperature it showed a drastic phase transition from amorphous-to-nanocrystalline material formation.

Parts d and e of Figure 21 show the morphology fingerprints of amorphous and nanocrystalline PLD Ga_2O_3 films, respectively. The nanocrystalline Ga_2O_3 films exhibit higher root-mean-square (RMS) roughness compared to those amorphous films. Also, for nanocrystalline PLD Ga_2O_3 films, the Gaussian-type grain-size distribution characteristics prevail, whereas the other samples exhibit almost a flat surface without any signature of cluster formation. These results corroborate with XRD analyses in distinguishing the crystalline versus amorphous PLD Ga_2O_3 films. The increased RMS roughness values can be due to the self-assembled conical nanotextures, with dimensions of 10−20 nm, on the front surface. Such morphological features promote the algorithm of multiple reflection and absorption, which results into better photon absorption (86).

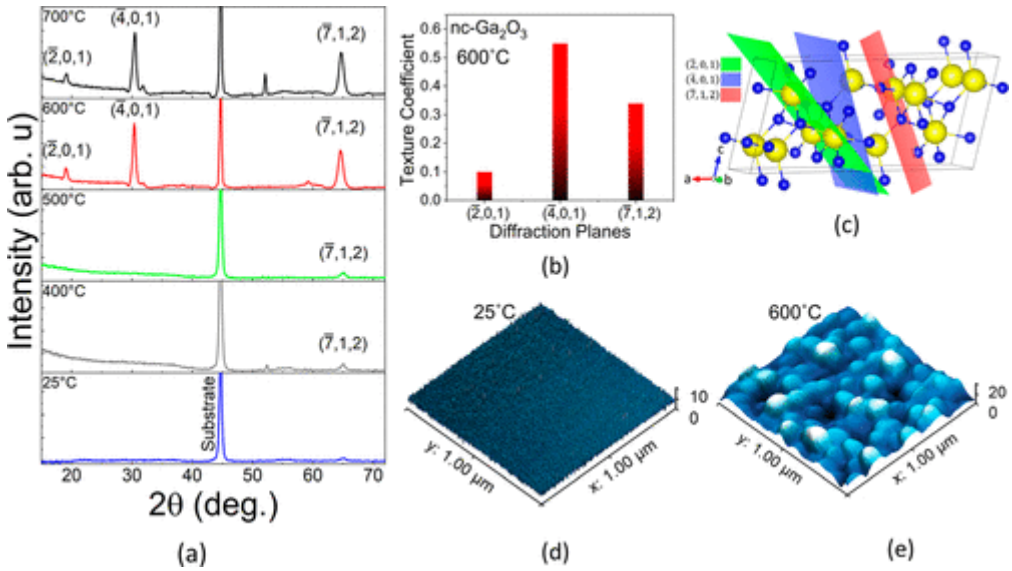

Figure 21: A) θ/2θ XRD of as-grown gallium oxide thin films with increasing in situ substrate temperature, showing the evolution of amorphous gallium oxide into nanocrystalline β-Ga_2O_3. The peaks noted are ($2\bar{0}1$), ($4\bar{0}1$), and ($\bar{7}12$). B) Texture coefficient of the corresponding diffraction planes, deposited at higher substrate temperature, where ($4\bar{0}1$) shows the highest among all of them. C) Schematic of a monoclinic β-Ga_2O_3 unit cell, with the three diffraction planes contributing to the observed XRD peaks. D) 1 × 1 μm^2 surface morphology of amorphous Ga_2O_3 and E) highly oriented nanocrystalline β-Ga_2O_3 film.

5.2.2 Nanostructure Interface

The structural quality and interface nanostructure of Ga_2O_3 films further evidenced in TEM analyses are presented in Figure 22. The data shown are the representative survey and high-resolution TEM (HRTEM) images and SAED patterns from the specifically selected regions of the Ga_2O_3 film−Si substrate. Additionally, the fast Fourier transfer spectra are also shown as insets in the corners of the relevant HRTEM images. High-quality interface structures are manifested for all of the PLD Ga_2O_3 films, which were found to be uniform with sharp surfaces. No significant diffusion of Ga_2O_3 into the substrate interface was observed. Corroborating with the XRD results,

the HRTEM and SAED analyses further confirm the formation of amorphous and nanocrystalline Ga_2O_3 films depending on Ts. Apparently, fabrication at elevated substrate temperature (600−700 °C) accelerates the nucleation and growth of βGa_2O_3. Preferential texturing along $(\bar{4}01)$ was confirmed by both XRD (Figure 21) and SAED (Figure 22), while structural characterization clearly indicated the formation of more compact, dense β-Ga_2O_3 with a smooth interface structure.

It is very clear from the cross-sectional morphology that, with increasing temperature, there is a clear reduction of the film thickness. The higher out-diffusion rate of impinged adatoms with increasing substrate temperature explains the lower film thickness with higher Ts. There is no evidence of Ga atom back-etching of the Si substrate or interdiffusion through the interfacial layer. So, the density of the initial nucleation centers is free from any additional factors other than incoming adatoms, substrate temperature, and oxygen pressure. The chemical analyses (not shown) made using XPS indicate that, in all of the samples deposited under variable temperature, the Ga ions exist in their highest oxidation state (Ga3+). The chemical stoichiometry is well maintained, with a O/Ga ratio close to the expected value (∼1.5) in all of the samples.

The β-Ga_2O_3 film on the Si substrate is typically opaque in the UV-to-visible region; therefore, we relied on optical reflectivity measurements for further analysis, especially to determine the band gap. To calculate the band gap of the Ga_2O_3 films, we adopted an indirect approach, which was quite successful in semiconductors. The optical data of PLD Ga_2O_3 films are shown in Figure 23. The room temperature diffuse reflectance (R) of as-deposited PLD Ga_2O_3 films (Figure 23a) was analyzed with the help of the Kubelka−Munk function, which is defined as

$$F(R) = \frac{K}{S} = \frac{(1-R)^2}{2R} \tag{18}$$

Here, F(R) represents the Kubelka−Munk function, which replicates patterns similar to those of wavelength-dependent absorbance of the thin film, and K, S, and R are the absorption coefficient, scattering coefficient, and reflectance, respectively. Figure 23b represents the corresponding wavelength-dependent F(R) plots for each sample. Additionally, a modified Tauc equation has been implemented to calculate the band gap of nanocolumnar β-Ga_2O_3 films.

$$\alpha h\nu = A(h\nu - E_g)^n \tag{19}$$

$$F(R)\, h\nu = A(h\nu - E_g)^n \tag{20}$$

Here, α, h, ν, Eg, F(R), and A represent the absorption coefficient, Planck's constant, incident photon frequency, optical band gap, Kubelka−Munk function, and fitting constant, respectively. We used n = 1 /2 for calculating the allowed direct transition energy in the electronic band structure (Figure 23c). From the high end (600 °C) to low end (25 °C) of Ts, the band-edge absorption shows a direct shift (Figure 23c). In addition, the increment in the interference fringes (Figure 23a,b) also shows an inverse correlation with Ts. A higher number of interference fringes, especially for samples deposited at lower Ts, infers a higher film thickness, which is further confirmed by the TEM data and analyses. The optical band gap of nanocrystalline PLD Ga_2O_3 films (Figure 23d) is almost similar to that reported for Ga_2O_3; however, the bandgap values were low for amorphous PLD Ga_2O_3 films. This observation refers to the formation of very high quality nanocrystalline PLD Ga_2O_3 films. The presence of a higher defect density, random orientation of unit cells, interstitial states, surface states, cumulative strain, etc., in amorphous samples deviates the band-to-band transition from its ideal value, whereas a high-quality nanocrystalline Ga_2O_3 film with reduced parasitic components leans toward its ideal optical behaviors (39).

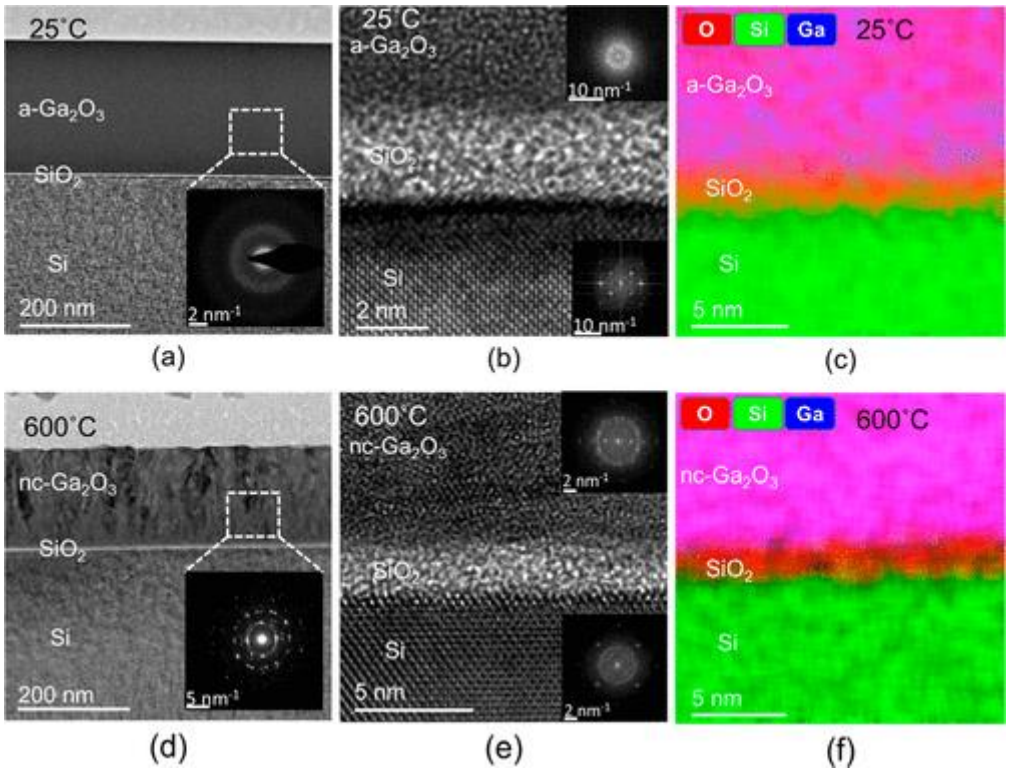

Figure 22: Cross-sectional TEM imaging analyses of Ga_2O_3 films. The TEM images of amorphous Ga_2O_3 A–C) and nanocrystalline Ga_2O_3 D–F) films are shown along with the corresponding elemental color mapping. In situ diffraction patterns provide evidence for the amorphous and nanocrystalline nature of the samples. For nanocrystalline Ga_2O_3, the TEM data (imageD) shows close-compact nanocolumnar growth after the thin β-Ga_2O_3 seed layer.

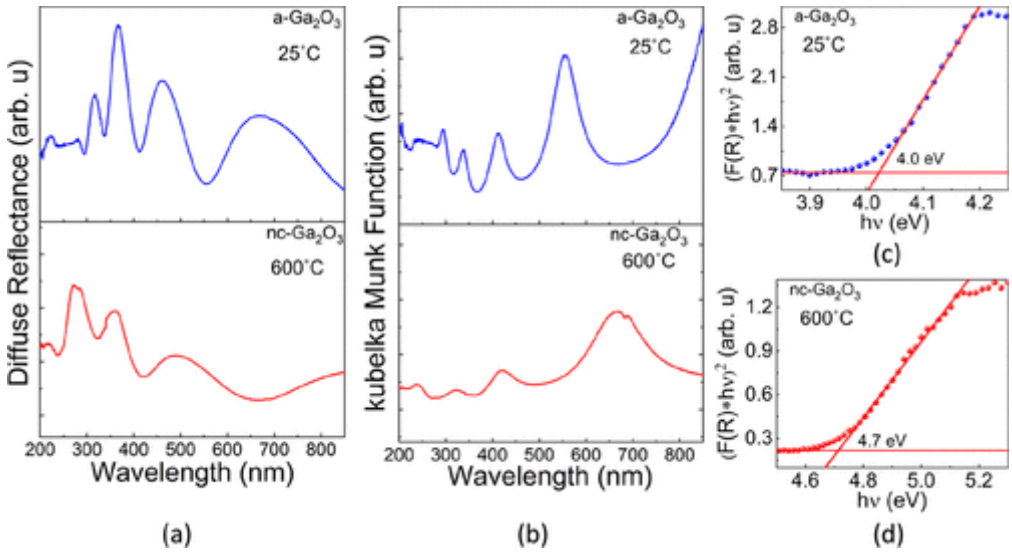

Figure 23: Optical property analyses of amorphous and nanocrystalline Ga_2O_3 films. A) Diffuse-reflectance spectra obtained for Ga_2O_3 samples at a perpendicular photon incident mode. Assertively, amorphous Ga_2O_3 shows higher interference fringes than nanocrystalline Ga_2O_3 films. B) Kubelka–Munk function of the corresponding amorphous and nanocrystalline Ga_2O_3 films. The Kubelka–Munk function derived from the reflectance data clearly indicates significant differences in the respective Ga_2O_3 thin-film samples. C - D) Tauc plots of amorphous and nanocrystalline Ga_2O_3 films. The band-edge absorption difference can be noted if amorphous Ga_2O_3 is compared to nanocrystalline Ga_2O_3.

5.2.3 Photoluminescence (PL)

The PL spectra of amorphous and nanocrystalline PLD Ga_2O_3 films are presented in Figure 24a and 24c, respectively. The data are shown in association with the corresponding carrier dynamics of photogenerated carriers (Figure 24b,d), respectively. It is clear that all of the possible luminescence transitions are from the donor−acceptor pair, which is strongly supported by the findings of many researchers (37-39). These are Ga- and O-related states. Although we try to excite all of the samples with near-band-gap photons, there is no such signature of band-to-band transition

in these samples. The room temperature deposited PLD Ga_2O_3 films do not show any luminescence signal because most of the excited carriers are being trapped. Additionally, there is an overall blue shift of the PL peak with a significant increment of the absolute intensity. Sufficient surface energy and oxygen over pressure, during deposition, promote the samples with higher substrate temperature to form a close-compact nanocolumnar β-Ga_2O_3 thin film. The overall dimensions of the Ga_2O_3 nanocrystals are much higher than the corresponding Bohr radii and do not have any quantum confinement effect. However, these donor− acceptor pairs are acting as a band of energy states between the valence and conduction bands and can be tuned depending on a few selective deposition parameters, like the substrate temperature, oxygen overpressure, and laser pulse frequency. Also, a phonon is acting as a core member of this downward carrier transition, resulting in a higher photogenerated carrier lifetime. The overall carrier dynamics of both amorphous and nanocrystalline Ga_2O_3 thin films is demonstrated through Figure 5b,d, where horizontal arrows represent photon incidence or photon extraction, vertical arrows represent the generation and recombination of an electron−hole pair, diagonal arrows represent phonon-assisted relaxation of photogenerated carriers, and finally vertical downward arrows (color: dark gray) represent the trapping of carriers. The line thickness of each arrow carries the signature of the corresponding process. The a-Ga_2O_3 thin film suffers from a significant number of crystalline defects and is more prone to optical defect formation, which is further affected with surface states. Assertively, the trapping of carriers is dominating the direct carrier recombination through sub-bands. Thus, it shows a very low luminescence intensity (the gray arrow is thick, while others are very thin, except the photon-incident- and photogeneration-related signatures). As we optimize the growth process to obtain a nanocrystalline Ga_2O_3 thin film, decorated with nanocolumnar crystal formation in addition to conical surface morphology, the film becomes more immune to the defect formation.

As a result, it shows a much higher percentage of direct recombination of photogenerated carriers, with little carrier trapping. Figure 24d supports the same.

The mechanistic aspects and underlying science behind the observed green emission and wide-range spectral selectivity in intrinsic, nanocrystalline β-Ga_2O_3 films can be explained as follows. We believe that the selectively and precisely engineered nanocrystalline Ga_2O_3 with control over the size, phase, and interface nanostructure is the key aspect that promotes the enhanced PL activity in these samples. As revealed by the AFM studies, self-assembled conical nanotextures with uniform distribution characteristics and roughness on the front surface promote the algorithm of multiple reflection and absorption, which promotes enhanced photon absorption. Deriving such an enhanced property and performance in this work is facilitated by direct control over the growth process. The physical and/or thermodynamic parameters that control the growth and evolution of PLD β-Ga_2O_3 films on Si are the substrate temperature, chamber pressure, laser wavelength, laser power, laser pulse frequency, and distance between the substrate and target source. All of the β-Ga_2O_3 thin-film samples deposited at Ts < 600 °C are all amorphous in nature, which is certainly expected because Ts is lower than the critical temperature for crystallization of Ga_2O_3. At and beyond 600 °C, it shows a particular β-Ga_2O_3 phase with a close-compact nanocolumnar thin film, decorated with nanocrystalline surface morphology. The growth dynamics here are reminiscent of the Structure-Zone Model (SZM)28 but in a slightly modified way. The original theory was developed on the basis of sputter deposition of different metallic thin films with varying substrate temperature and chamber pressure, whereas here we have deposited complex metal oxide through PLD. The pulsed-laser-generated plume creates a higher order of the localized supersaturating regime on the substrate, and ∼50 mTorr oxygen background pressure drastically reduces the surface adatom mobility, resulting in a very high density of the nucleation

centers, compared to the standard sputter deposited β-Ga_2O_3. Thus, the growth mode of β-Ga_2O_3 films clearly falls into the high-pressure zone-T region in SZM. Therefore, undoubtedly, the compact nanocolumnar β-Ga_2O_3 film, as reflected in the cross-sectional TEM studies, can be due to the growth dynamics.

Additionally, anisotropic thermal conductivity plays a significant role during the growth process (13,88). The high-temperature (600−700 °C) PLD-assisted formation of a β-Ga_2O_3 nanocrystalline thin film on Si has been organized in two consecutive stages: initial random crystallization of β-Ga_2O_3 on amorphous SiO2, followed by thermally driven preferred surface diffusion and crystallization of a nanocolumnar (Figure 24e) structure (Figure 24f, showing the schematic). Luo et al. have already shown differential thermal conductivity toward different orientations of β-Ga_2O_3 crystals. Correlating that observation with the current growth process, we can infer that the first step is almost random, resulting in nano crystallization with all possible orientations. Then, at the beginning of the second stage, higher thermally conductive zones promote better kinetic energy to the incoming adatoms, whereas the others appear to be relatively dull for providing sufficient energy. As a result, the incoming adatoms tend to settle down at those lower-energy spots, forming compact vertical nanocolumns. This is similar to the GLAD process but without any external shadowing effect. Assertively, it shows close-compact nanocolumnar growth with a higher fill factor (87,89). Thus, the observed enhanced green-emission PL characteristics in the intrinsic nanocrystalline Ga_2O_3 films without the need for any dopants are attributed to precise engineering with control over the size, phase, and interface nanostructure, where the self-assembled conical nanotextures promote the algorithm of multiple reflection and absorption, leading to such optoelectronic properties.

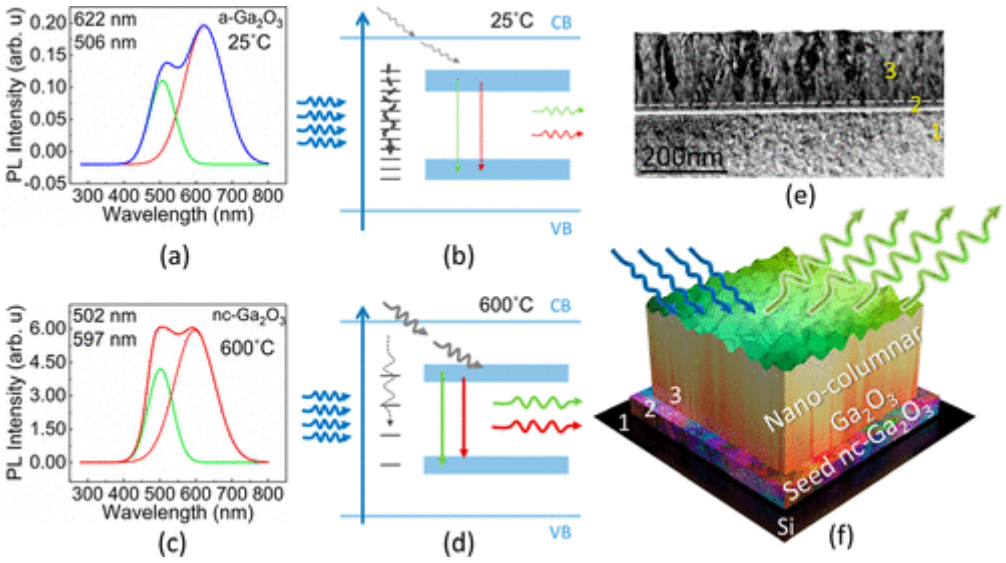

Figure 24: Room temperature PL spectra of amorphous A) and nanocrystalline C) Ga_2O_3 films. B and D) Corresponding transitions of photoexcited electrons. Evidently, there is a giant jump in the photoextraction efficiency, with a moderate blue shift between the donor–acceptor energy states. E) Cross-sectional transmission electron microscope image of close-compact nanocolumnar β-Ga_2O_3 thin film, showing three stages of the growth process, Si substrate 1, nanocrystalline seed layer 2, nanocolumnar β-Ga_2O_3 3. F) Schematic of a close-compact nanocolumnar β-Ga_2O_3 on top of a randomly oriented seed β-Ga_2O_3 layer on the Si substrate, facilitating green emission.

5.3. Gallium Oxide Nanofibers

5.3.1 Solution Characterization, Fiber Formation, and Microstructure

Solution parameters most often considered for the electrospinning process include viscosity, surface tension, and electrical conductivity. These parameters, measured as a function of gallium nitrate concentration variations used in this study, are shown in Figure 25. The apparent viscosity was found to increase with gallium nitrate. The formulation methodology is at least partially responsible for the viscosity increase because the polyvinylpyrrolidone concentration is

also being increased as the gallium nitrate concentration increases and increasing polymer concentration in solution is well-known to increase viscosity. However, it is also possible that increasing gallium nitrate concentration also contributes to the viscosity increase through chelation between gallium ions and the carbonyl-nitrogen resonance structure in polyvinylpyrrolidone (90-92). The surface tension was not significantly affected by the gallium nitrate concentration. The one exception was with 15 wt.% gallium nitrate, but this was most likely due to the high viscosity of the solution interfering with the measurement. The general surface tension constancy suggests that it is most likely being controlled by the water:ethanol solvent, which was held constant. The surface tensions of the feedstock solutions are intermediate between the surface tensions of water (72 dynes/cm) and ethanol (22 dynes/cm) and the mean surface tension value of 33 dynes/cm for a 50:50 wt.% water:ethanol mixture is consistent with expectations (92,93). The electrical conductivities of the feedstock solutions increase linearly with gallium nitrate concentration, which is also expected based on the electrical conductivity dependence on charge carrier concentration.

Initial fiber spinning of a solution containing 15 wt% of the gallium nitrate precursor led to erratic fiber formation and minimal fiber deposition on the rotating drum collector. This can most likely be attributed to either the high viscosity or the high electrical conductivity of this solution (see Figure 25). Poor fiber quality and microstructure has been observed when viscosity is above 1000 cP, but did not generally prevent deposition so the high electrical conductivity is expected to be the major contributing factor (94). Electrospun fibers can remain electrically charged after the spinning process and repulsion between fibers can be responsible for inhibiting fiber deposition (95,96). The initial electrospinning result suggests a gallium nitrate concentration

of 15 wt% is too high for effective fiber collection. Reducing the gallium nitrate concentration below 9 wt.% lead to successful fiber formation and collection.

Initial assumptions used in formulating the electrospinning solutions included: 1) viscosity is primarily controlled by the polymer concentration, 2) as-spun fiber diameter is primarily controlled by viscosity and so controlled by polymer concentration, and 3) the ceramic fiber diameter after heat treatment is primarily controlled by a combination of the initial fiber diameter and the ceramic precursor concentration. It was believed that if these assumptions were reasonable, then electrospinning the feedstock solutions using similar parameters would result in similar as-spun fiber diameters and the ceramic fiber diameters will depend on the gallium nitrate concentration. SEM images shown in Figure 26 demonstrate the fiber morphology of the as-spun fibers and of the Ga_2O_3 fibers after a heat treatment at 700ºC. The average fiber diameter of as-spun fibers with 3.25 wt.% gallium nitrate was 118 ± 8 nm based on a 95% confidence interval from 40 measurements. This average fiber diameter is a statistically insignificant from the average fiber diameter of 126 ± 7 nm for the as-spun fibers with 7.50 wt.% gallium nitrate based on analysis of variance ($p = 0.15$). In contrast, the difference between the two average fiber diameters of the Ga_2O_3 fibers from the as-spun fibers were statistically significant ($p = 10^{-7}$), corresponding to 62 ± 5 nm for the fibers originally containing 3.25% wt.% gallium nitrate and 83 ± 5 nm for the fibers originally containing 7.50 wt.% gallium nitrate. The similar fiber diameters in the as-spun state and different fiber diameters in the heat-treated state confirm our initial assumptions are reasonable over the concentration range of 3.25-7.50% gallium nitrate.

The Ga_2O_3 nanofibers in Figure 26(d) have protrusions on the surfaces of the nanofibers. These protrusions are like prior observations by Zhou *et. al.* when heat treating fibers at 600ºC (96), whereas smooth fibers were obtained when heat treating at either 550ºC, corresponding to

fully amorphous fibers, or 750ºC and corresponding to fully crystalline fibers. Zhou proposed that this fiber morphology results from the onset of crystallization, whereby the protrusions are crystalline β-Ga_2O_3 growing on the amorphous fibers. The heat treatment at 700ºC is intermediate between the 600ºC and 750ºC temperatures used by Zhou and is therefore consistent. However, an interesting feature of Figure 26 is that the fibers originally containing 3.25% gallium nitrate and heat treated at 700ºC did not exhibit the same morphological features. This suggests different crystallization behavior when using different gallium nitrate concentrations.

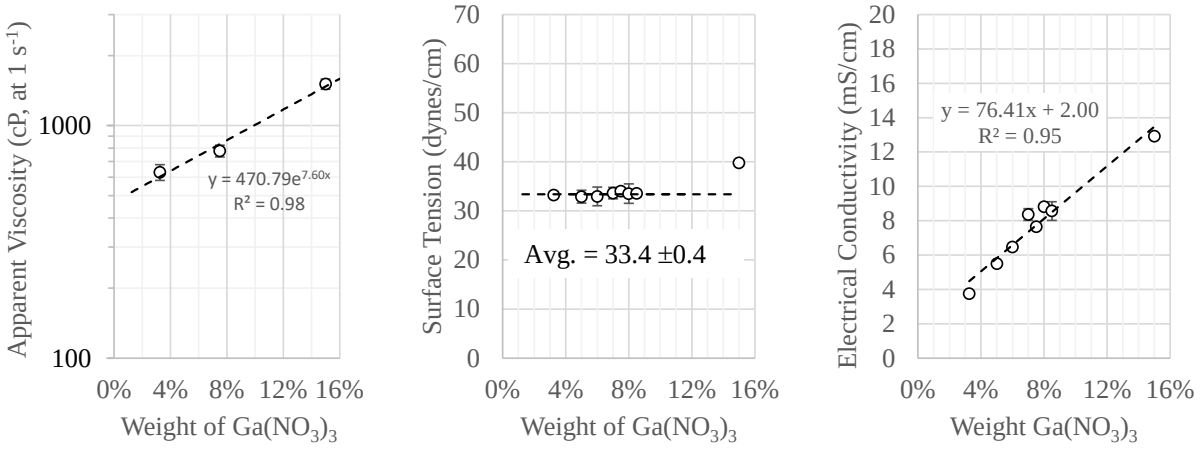

Figure 25: Apparent viscosity, surface tension, and electrical conductivity of electrospinning feedstock solutions as a function of Ga(NO3)3 concentration. Errors bars on data points represent a 95% confidence interval from three measurements.

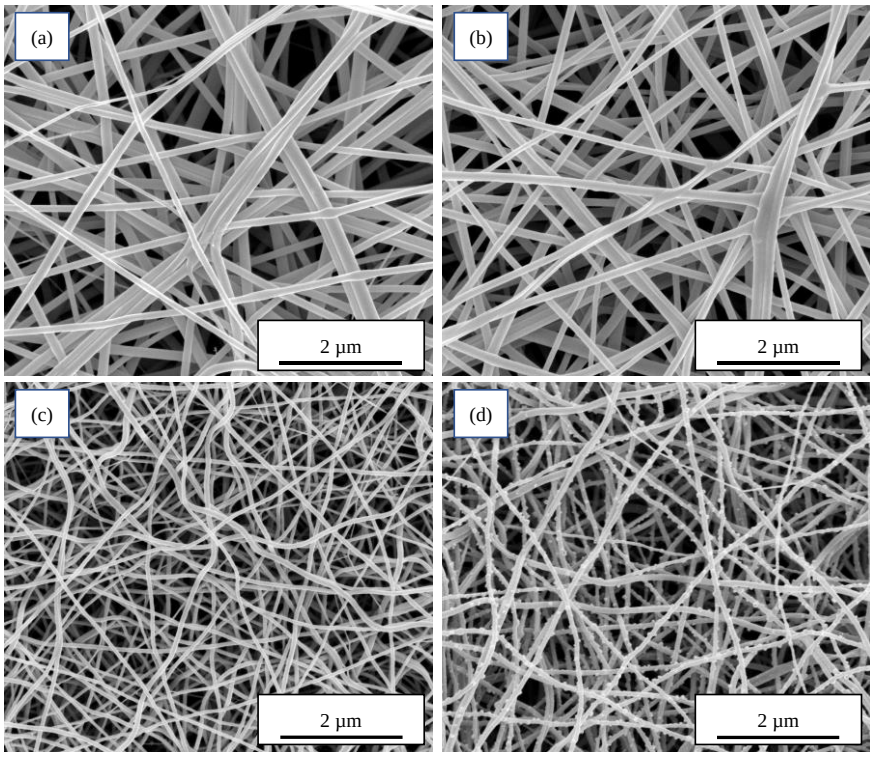

Figure 26: Secondary electron images of as spun fibers with A) 3.25 wt.% gallium nitrate and B) 7.50 wt.% gallium nitrate. The fibers with C) 3.25 wt.% gallium nitrate and D) 7.50 wt.% gallium nitrate after a thermal treatment at 700ºC are also shown.

5.3.2 Thermal Stability Behavior

Thermogravimetric analysis and data obtained on the Ga-oxide nanofiber samples are shown in Figure 27. It is evident that TGA curves show an expected decrease in mass, which is associated with the decomposition of polymers within the fibers. Such a result would be expected with conversion of the gallium nitrate precursor and polymer to amorphous gallium oxide and then to crystalline gallium oxide.

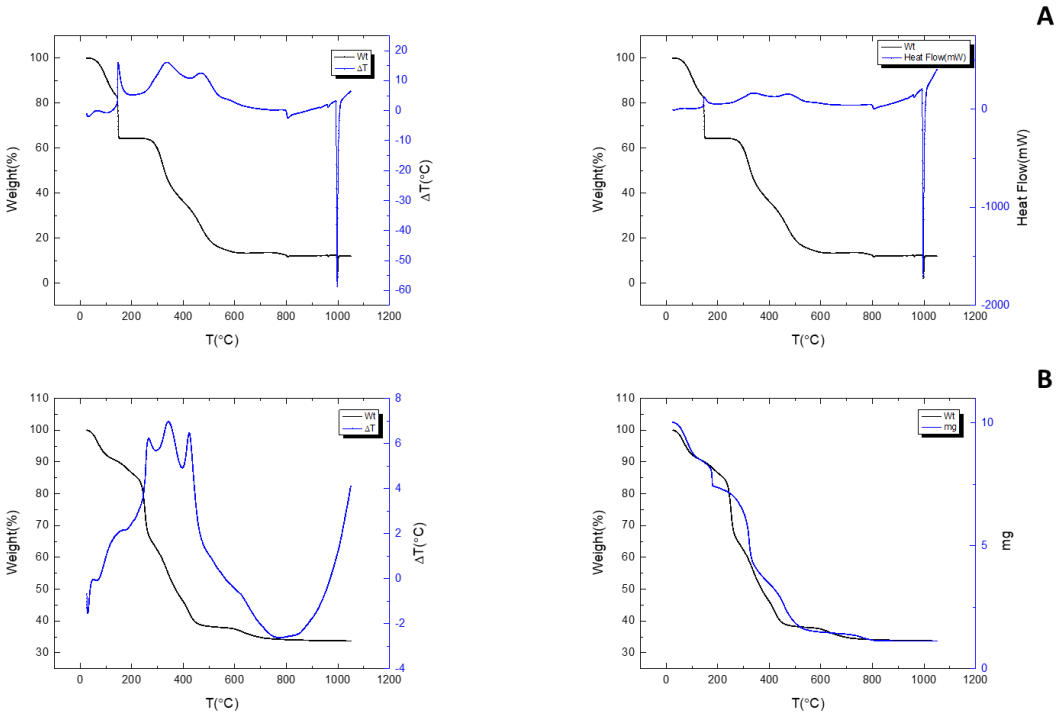

Figure 27: Thermogravimetric analysis of nanofibers. The data recorded in the temperature range of 25-1050 ºC shown.

5.3.3 Crystal Structure, Phase Stabilization and Chemical Bonding

The XRD patterns of pre-heat treated as well as post-processing annealed samples indicated the phase evolution in these nanofibers. However, the TEM data are more relevant to discuss the phase. The data shown are for pre-heat treated samples and samples annealed at 700 °C, 800 °C, and 900 °C, respectively. Both α and β phases of gallium oxide are present at 700 °C which can be considered reasonable given the transitional nature of the samples from amorphous to crystalline. However, there was indication of the alpha phase present at 800 °C, albeit, only in trace quantities. This is unexpected as gallium oxide morphology is typically expected to shift entirely to β phase when subjected to 800 °C temperatures when converted in thin films (98). This combined α and β phase pattern can also be seen in Raman spectroscopy data for the 800 °C

samples. There were technical issues in preparing the 700 °C samples for the Raman measurements so they were not included.

Finally, to better understand the structure evolution in Ga-oxide nanofibers, the local microstructure of the selected samples is probed using TEM measurements. Figure 29 presents HAADF-STEM (Figure 29A and B) and BF TEM (Figure 29C D) images of Ga_2O_3 fibers. Imaging analysis indicates that all the Ga_2O_3 fibers are nanocrystalline. While grain sizes (tens of nm) are too small to isolate a single grain for diffraction, selected area electron diffraction from a region allowed us to determine the crystal structure and specific phase of these materials. As is evident in the images, larger agglomerated regions are also present in the sample (image D). Thus, the TEM imaging analyses indicate the characteristic nanocrystalline features, dense and agglomeration of the nanofibers although the microstructure is fairly uniform across the samples analyzed.

The selected area electron diffraction (SAED) patterns of Ga_2O_3 nanofibers are shown in Fig. 30. The experimental and simulated patterns are shown for comparing the data and understand the phase stabilization in Ga_2O_3 nanofibers. First of all, it is evident that the SAED pattern exhibits a ring made up of bright spots that indicate that the nanofiber samples were composed of randomly oriented nano crystalline Ga_2O_3. The pattern was successfully indexed with ICDD PDF4+ database software and they match with the simulated diffraction patterns of Ga_2O_3. Thus, together with GIXRD analyses, the SAED analyses confirm the formation of nanocrystalline Ga_2O_3 fibers. Here the simulated pattern is shown at approximately the same magnification as the experimental pattern, and the arrows indicate the positions of the non-overlapping alpha-phase diffraction rings (which appear to be absent from the experimental pattern). The three innermost diffraction rings match the expected diffraction rings for beta phase (see Table). Thus, the electron diffraction analyses suggest that after the 900 °C heat treatment only β-phase is present**.** In the case of the

700°C and 800°C samples the TEM results do not indicate an initial formation of alpha phase gallium oxide or even the residual amounts indicated by xrd results. However, while this is not in agreement with previous data, there is corroborating evidence of both the more complete transition to the beta phase with increased heat treatment temperature as well as the improved crystallinity of the samples as indicated by the formation of distinct nanocrystals in the 800°C fibers not present in the lower temperature samples (Figures 29 E and 29F).

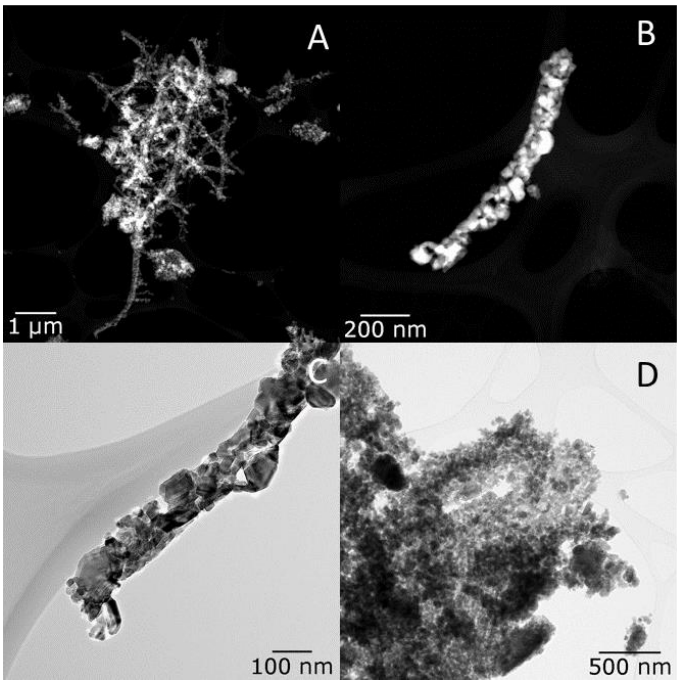

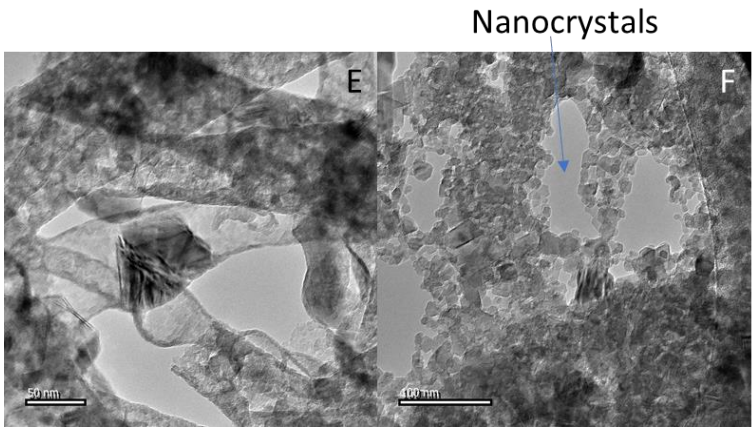

Figure 28: (A,B) High-angle annular dark-field scanning TEM (HAADF-STEM) and (C,D) bright-field (BF) TEM images of Ga-oxide nanofibers after 900°C, 2 hour heat treatment. The formation of nanocrystalline Ga-oxide fibers is evident in image A while higher magnification images (B,C) show the fiber structure and arrangement. Agglomerated regions are also present in the samples as indicated in image D. At the higher magnifications the formation of distinct nano crystals can be seen for an 800°C sample (F), this is not as the case for those fibers heat treated at 700°C (E)

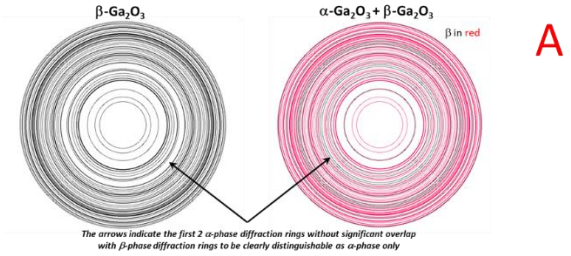

A

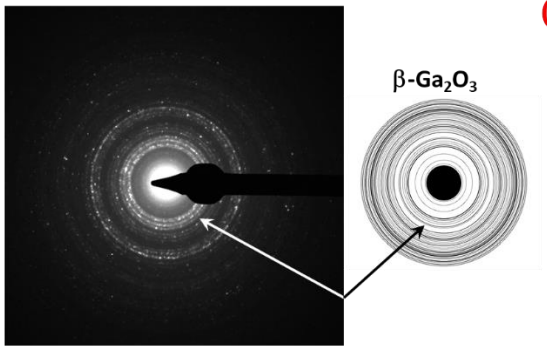

C

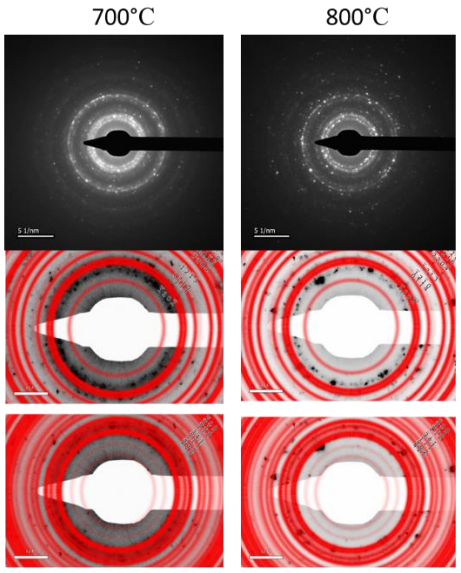

B

Diffraction Ring	Index (hkl)	d-spacing (Å)
1	001	5.63
2	20$\bar{1}$	4.68
3	201	3.67

D

Figure 29: A) sample differences between α and β gallium oxide diffraction rings B) Observed diffraction rings indicating for both 700°C and 800°C samples show transition to the β without conclusive evidence of residual α phase C) Diffraction pattern for 900°C D) index and d-spacing of selected diffraction rings

β - Ga_2O_3 exhibits monoclinic crystal symmetry with C2/m space group. From group theory symmetry analysis, the expected optical vibrational modes of Ga_2O_3 is 27, among these vibrational modes 15 are Raman active and 12 are infrared active (99). Raman spectra of Ga_2O_3 is classified into three regions; high frequency region (770 – 500 cm^{-1}) which includes stretching and bending modes of GaO_4 tetrahedra, phonon modes in mid frequency region (480 – 310 cm^{-1}) due to deformation of GaO_6 octahedra and phonon modes in low frequency region (below 200 cm^{-1}) due to oscillation and translation of Ga-O chains (100,101). Figure 31 shows the Raman spectra of as prepared and thermally annealed samples. Corroborating with XRD data, as prepared samples exhibit broader peaks indicating the amorphous nature of the fibers. However, it should be noted that most of the broader peaks still correspond to the skeleton of Ga_2O_3. The peak evolution and the trend as a function of thermally annealed samples clearly indicate the structural transformations and microstructure changes. The most important observation is the fact that the sharp and high intense phonon modes reveal that samples are highly crystallized. The nanofibers prior to heat treatment exhibit a smaller number of the phonon modes, blue shift in frequency of phonon modes clearly evident compare to bulk β-Ga_2O_3. A total of 6 phonon modes were found with two phonon modes in each region.

The cross section, surface morphology, and in particular, the crystallization behavior of electrospun fibers, are heavily influenced by the calcination temperatures and precursor concentrations within the solution (102,103). Greater and more uniform width and smoother

surface features are common in fibers with greater inorganic precursor concentrations, while morphologies ranging from dense cylindrical structures to ribbons or tubes are influenced by ratios of the precursor compounds to polymers in solution, as well as the evaporation rate of water, and polymer burn up rate (102,103). With an increase in temperature above 700 °C during calcination, PVP, the chosen polymer, becomes viscous and fibers begin to plasticize. Carbone monoxide and other gases and vapors from evaporating water and ethanol are released during polymer decomposition and based on diffusion rate of these gasses and the precursor chosen can lead to variations in the structure of the fibers as well as modify the exact crystallization process (102,103).

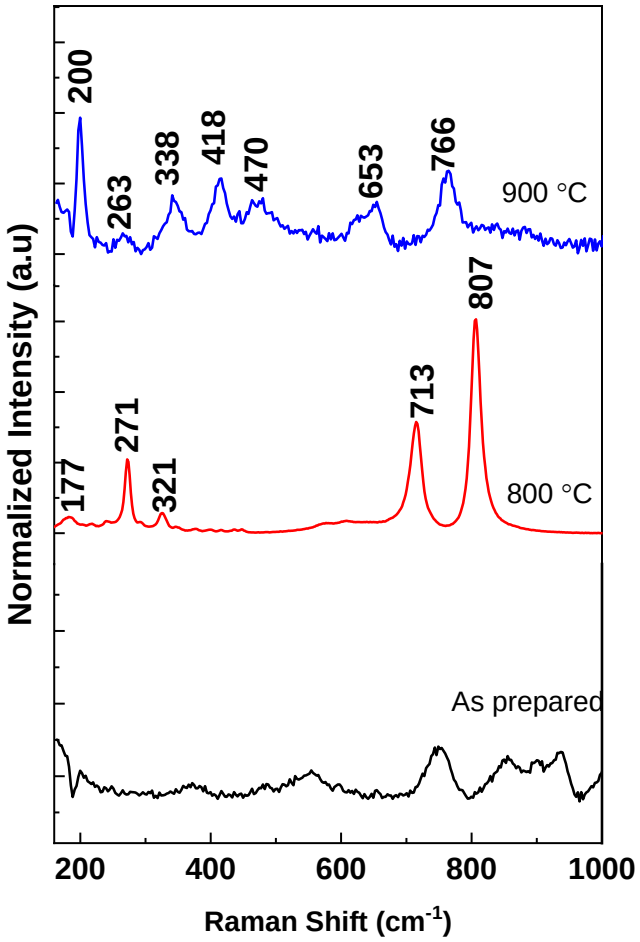

Figure 30: Raman spectra of samples as prepared and heat-treated Ga-oxide nanofibers

While the initial mechanism for Ga_2O_3 formation was assumed to be a direct decomposition of the Gallium nitrate precursor upon exposure to air at elevated temperatures leading to the initial formation of alpha phase Ga_2O_3, which in turn led to partial and then complete transformation into the beta phase polymorph higher temperatures (800-900°C); there is evidence gathered from the XRD and Raman spectroscopy data indicating a secondary formation mechanism, namely the presence of peaks indicative of GaO(OH) both in the as prepared and lower temperature samples. This chemical signature is potentially the result of an unintentional forced hydrolysis upon application of the current for the electrospinning procedure (104). This, combined with application

of elevated calcining temperatures that would lead to series of decomposition stages initiating with the formation of $Ga(OH)_2NO_3$ then leading to further breakdown into $Ga(OH)_3$ and $Ga(NO_3)O$, compounds before finally reaching the observed GaO(OH) and Ga_2O_3 phases present at the highest calcining temperatures(105).

$$Ga(NO_3)_3{\cdot}8.07H_2O(s) \rightarrow \rightarrow Ga(OH)_2(NO_3)(s)+N_2O_5(g)+7.07\ H_2O(g) \quad (21)$$

$$mGa(OH)_2(NO_3)(s) \rightarrow (m/2)Ga(OH)_3(s)+ +(m/2)Ga(OH)O(s)+(m/2)\ N_2O_5(g) \quad (22)$$

$$(1/2)Ga(OH)_3(s)+(1/2)Ga(OH)O(s) \rightarrow \rightarrow (1/2)Ga_2O_3(s)+H_2O \quad (23)$$

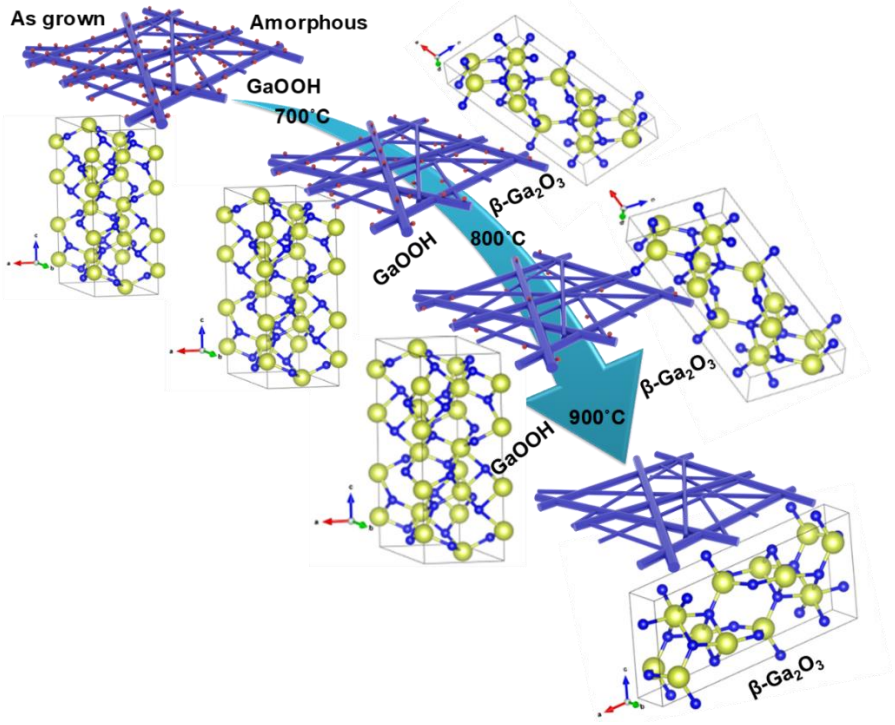

Figure31: Single phase amorphous hydroxide (GaO(OH)) to mixed-phase nanocrystalline oxide-hydroxide (GaO(OH) + β-Ga_2O_3) to single phase nanocrystalline β-Ga_2O_3 nanofibers

5.3.4 Electronic Structure and Optical Properties

The XPS core level spectra of Ga 2*p* region were probed to understand the electronic structure difference (if any) between the Ga-oxide nanofibers synthesized under variable processing conditions, especially those with a marked difference between α and β phase Ga_2O_3. In all the samples, the Ga $2p_{3/2}$ peak was located with a positive Binding Energy (BE) shift relative to the Ga metallic state indicating that the Ga ions exist in their higher valence state. Generally, the positive shift in the binding energy of Ga $2p_{3/2}$ core level peak is due to the redistribution of the electronic charge. On the other hand, very similar features and respective BE positions indicate that the Ga chemical state is stabilized in its highest oxidation state and is common in all of the Ga_2O_3 nanofibers. Specifically, no changes in BE location and/or peak shape were observed for the Ga 2*p* region as a function of either heat treatment of precursor concentration. This observation allows to conclude that the Ga ion chemical state is unaffected by any of these variable processing conditions or post processing thermal annealing and the Ga always exist in their highest chemical state (Ga^{3+}). However, the critical analysis of the oxygen core level peak explained the key differences arising in the chemical quality of the samples.

To further understand the mechanism and differences in nanofibers stabilizing in a specific phase, the high-resolution XPS data of O 1*s* in nanofibers are evaluated. It was noted that the O 1s peak is highly asymmetric for samples heat treated at lower temperatures while it becomes more or less symmetric in the samples heat treated at 900^{o}C. The asymmetric nature of the O 1*s* peak is, generally, indicative of oxygen bonded to different species (other than the host oxide matrix). Therefore, attempts were made to resolve the components by means of peak fitting. The asymmetric O 1*s* peak can be resolved into two component regions: (i) the first is the intense, main peak centered at BE~530.7 eV and (ii) two small shoulder peaks located at higher binding energies

at 532.2 eV and 533.4 eV. These three component peaks indicate three different chemical states or chemical bonding environments around oxygen in the Ga-oxide ceramic nanofibers. The main O 1*s* peak component with a major intensity corresponds to oxygen bonded to gallium (Ga-O bonds) as expected in stoichiometric Ga_2O_3. It has been reported in the literature that the O 1*s* peak for the stoichiometric, undoped Ga_2O_3 occurs generally at BE~530.5-531.0 eV. Comparison of the O 1*s* peak data indicates that the O 1*s* peak position occurs at a well-defined BE. Also, there is no appreciable peak shift in the BE position. These factors indicate the formation of Ga-O bonds, which are signature of stoichiometric Ga_2O_3, in all of the nanofibers. The shoulder peaks at BE 532.2 eV and 533.4 eV attributed to the surface oxygen bonded to carbon in the form of either carbonyl (oxygen bonded to carbon, C-O) or hydroxyl (oxygen bonded to hydrogen, O-H) groups. The presence of the carbonyl/hydroxyl component with a significant intensity for nanofibers at 700^{o}C compared to that of 900^{o}C indicates that the alpha phase stabilization may be due to the water incorporated into Ga_2O_3. These functional chemical groups may be included into the sample during synthesis and retained during pyrolysis of the polymer, as the synthetic approach to these nanofibers is based on solution-based chemistry. However, when the samples are thermally annealed at higher temperatures (900^{o}C), the hydroxyl component may be fully eliminated leading to the formation of beta phase Ga_2O_3.

5.4. Environmental Barrier Coating

5.4.1 Reaction Sequence

The short term infiltration tests of the various CMAS compositions as tested on the YSiFe and YDS coatings where done to determine crystallisation products and infiltration kinetics. The exact reaction products are heavily dependont on the composition of the CMAS the coatings are exposed two and are broadly characterized by an initial and secondary reaction as outlined in figure 33. The first reaction, highly dependent on calcium content of the CMAS, will tend to lead to formation of Apatite in calcium rich reaction, while calcium lean reactions will lead to more YDS formation. The former is preferred as it leads to a secondary reaction suitable for the formation of a garnet layer in the presence of sufficient Fe, Al, Mg, SI, or Ti which when formed will serve as a sacrifical type barrier layer preventing further consumption of the coating. Alternatively the secondary reaction may also yield YDS in the case of Ti content (TiO_2 in CMAS) in excess of 3 atomic %, along with insufficent levels of of the other constituent elements needed for garnet formation. In both cases where YDS is the primary reaction products without suffcient level of secondary elements (primarily Ca, Al, and Mg), rapid apatite formation without subsequent formation of garnet as a stabilizing/barreir layer can lead to coninual degradation and consumption of the coating over the coarse of exposure to the CMAS. (2,106-110). Table 2 summarizes the prinicple reaction products of the CMAS infiltration tests.

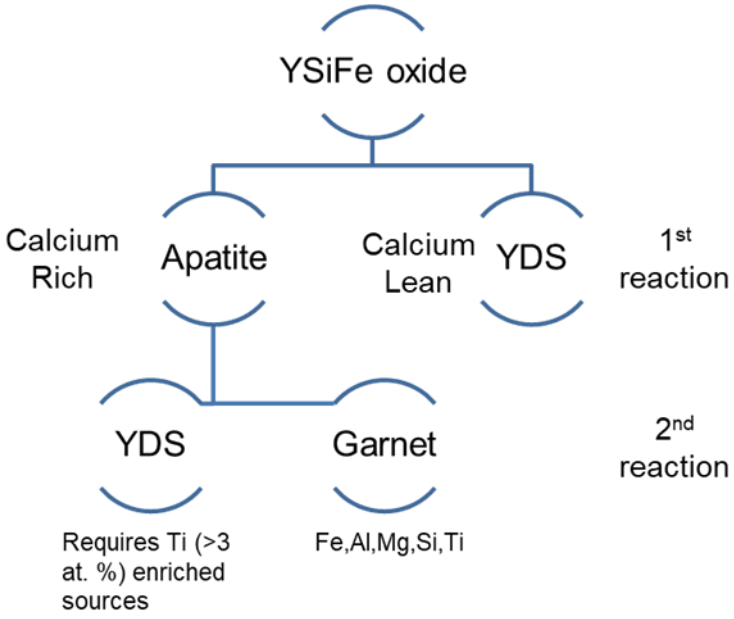

Figure 32: Reaction sequence of CMAS infiltration

Table 2: Summary of Reaction products

ID	Phase	Theoretical Formula
A	Apatite	$(Ca,Y)_4(Y,Zr)_6(SiO_4)O_2$
G	Garnet	$(Ca,Y,Zr)_3(Zr,Ti,Mg,Al,Fe)_2(Si,Al,Fe)_3O_{12}$
Y	YDS	$Y_2Si_2O_7$
AN	Anorthite	$CaAl_2Si_2O8$

5.4.2 CMAS Infiltration Studies- 10min 1300 °C: Alumina Substrate-CMAS1/2

Initial infiltration studies began with CMAS 1 and 2 applied to heat treated YSiFe coatings directly deposited on alumina substrates that were exposed to rapid heating to 1300 °C, maintaining that temperature for 10 minutes, before quenching to room temperature. The SEM imagery shown in figure 34A shows a cross section of the coating exposed to CMAS 1 showing minimal consumption of the coating, while 34B shows a thin reaction layer of approximately 2

μm that remains fairly constant throughout the main portion of the interface. A similar pattern can be seen in in 34C and 34B with CMAS 2 exposure. In both cases the porosity closer to the substrate seem larger and more prevalent compared to the surface portion of the coating, possibly an indication of sintering of the coating material caused by the reaction between the coating and substrate. EDS analysis of the images identified the primary reaction products as primarily garnet with anorthite forming within the CMAS melt itself. Sample compositions of the garnet phases formed from the exposure of the coating to CMAS 1 and 2 are presented in table 3.

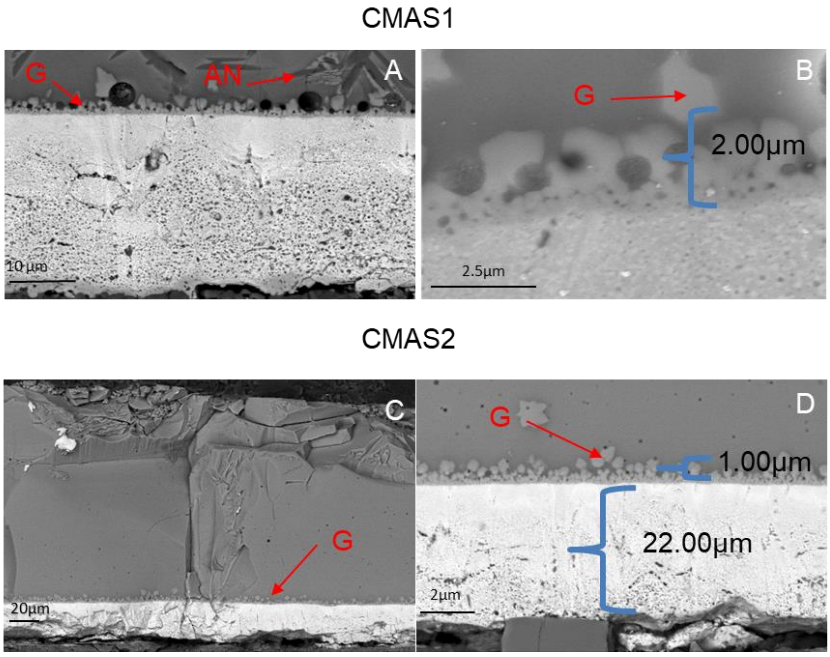

Figure 33: A) Overview of remaining coating for CMAS1, B) Reaction layer for CMAS1, C) Overview of remaining coating for CMAS2, D) Reaction layer for CMAS 2

Table 3: Sample composition of stable garnet phase reaction product from exposure of CMAS 1 and CMAS 2 to YSiFe coating for 10 min at 1300^{o} C for 10 minutes

At %	O	Mg	Al	Si	Ca	Ti	Fe	Y
CMAS1	50.87	4.5	5.62	15.33	10.75	1.2	7.12	4.61
CMAS 2	54.23	4.15	5.66	12.93	8.85	0.93	7.6	5.65

5.4.3 Calcium Lean Garnet formation

A phenomen observed during the 10 minute infiltration tests for the heat treated YSiFe coatings on alumina substrate that was not present for either the 1hr infiltration on alumina or 30 minute infiltrations on the full system was the apearance of calcium lean garnet formation as identified via EDS measurements. The atomic percentage of calcium in lean formation as in figure 35A and 35B varied between aproximately 50-90% lower compared to the the calcium rich areas shown in 35C and 35D. A sample of the reduced calcium levels of the garnet phases is shown in table 4, and it should be noted that this has resulted in excess consumption of other elements derived from the coating. There is also a distinct lack of Ti measured in the what comparatively little garnet has been formed reinforcing the fact that a distinct, and less stable phase of garnet has formed, that combined with increased apatite formation has lead to greater degradation of the coaitng. This deficiency is potentially due to the centralized reaction products consuming the majority of the calcium in the CMAS melt before the melt layer reaches and reacts with the side areas of the coating.

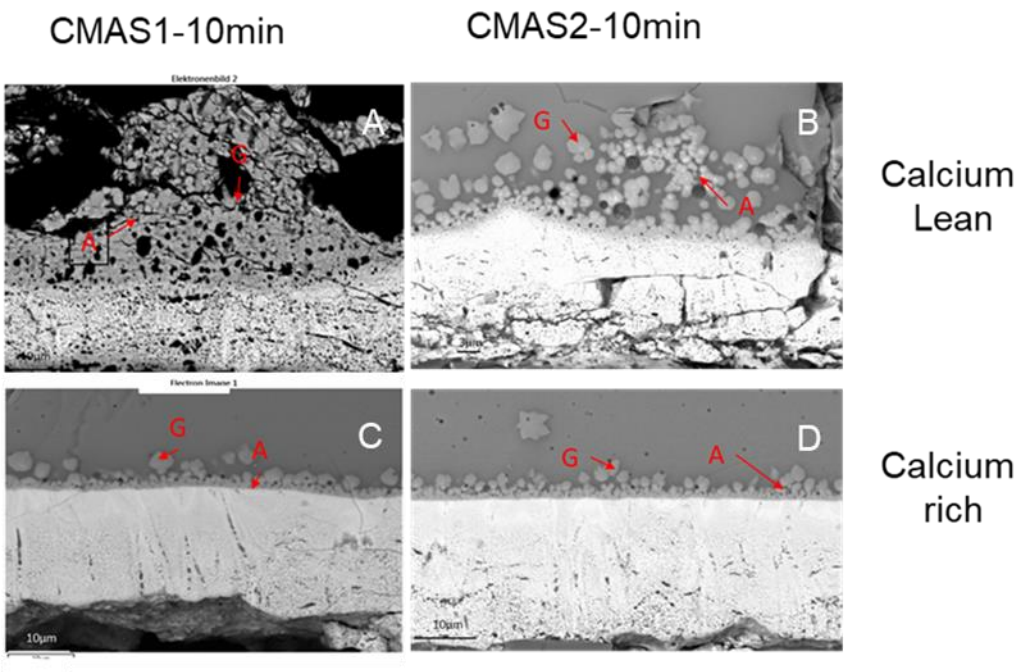

Figure 34: A) Overview of remaining coating for UCSB CMAS, B) Reaction layer for UCSB CMAS, C) Overview of remaining coating for Popocatepetl CMAS, D) Reaction layer for Popocatepetl CMAS

Table 4: Sample composition of calcium lean stable garnet phase reaction product from exposure of the UCSB and Popocatepetl CMAS to YSiFe coating at 1300^{o} C for 10 minutes

At %	O	Mg	Al	Si	Ca	Ti	Fe	Y
CMAS1	38.59	0.92	10.63	5.14	1.24	-	22.92	20.55
CMAS 2	61.92	0.57	6.07	9.86	0.41	-	4.07	17.11

5.4.4 CMAS Infiltration Studies- 1hr 1300 °C: Alumina Substrate-CMAS 1/2

The second set of infiltration tests kept the same parameters as set one, but increased isothermal heating time to 1hr. The results of this exposure, as seen in the cross-section SEM

image in figure 36A shows a significant breakdown and migration of the coating throughout the CMAS 1 melt. With figure 36B indicating as little as 4 μm remaining of the coating. A similar pattern was seen in figure 36C/D for CMAS 2. Interestingly, EDS analysis indicates that apatite and garnet remain the primary reaction products, with smaller amounts of Anorthite formation. A summary of the primary garnet phase formation is displayed in table 5. This breakup of the coating is inconsistent with previous work done on the YSiFe coatings under one hour exposure times as shown in figure 37, where the coating remained largely intact while forming similar apatite and garnet reaction products (111,112). It is unknown at this juncture whether the difference in coating integrity is a result of the CMAS composition, or some unexpected surge/drop in furnace temperature that may have introduced excessive thermal stresses to the system causing the coating break up.

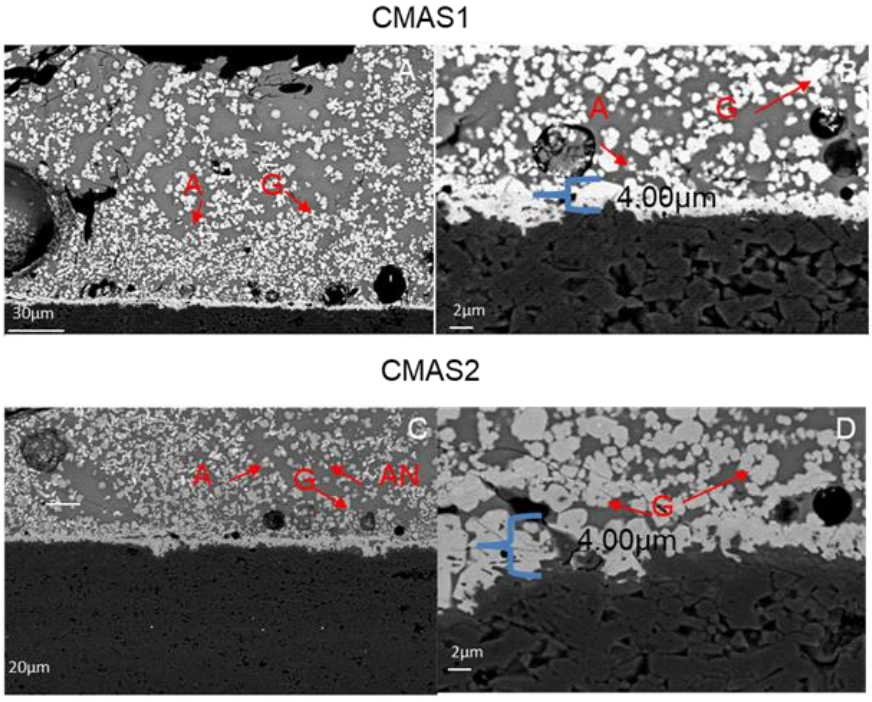

Figure 35: A) Overview of remaining coating for CMAS1, B) Reaction layer for CMAS1, C) Overview of remaining coating for CMAS2, D) Reaction layer for CMAS 2

Table 5: Sample composition of garnet phase reaction product from exposure of CMAS 1 and CMAS 2 to YSiFe coating at 1300^{o} C for 1 hour

At %	O	Mg	Al	Si	Ca	Ti	Fe	Y
CMAS1	58.84	3.7	7.53	8.97	4.55	0.28	6.36	9.76
CMAS 2	58.31	3.42	5.88	11.39	7.46	0.43	5.95	7.15

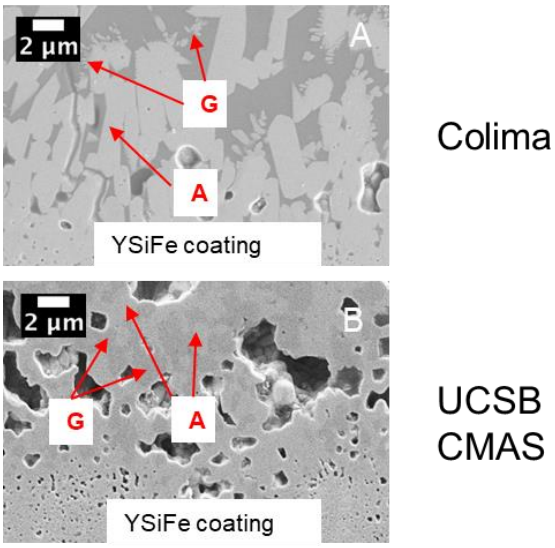

Figure 36: A) Reaction products and coating formation for Colima CMAS, B) Reaction products and coating formation for UCSB CMAS (110)

5.4.5 CMAS Infiltration Studies- 30 min 1300 °C: Full System-CMAS 1/2

The third set of infiltration tests focused on a simulated full EBC system making use of a SiC substrate, with a Si bond coat and YDS layer preceding the YSiFe top coat. As with the previous trials the sample was quickly heated in a 1300°C oven, before being isothermally heated for 30 min, followed by quenching to room temperature. The cross-section SEM shown in figure 38A shows that the overall system retains its integrity fairly well with larger cracks forming

primarily in the YDS layer, potentially due to greater than expected CTE mismatch. A similar pattern can be seen in the cross section shown in figure 38C exposed to CMAS2. It should be noted that that EDS analysis shows that the primary reaction products between the coating and CMAS in both cases remains apatite and garnet, as seen in figures 38B/D. A sample composition of the stable garnet phases is shown in table 6. In both a fairly rapid assumed conversion from apatite to garnet has formed a continuous reaction layer preventing excessive coating consumption at the interface. It was also observed that there was some diffusion of the YDS layer into the YSiFe. These diffused areas tend to display greater porosity compared to the rest the top coat and also tend to correlate with the beginnings of some of the larger cracks visible in the YDS, possibly due to weakening of the local structure. Such excessive cracking, shown in figure 39, can lead to CMAS infiltration and reaction products forming within the top coat itself, drastically weakening the layer and compromising protection from further infiltration.

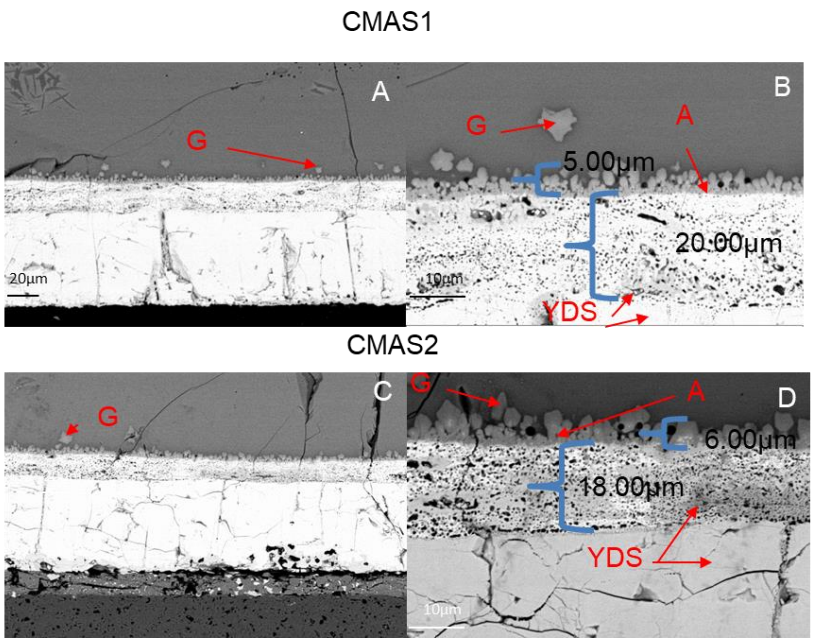

Figure 37: A) Overview of remaining coating for CMAS1, B) Reaction layer for CMAS1, C) Overview of remaining coating for CMAS2, D) Reaction layer for CMAS 2

Table 6: Sample composition of calcium lean stable garnet phase reaction product from exposure of CMAS 1 and CMAS 2 to YSiFe coating at 1300^{o} C

At %	O	Mg	Al	Si	Ca	Ti	Fe	Y
CMAS1	58.93	4.26	4.65	12.88	8.6	0.99	5.75	3.93
CMAS 2	60.48	3.98	1.88	13.23	10.15	1.08	5.63	3.59

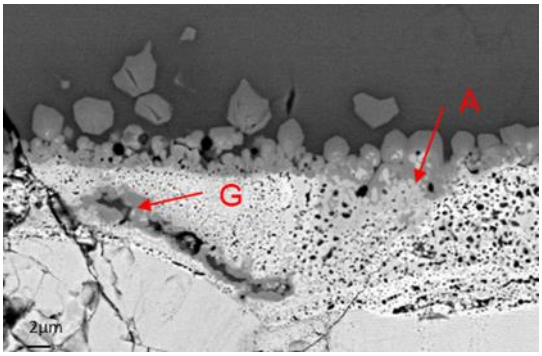

Figure 38: Sample cross section with excessive porosity and cracking

5.4.6 CMAS Infiltration Studies- 30 min 1300 °C: YDS on Alumina-CMAS1/2

The fourth set of infiltration studies was to determine the effect of the artificial CMAS composition on pure YDS, on its own considered fairly good for EBC applications in terms of water vapor resistance. As with the other trials, the samples were isothermally heated at 1300 °C for 30 minutes before quenching. Cross section imagery in figures 40A/B show that in the case of both CMAS1 and 2 the coating was almost completely consumed with EDS mapping identify extensive anorthite formation in the former and sublimation into the glass phase in the latter. This is largely due to the lack of Fe in the coating, preventing the successful transition process from apatite to the garnet phase and the subsequent arresting of the coating reaction and consumption.

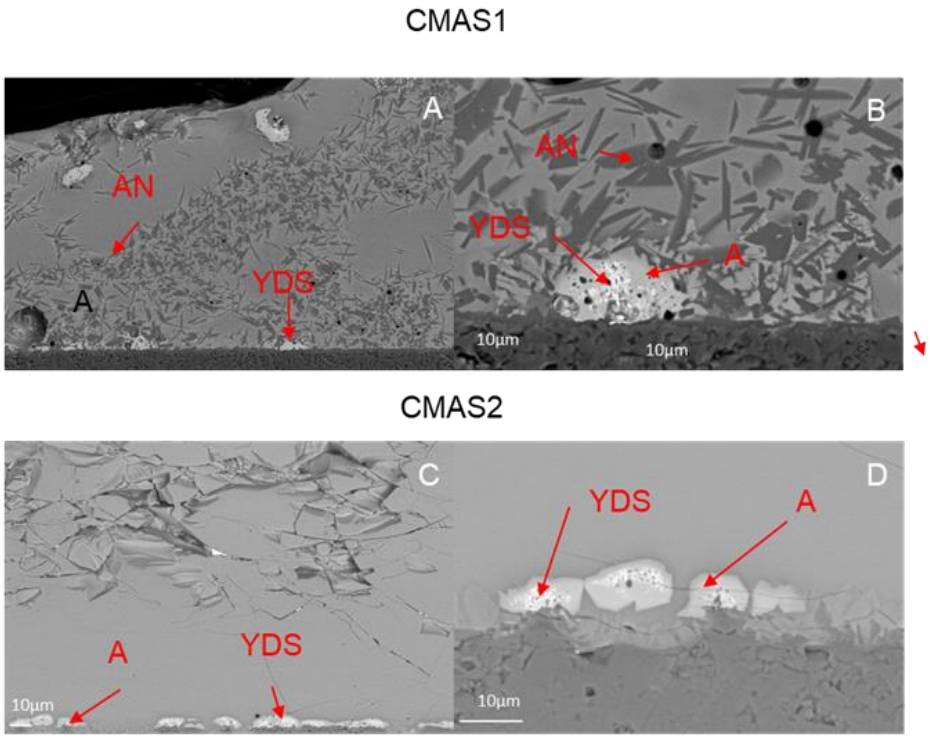

Figure 39: A) Overview of remaining coating for CMAS1, B) Reaction layer for CMAS1, C) Overview of remaining coating for CMAS2, D) Reaction layer for CMAS 2

5.4.7 CMAS Infiltration Studies- 30min 1300 °C: YDS on Alumina -UCSB/Popocatepetl

The fifth infiltration studies involved exposure of the same type of pure YDS on alumina samples to the UCSB and Popocatepetl CMAS to further expand the information available on the effects of CMAS on traditional EBC components. These samples follow an identical isothermal heating and quenching regime as the fourth trial being held at 1300 °C for 30 minutes before being rapidly cooled to room temperature. The SEM imagery shown in figure 41A/B show a total consumption of the YDS coating when exposed to the UCSB CMAS. EDS analysis indicates complete consumption into the glass phase with trace amounts of anorthite formation. This is very similar to the sample exposed to CMAS 2 and to be expected given their similar compositions with substantially higher, relative to CMAS1, Ca levels seemingly the driving factor in glass

sublimation. Conversely, the SEM imagery and EDS analysis for the sample exposed to the Popocatepetl CMAS (figures 41C/D), show almost no degradation in the coating at all. This can be attributed to low Ca, Al, and Mg content in the CMAS preventing formation of the apatite phase and subsequent absorption into the glass melt.

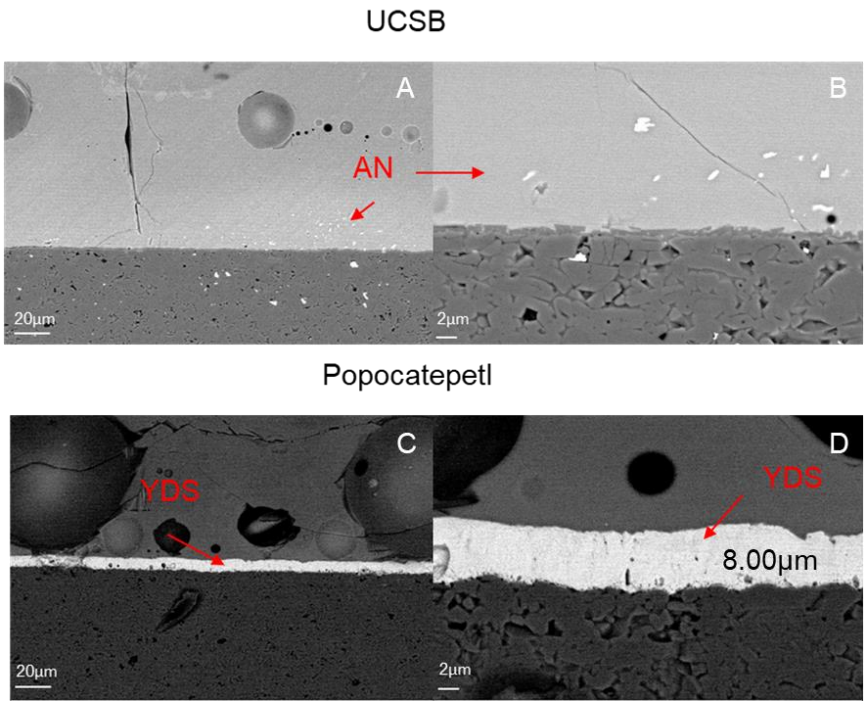

Figure 40: A) Overview of remaining coating for UCSB CMAS, B) Reaction layer for UCSB CMAS, C) Overview of remaining coating for Popocatepetl CMAS, D) Reaction layer for Popocatepetl CMAS

6. Summary and Conclusions

6.1 RF Magnetron Sputtered Gallium Oxide

The effect of post-deposition thermal annealing on the crystallization or growth process, crystal chemistry, mechanical properties, refraction index profiles, and electrical characteristics of sputter-deposited, nanocrystalline Ga_2O_3 films has been evaluated. It can be concluded that annealing plays a major role in altering the structure and morphology of the Ga_2O_3 films. The thermal annealing to 800−900 °C improves the structural quality and packing density of the Ga_2O_3 films. While the films annealed at intermediate temperatures (up to 700 °C) become exceedingly rough, Ga_2O_3 films annealed at 800−900 °C exhibit relatively smoother morphology, distribution characteristics and optical quality. The refraction index values at 632 nm increase from 1.78 to 1.84 that corroborates with gradual improvement of structural quality, texturing, and packing density upon thermal annealing at 800− 900 °C. The correlation established between annealing temperature and optical and electrical characteristics in Ga_2O_3 films may useful and can serve as foundation nanocrystalline Ga_2O_3 films for application in sensors and optical and optoelectronic devices.

6.2 PLD Gallium Oxide

We demonstrated an approach based on selective engineering of the size-, phase-, and interface nanostructure-controlled β-Ga_2O_3 films to realize reliable and highly intense green-emission PL without the need for expensive processing, epitaxial system, and dopants. In nanocrystalline β-Ga_2O_3 films with an average crystallite size of ~9 nm, the green-emission PL noted is remarkable and is extremely high (~30 times). Structural and interface nanostructure analyses indicate that high-quality nanocrystalline β-Ga_2O_3 films with highly dense and

interconnected nanocolumnar structures promote enhanced optoelectronic performance. We believe that there may be further options available to further tune and improve the optoelectronic performance, while the underlying science and mechanisms may be applicable to a large class of wide-band-gap nanostructured oxides for optical, electronic, and optoelectronic devices for extreme environment applications.

6.3 Gallium Oxide Nanofibers

The effect of processing parameters on the properties of Ga_2O_3 nanofibers were evaluated by X-ray diffraction (XRD), scanning electron microscopy (SEM), transmission electron microscopy (TEM), X-ray photoelectron spectroscopy (XPS) and Raman spectroscopy. Thermal treatments in the range of 700-900^{o}C induces crystallization of amorphous fibers and leads to phase stabilization of α-Ga_2O_3, β-Ga_2O_3, or mixtures of these phases. The XRD and TEM selected area electron diffraction analyses indicate that the transformation sequence progresses by forming the metastable α-Ga_2O_3 nanofibers at low temperature (700^{o}C), mixtures of α-Ga_2O_3 and β-Ga_2O_3 at intermediate temperatures (800^{o}C), fully transforms to β-Ga_2O_3 phase at higher temperatures (900^{o}C). Raman spectroscopic analyses corroborate the structural evolution and confirms high chemical quality of the β-Ga_2O_3 nanofibers. The electronic structure probed by XPS indicate that the hydroxyl groups present for the samples treated at lower temperatures account for the α-Ga_2O_3 phase formation. However, treatment at higher temperatures fully removes those hydroxyl groups resulting in the formation of β-Ga_2O_3 nanofibers.

6.4 Environmental Barrier Coating

Based on the infiltration studies performed several conclusions can be drawn from application of varied CMAS compositions to candidate EBC materials. Firstly, YDS on its own

can be considered generally unsuited for EBC coatings in terms of its CMAS resistance. Any exposure to CMAS with sufficiently high Ca and other necessary, and fairly common, constituents such as Mg or Al will lead to anorthite and apatite formation without any stabilizing elements causing rapid coating consumption.

Alternatively, introduction of FeO into the Y/YSi system leads to substantially improved CMAS resistance while theoretically maintaining low water vapor recession rates. This is caused by the assumed initial apatite formation rapidly undergoing transformation into garnet due to the effects of elevated Fe content, leading to phase stability and minimized reactions with molten CMAS. It should be noted that, just as with the case of the YDS, the effectiveness will be highly dependent on the precise CMAS composition with unfavorable constituent elements potentially leading to a lack of transition to the south after garnet phase. Additionally, cracking and excessive porosity formation in a full EBC system using such coating are possibly due to diffusion from YDS layers and CTE mismatch among the various components of the system.

7. Future Work

Further research into the practical applications of the materials studied in this project would focus around their integration into sensors and structural components and subsequent evaluation of their performance in simulated conditions.

In terms of the gallium oxide based nanostructured materials, they would likely be deposited onto interdigitated electrodes and undergo testing in elevated temperature environments (700 ° C and above) to determine their response and recovery times when functioning as chem-resistive sensors. While PLD and Magnetron sputtering are both suitable methods for direct deposition onto electrodes, the inherently brittle nature of the calcined gallium oxide nanofibers will necessitate an alternate integration method that maintains structural integrity without compromising the sensitivity of the sensor

In order to better understand the mechanics of the YSiFe coating and its effectiveness in its intended role as part of an EBC system additional testing is required including the repeating of 1hr testing to see if coating decomposition is a consistent phenomenon as well as extend the testing period to long term (potentially 50hr +) to effectively compare the results with similar work done on other CMAS compositions. Since the UCSB and Popocatepetl CMAS has already been tested on YDS, they should also be applied to the YsiFe coating to determine their effects on structural integrity of the system. In relation to that, additional XRD/TEM analysis is pending to more accurately determine phase formation.

The final stages of the research would be combining the sensors and protective coatings onto a simulated high temperature gas turbine environment. The sensors themselves would ideally be incorporated into the surface of the protective barrier coatings and could make use of high

temperature substrate material such as YSZ, MgO, or Alumina to facilitate integrate with an interdigitated electrode. The primary challenge would lie in ensuring sufficient gas flow over the sensors to achieve meaningful measurements, without compromising the integrity of the protective coatings.

References

1. Spirig, J. V, Ramasamy R., Sheikh A. A., Jules, L. R., Singh, D., Dutta, P. K. 2007. "High temperature zirconia oxygen sensor with sealed metal/metal oxide internal reference." Sensors and Actuators B: Chemical 124 (1):192-201.
2. Poerschke, D. L., Jackson R. L., Levi C. G. Silicate Deposit Degradation of Engineered Coatings in Gas Turbines: Progress Toward Models and Materials Solutions, *Annu. Rev. Mater*. **2017** Res. 47, pp. 297-330
3. Kumar, S. S., Rubio, E., Noor-A-Alam, M., Martinez, G., Manandhar, S., Shutthanandan, V., Thevuthasan, S., Ramana, C.V., Structure, Morphology, and Optical Properties Of Amorphous And Nanocrystalline Gallium Oxide Thin Films. *The Journal of Physical Chemistry C* **2013,** *117* (8), 4194-4200.
4. Zhang, W., Naidu, B.S., Ou, J. Z., O'Mullane, A.P., Chrimes, A. F., Carey, B. J., Wang, Y., Tang, S. Y., Sivan, V., Mitchell, A., Bhargava, S.K., Kalantar-zadeh, K., Liquid Metal/Metal Oxide Frameworks with Incorporated Ga_2O_3 for Photocatalysis. *ACS Appl. Mater. Interfaces* **2015,** 7, 1943-1948
5. Mu, W., Jia, Z., Cittadino, G., Yin, Y., Luperini, C., Hu, Q., Li, Y., Zhang, J., Tonelli, M., Tao, X., Ti-Doped β-Ga_2O_3: A Promising Material for Ultrafast and Tunable Lasers. *Crystal Growth & Design* **2018**, 18 (5), 3037-3043.
6. Zade, V., Mallesham, B., Shantha-Kumar, S., Bronson, A., Ramana, C. V., Interplay between Solubility Limit, Structure, and Optical Properties of Tungsten-Doped Ga_2O_3 Compounds Synthesized by a Two-Step Calcination Process. *Inorganic Chemistry* **2019**, 58, 3707-3716.

7. Zhang, J., Shi, J., Qi, D.-C., Chen, L., Zhang, K. H. L. Recent Progress on the Electronic Structure, Defect, and Doping Properties of Ga_2O_3. *APL Materials.* **2020,** 8, 020906
8. Mazeina, L., Picard, Y.N., Maximenko, S.I., Perkins, F.K., Glaser, E.R., Twigg, M.E., Freitas Jr., J.A., Prokes, S.M., Growth of Sn-Doped β-Ga_2O_3 Nanowires and Ga_2O_3−SnO_2 Heterostructures for Gas Sensing Applications, *Crystal Growth & Design* **2017**, 9, 4471-4479.
9. Rafique, S., Han, L., Zorman, C. A., Zhao, H. Synthesis of Wide Bandgap β-Ga_2O_3 Rods on 3C-SiC-on-Si. *Crystal Growth & Design* 2016, *16,* 511– 517,
10. Sun, H., Li, K.-H., Torres Castanedo, C.G., Okur, S., Tompa, G.S., Salagaj, T., Lopatin, S., Genovese, A., Li, X. HCl Flow-Induced Phase Change of α-, β-, and ε-Ga_2O_3 Films Grown by MOCVD. *Crystal Growth & Design* 2018, 1842370-2376.
11. Bartic, M., Baban, C. I., Suzuki, H., Ogita, M., Isai, M., β-Gallium Oxide as Oxygen Gas Sensors at a High Temperature. *Journal of the American Ceramic Society* **2009,** *90* (9), 2879-2884.
12. Ogita, M., Higo, K., Nakanishi, Y., Hatanaka, Y., Ga_2O_3 Thin Film for Oxygen Sensor at High Temperature. *Applied Surface Science* **2001,** *175*, 721-725.
13. Pearton, S. J., Yang, J., Cary, P.H., Ren, F., Kim, J., Tadjer, J. M., Mastro, M. A., A Review of Ga_2O_3 Materials, Processing, and Devices. *Appl. Phys. Rev.* **2018**, 5, 011301-011356.
14. Yang, G., Jang, S., Ren, F., Pearton, S. J., Kim, J. Influence of High-Energy Proton Irradiation on β-Ga_2O_3 Nanobelt Field-Effect Transistors. *ACS Applied Materials & Interfaces* **2017**, *9* (46), 40471–40476.

15. Jamison, J.S., May, B.J., Chien, S-C., McComb, D.W., Grassman, T.J., Windl, W., Myers, R.C. Ferromagnetic Epitaxial μ-Fe_2O_3 on β-Ga_2O_3: A New Monoclinic Form of Fe_2O_3. *Crystal Growth & Design* **2019**, in press (DOI:. doi.org/10.1021/acs.cgd.9b00029).
16. Peelaers, H., Van de Walle, C. G., Brillouin Zone and Band Structure of β-Ga_2O_3. *physica status solidi (b)* **2015,** *252* (4), 828-832.
17. Tomm, Y., Ko, J., Yoshikawa, A., Fukuda, T., Floating zone growth of β-Ga_2O_3: a new window material for optoelectronic device applications. *Solar Energy Materials and Solar Cells* **2001,** *66* (1-4), 369-374.
18. Zhang, Y., Yan, J., Li, Q., Qu, C., Zhang, L., Xie, W., Optical and Structural Properties of Cu-doped β-Ga_2O_3 films. *Materials Science and Engineering: B* **2011,** *176* (11), 846-849.
19. He, H., Orlando, R., Blanco, M. A., Pandey, R., Amzallag, E., Baraille, I., Rérat, M., First-principles study of the structural, electronic, and optical properties of Ga_2O_3 in its monoclinic and hexagonal phases. *Physical Review B* **2006,** *74* (19), 195123.
20. Yoshioka, S., Hayashi, H., Kuwabara, A., Oba, F., Matsunaga, K., Tanaka, I., Structures and energetics of Ga_2O_3 polymorphs. *Journal of Physics: Condensed Matter* **2007,** *19* (34), 346211.
21. Ramana, C.V., Properties of Sputter-Deposited Gallium Oxide. In *Gallium Oxide*, Elsevier: **2019**, pp 47-66.
22. Irfan, I., Gao, Y. Effects of Exposure and Air Annealing on MoO_x Thin Films. *Journal of Photonics for Energy* **2012**, 2, 021213.
23. Choong-Ki. Kim, Eungtaek Kim, Myung Keun Lee, Jun-Young Park, Myeong-Lok Seol, Hagyoul Bae, Tewook Bang, Seung-Bae Jeon, Sungwoo Jun, Sang-hee K. Park, Kyung Cheol Choi, and Yang-Kyu Choi. An Electro-thermal annealing (ETA) Method to Enhance

the Electrical Performance of Amorphous-Oxide-Semiconductor (AOS) Thin-Film Transistors (TFTs). *ACS Applied Materials & Interfaces* **2018**, 8, 23820-23826.

24. Ke, W., Zhao, D., Cimaroli, A.J., Grice, C.R., Qin, P., Liu, Q., Xiong, L., Yan, Y., Fang, G. Effects of Annealing Temperature of Tin Oxide Electron Selective Layers on The Performance of Perovskite Solar Cells, *Jounral of Materials Chemistry A* **2015**, 3, 24163-24168.
25. Son, N.T., Goto, K., Nomura, K., Thieu, Q.T., Togashi, R., Murakami, H., Kumagai, Y., Kuramata, A., Higashiwaki, M., Koukitu, A., Yamakoshi, S., Monemar, B., Janzén, E. Electronic Properties of the Residual Donor in Unintentionally Doped β-Ga_2O_3. *Journal of Applied Physics* **2016**, 120, 235703.
26. Cao, Q., He, L., Feng, X., Xiao, H., Ma, J., Effect of Annealing on the Structural and Optical Properties of β-Ga_2O_3 Films Prepared on Gadolinium Gallium Garnet (110) by MOCVD, *Ceramics International* **2018,** *44*, 830-835.
27. Kim, H.W., Kim, N.H., Annealing Effects on the Properties of β-Ga_2O_3 Thin Films Grown on Sapphire by Metal Organic Chemical Vapor Deposition. *Applied Surface Science* **2004**, *230*, 301-306.
28. Gogova, D., Wagner, G., Baldini, M., Schmidbauer, M., Irmscher, K., Schewski, R., Galazka, Z., Structural Properties of Si-doped *β*-Ga_2O_3 Layers Grown by MOVPE, *Journal of Crystal Growth* **2014**, *401*, 665-669.
29. Feng, Z., Huang, L., Feng, Q., Li, X., Zhang, H., Tang, W., Zhang, J., Hao, Y., Influence of Annealing Atmosphere on the Performance of a β-Ga_2O_3 Thin Film and Photodetector. *Optical Materials Express* **2018**, *8* (8), 2229

30. Goyal, A., Yadav, B.S., Thakur, O.P., Kapoor, A.K., Muralidharan, R. Effect of Annealing on β-Ga_2O_3 Thin Film Grown by Pulsed Laser Deposition Technique, *Journal of Alloys & Compounds* **2014**, *583*, 214-219.

31. Harada, T., Ito, S., Tsukazaki, A. Electric dipole effect in PdCoO2/β-Ga_2O_3 Schottky diodes for high-temperature operation. Sci. Adv. **2019**, 5, 5733.

32. Yang, G., Jang, S., Ren, F., Pearton, S. J., Kim, J. Influence of High-Energy Proton Irradiation on β-Ga_2O_3 Nanobelt Field-Effect Transistors. ACS Appl. Mater. Interfaces **2017**, 9, 40471−40476.

33. Anhar Uddin Bhuiyan, A. F. M., Feng, Z., Johnson, J. M., Huang, H. L., Hwang, J., Zhao, H. MOCVD Epitaxy of Ultrawide Bandgap β-(AlxGa1−x)2O3 with High-Al Composition on (100) βGa_2O_3 Substrates. Cryst. Growth Des. **2020**, 20, 6722−6730.

34. Simeone, F. C., Yoon, H. J., Thuo, M. M., Barber, J. R., Smith, B., Whitesides, G. M. Defining the value of injection current and effective electrical contact area for EGaIn-based molecular tunneling junctions. J. Am. Chem. Soc. **2013**, 135, 18131−18144.

35. Um, H. J., Kong, G. D., Yoon, H. J. Thermally Controlled Phase Transition of Low-Melting Electrode for Wetting-Based Spontaneous Top Contact in Molecular Tunnel Junction. ACS Appl. Mater. Interfaces **2018**, 10, 34758−34764.

36. Huso, J., McCluskey, M. D., Yu, Y., Islam, M. M., Selim, F. Localized UV emitters on the surface of β-Ga_2O_3. Sci. Rep. **2020**, 10, 21022.

37. Cho, J. B., Jung, G., Kim, K., Kim, J., Hong, S.-K., Song, J.-H., Jang, J. I. Highly Asymmetric Optical Properties of β-Ga_2O_3 as Probed by Linear and Nonlinear Optical Excitation Spectroscopy. J. Phys. Chem. C **2021**, 125, 1432−1440.

38. Zhou, X. T., Heigl, F., Ko, J. Y. P., Murphy, M. W., Zhou, J. G., Regier, T., Blyth, R. I. R., Sham, T. K. Origin of luminescence from Ga_2O_3 nanostructures studied using x-ray absorption and luminescence spectroscopy. Phys. Rev. B: Condens. Matter Mater. Phys. **2007**, 75, 125303.

39. Ramana, C. V., Rubio, E., Barraza, C., Miranda Gallardo, A., McPeak, S., Kotru, S., Grant, J. Chemical Bonding, Optical Constants, and Electrical Resistivity of Sputter-Deposited Gallium Oxide Thin Films. *Journal of Applied Physics*, vol. 115, no. 4, **2014**, pp. 043508.

40. Nakagomi, Shinji, and Yoshihiro Kokubun. Crystal Orientation of β-Ga_2O_3 Thin Films Formed on c-Plane and a-Plane Sapphire Substrate. *Journal of Crystal Growth*, vol. 349, no. 1, 15, **2012**, pp. 12–18.

41. Oshima, T., Niwa, M., Mukai, A., Nagami, T., Suyama, T., Ohtomo, A. Epitaxial Growth of Wide-Band-Gap ZnGa2O4 Films by Mist Chemical Vapor Deposition. *Journal of Crystal Growth*, vol 386, **2013,** pp 190-193

42. Guo, D. Y., Wu, Z.P., An, Y.H., Guo, X.C., Chu, X.L., Sun, C.L., Li, L.H., Li, P.G., Tang, W.H. Oxygen Vacancy Tuned Ohmic-Schottky Conversion for Enhanced Performance in β-Ga_2O_3 Solar-Blind Ultraviolet Photodetectors *AIP Publishing*, vol 105, **2014**,

43. Sontheimer, Tobias, Amkreutz, D., Shulz, K., Wobkenberg, P. H., Guenther, C., Bakumov, V., Erz, J., Mader C., Traut, S., Ruske, F., Weizman, M., Schnegg, A., Patz, M., Trocha, M., Wunnicke, O., rech, B. Solution-Processed Crystalline Silicon Thin-Film Solar Cells. *Advanced Materials Interfaces*, vol 1, no 3, **2014**

44. Rebien, M., Henrion, W. Optical Properties of Gallium Oxide Thin Films. *Applied Physics Letters*, vol. 81, no. 2, **2002**, pp. 250–252.

45. Zhou, T., Chen, P., Hu, S., Yan, Y., Pan, W., Li, H. Enhanced Yellow Luminescence of Amorphous Ga_2O_3 Nanofibers with Tunable Crystallinity. *Ceramics International* **2016**, *42* (5), 6467–6474.
46. Zang, S. Mechanical and physical properties of electrospun nanofibers. master's thesis, North Carolina State University, **2009**, NCSU libraries.
47. Ramana, C. V., Becker, Ul., Shutthanandan, V., Julien, C. Oxidation and Metal-Insertion in Molybdenite Surfaces: Evaluation of Charge-Transfer Mechanisms and Dynamics. *Geochemical Transactions*, vol. 9, no. 1, **2008**.
48. Nikolaev, V.I., Maslov, V., Stepanov, S.I., Pechnikov, A.I., Krymov, V., Nikitina, I.P., Guzilova, L.I., Bougrov, V.E., Romanov, A.E. Growth and Characterization of β-Ga_2O_3 Crystals. *Journal of Crystal Growth*, vol. 457, 2017, pp 132-136
49. Takakura, K., Koga, D., Ohyama, H., Rafi, J.M., Kayamoto, Y., Shibuya, M., Yamamoto, H., Vanhellemont, J., Evaluation of the Crystalline Quality of β-Ga_2O_3 Films by Optical Absorption Measurements. *Physica B: Condensed Matter*, vol. 404, no. 23-24, **2009**, pp. 4854–4857.
50. Gönüllü, Yakup, Rodriguez, G. C. M., Saruhan, B., Urgen, M. Improvement of Gas Sensing Performance of TiO2 towards NO2 by Nano-Tubular Structuring." *Sensors and Actuators B: Chemical*, vol, 169, **2012**, pp. 151-160.
51. Zheng, W., Li, Z., Zhang, H., Wang, W., Wang, Y., Wang, C. Electrospinning Route for α-Fe2O3 Ceramic Nanofibers and Their Gas Sensing Properties. *Materials Research Bulletin* **2009**, *44* (6), 1432–1436.

52. Rao, R., Rao, A. M., Xu, B., Dong, J., Sharma, S., Sunkara, M. K. Blueshifted Raman Scattering and Its Correlation with the [110] Growth Direction in Gallium Oxide Nanowires. *Journal of Applied Physics* **200**5, *98* (9), 094312.
53. Wu, H., Pan, w. Preparation of Zinc Oxide Nanofibers by Electrospinning. *Journal of the American Ceramic Society*, vol. 89, no. 2, **2006**, pp. 699–701.
54. Wu, Hui, Lin, D., Zhang, R., Pan, W. ZnO Nanofiber Field-Effect Transistor Assembled by Electrospinning." *Journal of the American Ceramic Society*, vol. 91, no. 2, **2008**, pp. 656–659.
55. Zhu, D. Aerospace Ceramic Materials: Thermal, Environmental Barrier Coatings and SiC/SiC Ceramic Matrix Composites For Turbine Engine Applications, Glenn Research Center, Cleveland, Ohio, (2018)
56. Padture, N. P. Advanced structural ceramics in aerospace propulsion, *Nature Materials*, **2016**, **15**, pp. 804-809
57. Schulz, U. , Leisner, V., Lange, A., Mechnich, P., Mauer, C. Environmental Barrier Coatings for SiC based CMCs, Cologne **2015**
58. Levi, C. G., Hutchinson, J. W., Vidal-Sétif M.-H., Johnson, C. A. Enviromental degradation of thermal-barrier coatings by molten deposits, *MRS Bulletin*, vol 37**2012**, pp. 932-941
59. Argirusis, C. , Damjanović, T., Borchardt, G. Yttrium silicate coating system for oxidation protection of C/C-Si-SiC composites: Electrophoretic deposition and oxygen self-diffusion measurements, *Journal of the European Ceramic Society*, vol 27, no. 2-3, **2007**, pp. 1303–1306

60. Ott A. S. CMAS/Volcanic ash resistant coatings for TBC and EBC applications based on a novel Y-Si-Fe oxide system, Master's Thesis. **2018** University of Cologne
61. Sun, Z., Li, M., Zhou, Y. Recent progress on synthesis, multi-scale structure, and properties of Y–Si–O oxides, *International Materials Reviews*, vol 59, no. 7, **2014,** pp. 357-383 ()
62. Parmentier, J., Liddell, K., Thompson, D. P., Lemercier, H., Schneider, N., Hampshire, S., Bodart, P. R., Harris, R. K. Influence of iron on the synthesis and stability of yttrium silicate apatite, *Solid State Sciences*, vol. 3, **2001,** pp. 495-502 ()
63. Naraparaju, R., Gomez Chavez, J. T., Schulz, U., Ramona, C. V. Interaction and infiltration behavior of Eyjafjallajokull, Sakurajima volcanic ashes and a synthetic CMAS containing FeO with/in EBPVD ZrO2-65 wt% Y2O3 coating at high temperature, *Acta Materialia,* vol 136**2017**, pp. 164-180 ()
64. Koenig, H. R., and L. I. Maissel. Application of RF Discharges to Sputtering. *IBM Journal of Research and Development*, vol 14(2)**1970**. 168-171. doi: 10.1147/rd.142.0168.
65. Julian, J., Clare, A. Bio-glasses L an Introduction: *John Wiley & Sons.* New York **2012**
66. Nalwa, H.S. Nanomaterials and Magnetic Thin Films, Hanbook of Thin Film Materials Vol. 5, *Academic Press, New York,* **2002**
67. Eason, R. Pulsed Laser Deposition of Thin Films: Applications-Led Growth of Functional Materials. *Wiley Interscience*, Hoboken, New Jersey, **2007,**
68. Abràmoff, Michael D, Paulo J Magalhães, and Sunanda J Ram. Image processing with ImageJ. *Biophotonics international*, **2004**, 11 (7):36-42.
69. Terry A. L, Feldman L.C., and Mayer, J.W. Fundamentals of nanoscale film analysis: *Springer Science & Business Media*, **2007**

70. Vemuri, R.S, Bharathi, K. K., Gullapalli, S.K., Ramana, C.V. Effect of structure and size on the electrical properties of nanocrystalline WO3 films. *ACS applied materials & interfaces*, vol. 2 (9),**2010**, pp. 2623-2628

71. Mudavakkat, V. H., Atuchin, V. V., Kruchinin, V. N., Kayani, A., Ramana, C. V. Structure, morphology and optical properties of nanocrystalline yttrium oxide (Y2O3) thin films. *Optical Materials*, vol. 34 (5), **2012**, pp. 893-900. doi: 10.1016/j.optmat.2011.11.027.

72. Oliver, W. C., Pharr, G. W. An Improved Technique for Determining Hardness and Elastic Modulus using Load and Displacement Sensing Indentation Experiments. *J. Mater. Res.* **1992**, 7, 1564−1583.

73. Leedy, K. D., Chabak, K. D., Vasilyev, V., Look, D. C., Boeckl, J. J., Brown, J. L., Tetlak, S. E., Green, A. J., et al. Highly Conductive Homoepitaxial Si-doped Ga_2O_3 Films on (010) β-Ga_2O_3 by Pulsed Laser Deposition. *Appl. Phys. Lett.* **2017**, 111, 012103.

74. Kalygina, V. M., Zarubin, A. N., Nayden, Ye. P., Novikov, V. A., Petrova, Yu. S., Tolbanov, O. P., Tyazhev, A. V., Yaskevich, T. M. The Effect of Annealing on the Properties of Ga_2O_3 Anodic Films. *Semiconductors, vol.* 46, **2012**, pp.267−273.

75. Williamson, G. K., Hall, W. H. Discussion of the Theories of Line Broadening. *Acta Metall*. Vo. 1, **1953**, pp. 22−31.

76. Kalidindi, N. R., Manciu, F. S., Ramana, C. V. Crystal Structure, Phase, and Electrical Conductivity of Nanocrystalline W0.95Ti0.05O3 Thin Films. *ACS Appl. Mater. Interfaces* vol. 3, **2011**, 863− 868.

77. Shvets, V. A., Aliev, V. Sh, Gritsenko, D. V., Shaimeev, S. S., Fedosenko, E. V., Rykhlitski, S. V., Atuchin, V. V., Gritenko, V. A., Taplin, V. M., Wong, H. Electronic

Structure and Charge Transport Properties of Amorphous Ta2O5 films. *J. Non-Cryst. Solids*, vol. 354, **2008**, pp. 3025−3033.

78. Atuchin, V. V., Lebedev, M. S., Korolkov, I. V., Kruchinin, V. N., Maksimovskii, E. A., Trubin, S. V. Composition-Sensitve Growth Kinetics and Dispersive Optical Properties of Thin HfxTi1-xO2 ($0 \leq x \leq 1$) Films Prepared by the ALD Method. *J. Mater. Sci.: Mater. Electron*, vol. 30, **2019**, pp. 812−823.
79. Kittel, C. Introduction to Solid State Physics, *Wiley*: New York, **1968**.
80. Battu, A. K., Zade, V. B., Deemer, E., Ramana, C. V. Microstructure-Mechanical Property Correlation in Size Controlled Nanocrystalline Molybdenum Films. *Adv. Eng. Mater.* **2018**, 1800496.
81. Holmberg, K., Ronkainen, H., Matthews, A. Tribology of Thin Coatings. *Ceram. Int, vol* 26, **2000**, pp. 787−795.
82. Nix, W. D. Mechanical Properties of Thin Films. *Metall. Trans. A*, 20, **1989**, 2217
83. Beake, B. D., Vishnyakov, V. M., Valizadeh, R., Colligon, J. S. Influence of Mechanical Properties on the Nanoscratch Behaviour of Hard Nanocomposite TiN/Si3N4 Coatings on Si. J. *Phys. D: Appl. Phys*, vol39, **2006**, pp. 1392−1397.
84. Leyland, A., Matthews, A. On the Significance of the H/E Ratio in Wear Control: a Nanocomposite Coating Approach to Optimised Tribological Behaviour. *Wear*, vol 246, **2000**, pp. 1−11.
85. Jenkins, F. A., White, H. E. Fundamentals of Optics, 4th ed., McGraw-Hill, Inc., **1981**.
86. Ramana, C. V., Mudavakkat, V. H., Kamala Bharathi, K., Atuchin, V. V., Pokrovsky, L. D., Kruchinin, V. N. Enhanced Optical Constants of Nanocrystalline Yttrium Oxide Films. *Appl. Phys. Lett*., vol. 98, **2011**, 031905.

87. Atuchin, V. V., Kalinkin, A. V., Kochubey, V. A., Kruchinin, V. N., Vemuri, R. S., Ramana, C. V. Spectroscopic Ellipsomtery and XRay Photoelectron Spectroscopy of La2O3 Thin Films Deposited by Reactive Magnetron Sputtering. *J. Vac. Sci. Technol*. *A*, vol. 29, **2011**, 021004.

88. Makeswaran, N., Battu, A. K., Swadipta, R., Manciu, F. S., Ramana, C. V. Spectroscopic Characterization of Electronic Structure, Chemical Bonding, and Band Gap in Thermally Annealed Polycrystalline Ga_2O_3 Thin Films. *ECS J. Solid State Sci. Technol*, ol 8, **2019**, Q3249−Q3253.

89. Tripathi, A., Harris, K. D., Elias, A. L. Peroxidase-Like Behavior of Ni Thin Films Deposited by Glancing Angle Deposition for Enzyme-Free Uric Acid Sensing. *ACS Omega*, vol. 5, **2020**, 9123−9130.

90. Guo, Z., Verma, A., Wu, X., Sun, F., Hickman, A., Masui, T., Kuramata, A., Higashiwaki, M., Jena, D., Luo, T. Anisotropic thermal conductivity in single crystal β-gallium oxide. *Appl. Phys. Lett.*, vol. 106, **2015**, 111909

91. Krishnan, R., Lu, T. M., Koratkar, N. Functionally strain-graded nanoscoops for high power Li-ion battery anodes. *Nano Lett*., vol. 11, **2011**, pp. 377−84.

92. Gottapu, S., Padhi, S. K., Krishna, M. G., & Muralidharan, K. . Poly(vinylpyrrolidone) stabilized Aluminum Nanoparticles obtained by the reaction of sicl4 with LiAlH4. *New Journal of Chemistry*, vol. **39**(7), **2015,** pp5203-5207. doi:10.1039/c5nj00438a

93. Keiteb, A. S., Saion, E., Zakaria, A., & Soltani, N.. Structural and optical properties of zirconia nanoparticles by thermal treatment synthesis. *Journal of Nanomaterials*, **2016**, pp. 1-6. doi:10.1155/2016/1913609

94. Wang, J., Tsuzuki, T., Tang, B., Cizek, P., Sun, L., & Wang, X. Synthesis of Silica-coated Zno nanocomposite: The resonance structure of Polyvinyl pyrrolidone (PVP) as a COUPLING AGENT. *Colloid and Polymer Science*, vol. 288(18), **2010,** pp. 1705-1711. doi:10.1007/s00396-010-2313-8

95. Liu, H., Cai, C., Jia, M., Gao, J., Yin, H., & Chen, H. Experimental investigation on spray cooling with low-alcohol additives. *Applied Thermal Engineering*, vol. 146, **2019**, pp. 921-930. doi:10.1016/j.applthermaleng.2018.10.054

96. Ross, M., Kelly, J., Finkenauer, L., & Haslam, J. **(2019)**. Composite 4YSZ-Al2O3 NANOFIBERS prepared by ELECTROSPINNING and thermal processing. Retrieved March 27, 2021, from https://www.osti.gov/biblio/1571371-composite-al2o3-nanofibers-prepared-electrospinning-thermal-processing

97. Schreuder-Gibson, H. L., Gibson, P., & Tsai, P. Cooperative charging effects of fibers from electrospinning of electrically dissimilar polymers. *International Nonwovens Journal*, **2004** Os-13(4). doi:10.1177/1558925004os-1300406

98. Collins, G., Federici, J., Imura, Y., & Catalani, L. H. (). Charge generation, charge transport, and residual charge in the electrospinning of polymers: A review of issues and complications. *Journal of Applied Physics*, vol. 111(4), **2012** 044701. doi:10.1063/1.3682464

99. Zhou, T., Chen, P., Hu, S., Yan, Y., Pan, W., & Li, H. Enhanced yellow luminescence of amorphous Ga_2O_3 nanofibers with tunable crystallinity. *Ceramics International*, vol. 42(5), **2016,** pp. 6467-6474. doi:10.1016/j.ceramint.2015.12.105

100. Deitzel, J., Kleinmeyer, J., Harris, D., & Tan, N. B. The effect of processing variables on the morphology of electrospun nanofibers and textiles. *Polymer*, vol. 42(1), **2001,** pp. 261-272. doi:10.1016/s0032-3861(00)00250-0

101. Cejudo, A. M. High-pressure optical and vibrational properties of Ga 2 O 3 nanocrystals. Masters thesis, University of Barcelona. **2017**. Màster Oficial - Nanociència i Nanotecnologia 2017

102. Dohy, D., Lucazeau, G., & Revcolevschi, A. Raman spectra and valence force field of single-crystalline β Ga_2O_3. *Journal of Solid State Chemistry*, vol. 45(2), **1982,** pp. 180-192. doi:10.1016/0022-4596(82)90274-2

103. Ho, C., Tseng, C., & Tien, L. Thermoreflectance characterization of β-Ga_2O_3 thin-film nanostrips. Optics Express, vol. 18(16), **2010,** 16360. doi:10.1364/oe.18.016360

104. Zhang, Y., Yang, J., Li, Q., & Cao, X. (). Preparation of Ga_2O_3 nanoribbons and tubes by electrospinning. *Journal of Crystal Growth*, vol. 308(1), **2007,** pp. 180-184. doi:10.1016/j.jcrysgro.2007.07.036

105. Kakoria, A., Devi, B., Anand, A., Halder, A., Koner, R. R., & Sinha-Ray, S. (). Gallium Oxide Nanofibers for Hydrogen Evolution and Oxygen Reduction. *ACS Applied Nano Materials*, vol 2(1), **2018,** pp. 64-74. doi:10.1021/acsanm.8b01651

106. Taş, A. C., Majewski, P. J., & Aldinger, F. (). Synthesis of Gallium Oxide Hydroxide Crystals in Aqueous Solutions with or without Urea and Their Calcination Behavior. *Journal of the American Ceramic Society*, vol. 85(6), **2002,** pp. 1421-1429. doi:10.1111/j.1151-2916.2002.tb00291.x

107. Berbenni, V., Milanese, C., Bruni, G., & Marini, A. Thermal decomposition of gallium nitrate hydrate Ga(NO3)3×xH2O. *Journal of Thermal Analysis and Calorimetry*, **2005** 82(2), 401-407. doi:10.1007/s10973-005-0909-x

108. Poerschke D. L., Levi C. G. Yttrium bearing silicon carbide matrices for robust ceramic composites, *Journal of the American Ceramic Society*, vol. 96, no. 4, **2013** pp. 1300–1308

109. Eils N. K., Mechnich P., Braue W. Effect of CMAS Deposits on MOCVD Coatings in the System Y2O3–ZrO2: Phase Relationships, *J. Am. Ceram. Soc*., vol 96, no. 10 **2013** pp. 3333-3340

110. Krause A. R., Garces H. F., Herrmann C. E., Padture N. P. Resistance of 2ZrO2 Y2O3 top coat in thermal/environmental barrier coatings to calcia-magnesia-aluminosilicate attack at 1500°C, *Journal of the American Ceramic Society*, vol. 100, no 7, **2017**, pp. 3175-3187

111. Krause A. R., Li X., Padture N. P., Interaction between ceramic powder and molten calciamagnesia-alumino-silicate (CMAS) glass, and its implication on CMAS-resistant thermal barrier coatings, *Scripta Materialia*, vol. 112, **2016,** pp. 118-122

112. Braue W., Mechnich P. Recession of an EB-PVD YSZ Coated Turbine Blade by CaSO4 and Fe, Ti-Rich CMAS-Type Deposits, *J. Am. Ceram. Soc*., vol 94, no. 12, **2011,** pp. 4483–4489

Vita

Nanthakishore Makeswaran was born September 09, 1992 in India. Mr. Makeswaran received a Bachelor of Science in Aerospace engineering from the Florida Institute of Technology in May 2013. After working for a time, he enrolled in the Integrated Ph.D. program at the University of Texas at El Paso in 2016 in the Department of Mechanical Engineering. He completed an 8-month Ph.D. research internship at Lawrence Livermore National Laboratory, two summer Ph.D. research internships at the Air Force Research Laboratory during the summers of 2018 and 2019, and completed a 4 month guest researcher position at the German Aerospace Center beginning in 2019 and completing 2020 at part of his continued Ph.D. studies. He has several first and co-author publications in various scientific journals

This Dissertation was typed by Nanthakishore Makeswaran